An Android-Enabled Modular Self-Interference Cancellation System for

Standalone Simultaneous Transmit and Receive Multichannel Magnetic Resonance

Imaging at 1.5T

by

Zachary Allen Colwell

A Dissertation Presented in Partial Fulfillment
of the Requirements for the Degree
Doctor of Philosophy

Approved October 2023 by the
Graduate Supervisory Committee:

Sung-Min Sohn, Co-Chair
George Trichopoulos, Co-Chair
James Aberle
Rosalind Sadleir

ARIZONA STATE UNIVERSITY

December 2023

ABSTRACT

In 1946 Felix Bloch first demonstrated the phenomenon of nuclear magnetic

resonance using continuous-wave signal generation and acquisition. Shortly after in 1966,

Richard R. Ernst demonstrated the breakthrough that nuclear magnetic resonance needed

to develop into magnetic resonance imaging: the application of Fourier transforms for

sensitive pulsed imaging. Upon this discovery, the world of research began to develop

high power radio amplifiers and fast radio switches for pulsed experimentation.

Consequently, continuous-wave imaging placed on the backburner.

Although high power pulses are dominant in clinical imaging, there are unique

advantages to low power, continuous-wave pulse sequences that transmit and receive

signals simultaneously. Primarily, tissues or materials with short T_2 time constants can be

imaged and the peak radio power required is drastically reduced.

The fundamental problem with this lies in its nature; the transmitter leaks a strong

leakage signal into the receiver, thus saturating the receiver and the intended nuclear

magnetic resonance signal is lost noise.

Demonstrated in this dissertation is a multichannel standalone simultaneous

transmit and receive (STAR) system with remote user-control that enables continuous-

wave full-duplex imaging. STAR calibrates cancellation signals through vector

modulators that match the leakage signal of each receiver in amplitude but opposite in

phase, therefore destructively interfering the leakage signals. STAR does not require

specific imaging coils or console inputs for calibration. It was designed to be general-

purpose, therefore integrating into any imaging system. To begin, the user uses an

Android tablet to tune STAR to match the Larmor frequency in the bore. Then, the user

tells STAR to begin calibration. After self-calibrating, the user may fine-tune the

calibration state of the system before enabling a low-power mode for system electronics

and imaging may commence. STAR was demonstrated to isolate two receiver coils

upwards of 70 dB from the transmit coil and is readily upgradable to enable the use of

four receive coils.

Some primary concerns of STAR are the removal of transceivers for multichannel

operation, digital circuit noise, external noise, calibration speed, upgradability, and the

isolation introduced; all of which are addressed in the proceeding thesis.

DEDICATION

To Ivy bug; the grooviest gal and my tiniest friend. I love you.

ACKNOWLEDGMENTS

I would like to thank my advisor and committee members for their support and valuable insights throughout my undergraduate, masters, and doctorate journeys at ASU. Not only have you all challenged my work and inspired me to be a better researcher, but you also often provided the fundamental basis I needed to even call myself an engineer and infinitely fed a curious mind. This also includes ASU; I've spent more than a third of my life wandering campus, pondering the nature of our universe and how we, as engineers, have found strange ways to harness it. I'm beyond delighted to have started my journey with you all.

I would also like to thank our friends and collaborators at the Center of Magnetic Resonance Research at the University of Minnesota for allowing me to pester them in their lab yonder to test and develop my STAR systems. Without you, STAR would not exist, and I would not have found myself fortunate enough to work in medical devices for my career.

Of course, I would also like to thank my lab partners, mentors, and mentees in BiCS lab. We found ourselves lucky enough as kids to build a new research lab from the ground up. I reflect equally fondly on Tuesday afternoon coffees and Saturday night circuit debugging because of you. I could only hope we remain lifelong friends bonded equally by our quirks and silliness.

Last and certainly not least, I would like to thank my friends and family. Whether I tackled a PhD or started a garage band, you all would have been equally loving and supportive, which is why I took-up the piano at the start of my PhD, just in case STAR did not work out. Without you I would not have been able to sustain my spirit these past

few years. Some of us muscled through grad school together and some of you just wanted me to fix your WiFi; either way, you've been the most critical component of my success and I love you all. I love and miss you every day, dad. I wish you could have been here for one last graduation.

TABLE OF CONTENTS

LIST OF TABLES

LIST OF FIGURES

CHAPTER 1

INTRODUCTION

Magnetic resonance imaging (MRI) is a powerful imaging technique that has rapidly developed from physics to machine in the past century. With its ability to produce high contrast images of soft tissues, MRI has found its niche in the world of medical imaging. MRI may be an extension of the nuclear magnetic resonance (NMR) phenomenon, but it is not alone. NMR spectroscopy and functional MRI cohabitate with standard MRI as well in the world of applied NMR physics.

The essence of MRI lies in the atomic physics upon which it was developed. Arguably, it begins with Joseph Larmor and his understanding of atomic *precession* in the year 1897 [1]. Larmor was the first to derive the concept of nuclear magnetic precession, where the magnetic moment of any particle with a non-zero quantum spin will precess about an externally applied magnetic field; now, this is known as Larmor precession. Fast forward half of a century past the first introductions of magnetic moments, and this non-trivial revelation in physics allowed Felix Bloch to publish his famous nuclear induction paper in 1946 [2,3]. Simultaneously across the country, Edward Purcell also demonstrated the NMR phenomenon, hence they shared the Nobel prize in 1952 [4].

Although the initial NMR experimentation by Bloch was continuous wave (CW), pulsed MRI arose in the 1950s with the Hahn echo, now referred to as the *spin echo* [5,6]. In 1966, Ernst demonstrated that pulsed MRI had an intrinsically increased sensitivity compared to CW MRI, thus the hardware developments followed [7].

1

Continuous wave MRI, often synonymous with adiabatic NMR, does however have unique advantages. The primary advantages for imaging are the ability to image tissues and materials with short T_2 time constants and the drastically reduced radio frequency (RF) power requirements [8]. But, any advantages of adiabatic pulse sequence, in general, also now apply to simultaneous transmit and receive MRI. Some of these include potentially reduced motion artifacts, reduced specific absorption rate (SAR), reduced hardware costs, decreased B_1 field inhomogeneity sensitivity, and reduced acoustic noise due to slow-switching gradients [9-13].

The fundamental issue with CW MRI and NMR lies in its full-duplex nature. To transmit and receive signals simultaneously while your receiver is close in proximity to your transmitter, is to couple a strong leakage signal from the transmitter to the receiver. Also referred to as self-interference, this leakage signal is considerably stronger than the NMR signal from our tissue of interest, thus, image reconstruction is nearly impossible without efforts to isolate the receiver from the leakage signal. STAR hardware provides this isolation for MRI, although this problem is not unique to MRI; technologies such as frequency modulated continuous wave (FMCW) radar, radio frequency identification (RFID), and even modern communication systems with the rise of technology like 5G also face the leakage signal issue [14-20].

This work contributes to the solution of the self-interference problem by forcing the leakage signal to undergo destructive interference in the RF domain. Previous contributions are also rooted in RF cancellation, amongst other techniques, however, they lack a general-purpose application, or their frameworks are not readily built upon.

The continuous sweep imaging with Fourier transform (SWIFT) publication of 2012 detailed the importance of removing leakage signal for this new method of continuous wave imaging [8]. Shortly after, a few publications and conference abstracts were published for 3T and 4T STAR applications, hardware developments, and limitations [21-26]. Most recently (as of 2023), my standalone STAR paper demonstrated the feasibility of a standalone self-calibrating system that readily integrated with any RF coil and MRI console, thus establishing a STAR framework that was readily adapted to and integrated into any MRI console equipped with the continuous SWIFT pulse sequence [27]. This work and publication are the foundation for multi-channel STAR as well.

Some of the next steps for low power continuous wave STAR outlined here are to demonstrate the application of a modular multichannel STAR system for 1.5T clinical MRI, however, most of the circuits can reasonably accommodate higher field strengths, thus higher frequency RF signals. The framework and system provided allow STAR to be used with any MRI system while also joining forces with other retrofitted MRI technologies in the future such as automatic tuning and matching or power monitoring [28].

Chapter 1 outlined the basic history and motivations for MRI, continuous wave MRI, and the consequential STAR hardware.

Chapter 2 begins with the fundamental physics regarding quantum spin, proton precession, and the Bloch equations. These concepts should give the background intuition required to understand how NMR signals can be induced in the presence of a strong magnetic field. Also included is some electrical engineering background regarding

scattering parameters, transmission lines, and the printed circuit board (PCB) design philosophy used to develop standalone STAR.

Chapter 3 discusses the radio frequency (RF) hardware used in MRI and how it relates to the pulse sequences used for signal, thus image, generation, and acquisition. This includes brief discussions of power amplifiers, low noise amplifiers, and gradient coils; along with an extended review of RF coils. This naturally leads to the discussion of standard MRI pulse sequences compared to the continuous SWIFT pulse sequence and the consequentially difference hardware requirements.

Chapter 4 is entirely dedicated to standalone STAR. Beginning with the key concepts, it provides a comprehensive overview of STAR, then jumps into the current standalone STAR publication, and ends with the new multichannel STAR system. Included are data and discussions for every circuit and system within STAR.

Chapter 5 concludes the dissertation with a summary and an outlook on the future of STAR.

CHAPTER 2

SPIN PHYSICS AND ENGINEERING BACKGROUND

There are a few key physics concepts that carry the bulk of weight in understanding how MRI is feasible. The first is spin; without understanding spin, we cannot apply the concept of precession. And without precession, Bloch would not have been able to derive his famous equations for understanding the mechanism behind NMR signal generation.

These three equations of modern physics carry physical consequences that can be measured with well-engineered equipment. In terms of electrical engineering, a few of the most important concepts for at least understanding the proceeding STAR information are scattering parameters, transmission lines, and general MRI circuits.

2.1 Spin

One of the four fundamental quantum numbers for matter is intrinsic angular momentum, which is more commonly known as spin. Spin (I), which is quantized in increments of ½, is at the heart of NMR, thus MRI. Particularly interesting for NMR is the fact that spin relates to an associated magnetic dipole moment of a particle or atom. Unfortunately, determining nuclear spin is not as simple as summing the proton and neutron spins within the nucleus. Since protons and neutrons are not fundamental particles, their spin partially arises from sub-sub-atomic particles, such as quarks and gluons. It can be inferred from this information, that the spin of a nucleus depends not only on the element, but also the isotope. The potential spins a nucleus may have is predictable through three rules, however, the exact spin can only (as of now) be measured

experimentally. The three rules for determining the potential spin of a nucleus are as follows:

1. The nucleus has zero spin if the number of protons and neutrons are both even.

2. The nucleus has half-integer spin ($^1/_2$, $^3/_2$, etc.) if the sum of protons and neutrons is odd.

3. The nucleus has integer spin (1, 2, etc.) if the number of protons and neutrons are both odd.

Because of these characteristics of spin, many isotopes cannot be interacted with via NMR, such as Carbon-12 (^{12}C). Instead, if carbon spectroscopy would like to be performed, then metabolites must be doped with ^{13}C, for example. Fortunately for the us water-based creatures, the most common isotope of Hydrogen, ^1H, has a spin of ½.

2.2 Precession

An externally applied static magnetic field interacts with the magnetic dipole moment of a nucleus to form distinct energy states. Particularly useful for MRI are atoms with spin I = ½, like ^1H. A spin of ½ allows only two unique energy states to exist simultaneously in the presence of a static magnetic field, corresponding to what will be herein referred to as "up-spin" and "down-spin," denoted as $N_\uparrow$ and $N_\downarrow$, respectively.

The stronger the magnetic field, the higher the energy difference between these two states, shown in equation 1, where ΔE Is the difference in energy in Joules, γ is gyromagnetic ratio in megahertz/Tesla, $\hbar$ is the reduced planks constant in Joule-seconds and B_o is the strength of the magnetic field in Tesla. The difference in energy between the spin states is referred to as Zeeman splitting, which can be seen in figure 1 [29].

$$\Delta E = \gamma \hbar B_o$$

Equation. 1 Zeeman splitting energy difference
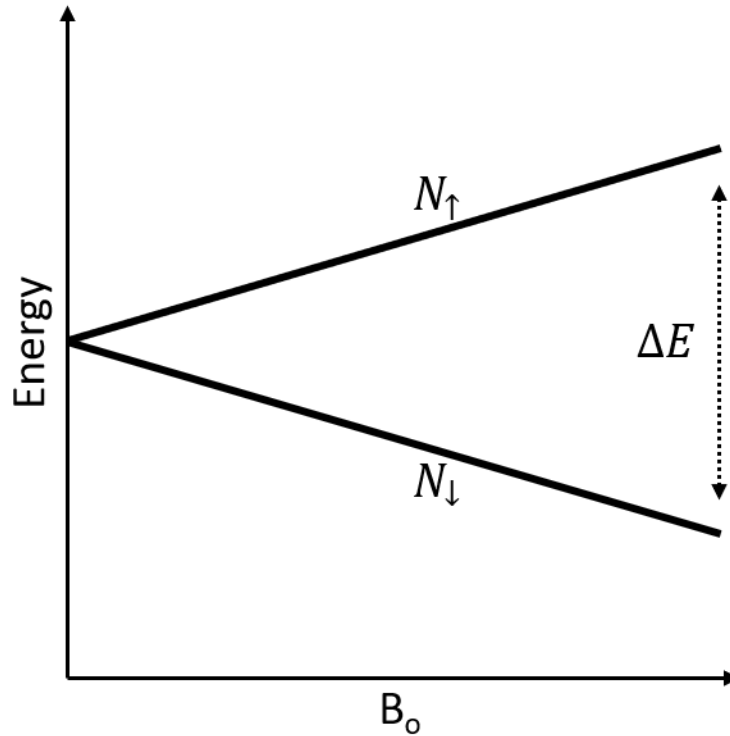
Figure. 1 Zeeman splitting

According to classical Boltzmann statistics, the difference in quantity between $N_\uparrow$ and $N_\downarrow$ in a particular volume of temperature T in Kelvin and magnetic field B_o in Tesla is:

$$\frac{N_\uparrow}{N_\downarrow} = e^{\Delta E / kT}$$

Equation. 2 Boltzmann distribution of spins at equilibrium

Where k is the Boltzmann constant in Joules/Kelvin. If we assume $\Delta E \ll kT$ then the Boltzmann distribution can be approximated as a linear difference between $N_\uparrow$ and $N_\downarrow$:

$$N_\uparrow - N_\downarrow \approx (N_\uparrow + N_\downarrow)\frac{\Delta E}{2kT}$$

Equation. 3 Reduced Boltzmann distribution

This net spin quantity shows us how many spins are producing a signal and results in a magnetization vector, **M**, which at equilibrium precesses about B_o at frequency f_o MHz in accordance to the Larmor equation:

$$f_o = \gamma B_0$$

Equation. 4 Larmor equation

We can now see, that the stronger the B_0 field, the larger the difference between $N_\uparrow$ and $N_\downarrow$, thus the more net signal we can acquire for NMR experimentation and imaging. This is the primary drive for higher field strengths in NMR and MRI.

2.3 Bloch Equations

To capture the essence of MRI, one certainly must begin with appreciating the Bloch equations: a concise triplet, who allow us to understand the change of the bulk nuclear magnetization vector, $\mathbf{M}(t) = M_x(t), M_y(t), M_z(t)$ when nuclei are in the presence of an externally applied magnetic field, $\mathbf{B}(t) = B_x(t), B_y(t), B_z(t)$. It is to be noted that **B** represents magnetic flux density, but is commonly referred to as the magnetic field, instead of **H**. Assuming the applied main magnetic field is in the z-direction, then the differential form of the Bloch equations are as follows:

$$\frac{dM_x(t)}{dt} = \gamma(\mathbf{M}(t) \times \mathbf{B}(t))_x - \frac{M_x(t)}{T_2}$$

$$\frac{dM_y(t)}{dt} = \gamma(\mathbf{M}(t) \times \mathbf{B}(t))_y - \frac{M_y(t)}{T_2}$$

$$\frac{dM_z(t)}{dt} = \gamma(\mathbf{M}(t) \times \mathbf{B}(t))_z - \frac{M_z(t) - M_0}{T_1}$$

Equation. 5 Bloch equations in differential form

Due to the phenomenon of precession, our coordinate system from our (the lab) point of view is rotating. However, if we select our observations to co-rotate with the precessing isochromats, then we can introduce a more convenient rotating frame coordinate system [30]. In this rotating coordinate system, the Bloch equations can be solved as follows:

$$M_x(t) = M_0 \sin(\theta) \sin(\omega_0 t) \, e^{-\frac{t}{T_2}}$$

$$M_y(t) = M_0 \sin(\theta) \cos(\omega_0 t) \, e^{-\frac{t}{T_2}}$$

$$M_z(t) = M_0 \left[1 - (1 - \cos(\theta)) e^{-\frac{t}{T_1}} \right]$$

Equation. 6 Bloch equations solved

M_0 represents the magnitude of the bulk magnetization vector at equilibrium, T_1 represents the longitudinal (spin-lattice) relaxation time, and T_2 represents the transverse (spin-spin) relaxation time. T_1 was defined by Bloch to be the time it took spins (isochromats) to realign 63% of M_0 in the z-direction and T_2 was defined to be the time it took the spins to dephase or decay down to only 37% of M_0 in the xy-plane.
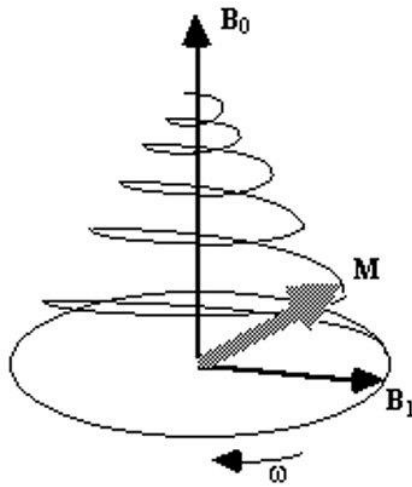
Figure. 2 Spin relaxation

Solutions to the Bloch equations in terms of M_x signal intensity and M_z signal intensity for 64 MHz signals in water and in tendons are shown in figure 3 in the form of exponentially decaying sinusoids. The T_1 and T_2 used for water were 4000 ms and 2000 ms, respectively, as can be seen in the left figure. The T_1 and T_2 used for tendons to

highlight how short T_2 can be, thus alluding to the application of STAR, were 400 ms and 5 ms, respectively, as can be seen in the right and center figures [31].
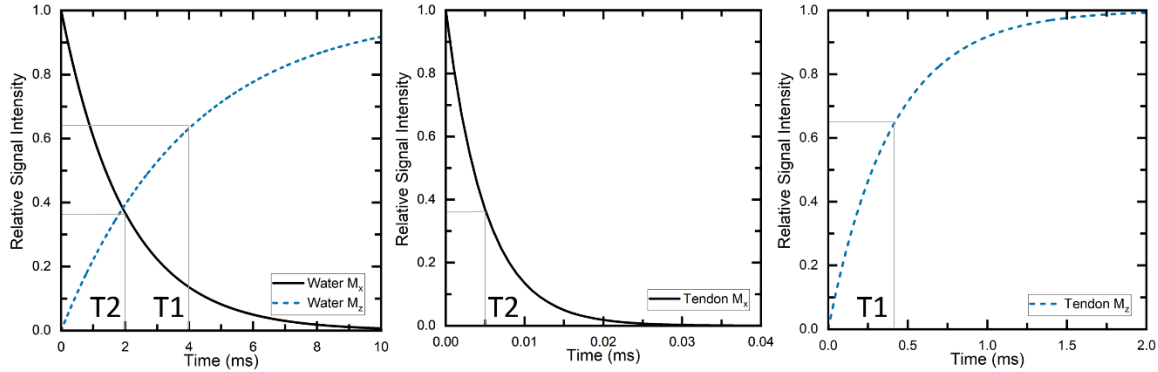
Figure. 3 Bloch equations solutions in water (left) and in tendons (center, right)

2.4 Scattering Parameters

Scattering Parameters are one of the most commonly used measurements to characterize an N-port RF circuit component, device, system, etc. Scattering parameters are defined by looking at incident voltages at each port of the device under test (DUT), as outlined below [32]. In fact, vector network analyzers, arguably the most important tool in any RF engineering lab, happily provide data in terms of scattering parameters.

Scattering parameters of an N-port system are concisely summarized in an N x N scattering matrix, as follows:

$$
\begin{bmatrix} V_1^- \\ V_2^- \\ \vdots \\ V_N^- \end{bmatrix} = \begin{bmatrix} S_{11} & S_{12} & \ldots & S_{1N} \\ S_{21} & S_{22} & \ldots & S_{2N} \\ \vdots & \vdots & \ddots & \vdots \\ S_{N1} & S_{N2} & \ldots & S_{NN} \end{bmatrix} \begin{bmatrix} V_1^+ \\ V_2^+ \\ \vdots \\ V_N^+ \end{bmatrix}
$$

Equation. 7 Scattering matrix

11

Where V_i^- is the voltage of the wave exiting port i and V_j^+ is the voltage of the wave entering port j. The scattering parameter S_{ij} is thus defined using these voltages when all ports, other than port j are terminated with load matched to the system impedance.

$$S_{ij} = \frac{V_i^-}{V_j^+}$$

Equation. 8 Scattering element

Provided all ports of a DUT, other than port j are terminated in a matched load, S_{jj} equals the reflection coefficient of that port, Γ. We can then define the return loss of the port to be:

$$RL = -20log|\Gamma| = -20log|S_{jj}|.$$

Equation. 9 Return loss

Furthermore, S_{ij} corresponds to the insertion loss a wave undergoes when entering port j and exiting port i such that:

$$IL = -20log|S_{ij}|.$$

Equation. 10 Insertion loss

There is another parameter, isolation, that can also be defined by flipping the subscripts of insertion loss, such that:

$$ISO = -20log|S_{ji}|$$

Equation. 11 Isolation

12

2.5 Transmission Lines

Impedance is one of the most important electrical engineering concepts, especially for RF engineering due to the extended concept of impedance matching and the nature of transmitting signals through transmission lines. Any two conductors in proximity to one-another have a mutual inductance, *L*, and capacitance, *C*. If the conductors and the dielectric medium between them are lossless, which is a reasonable approximation for the low RF frequencies in MRI, then the intrinsic impedance, Z_0, of this effective transmission line is predicted by the following:

$$Z_0 = \sqrt{\frac{L}{C}}\,\Omega$$

Equation. 12 Transmission line intrinsic impedance

This tells us that if we can calculate the mutual inductance and capacitance of any two conductors, then we can calculate the impedance of a wave travelling along them; therefore, we can electrically characterize the conductor system. If a load with impedance Z_L is attached to the end of the line at a distance ℓ meters, then one could measure the input impedance, Z_{in}, seen by a source of impedance Z_s on the other side of the line for any phase constant $\left(\beta = {2\pi}/{\lambda}\right)$ radians/meter, where λ is wavelength in meters, as:

$$Z_{in} = Z_0 \frac{Z_L + jZ_0 \tan \beta\ell}{Z_0 + j Z_L \tan \beta\ell}\,\Omega$$

Equation. 13 Transmission line input impedance

Any two devices or components can be characterized together regarding their impedances Z_1 and Z_2 using the reflection coefficient, Γ. If their impedances are different, then propagating waves reflect in accordance with the reflection coefficient, such that:

$$\Gamma = \frac{Z_2 - Z_1}{Z_2 + Z_1}$$

Equation. 14 Reflection coefficient

2.5.1 PCB Transmission Lines

There are many types of transmission lines used for transferring electromagnetic energy between two points in space. When using printed circuit boards, a few are extremely common. Two of these are coplanar waveguides (CPWG) and striplines. Microstrips are probably the most common, however, they are similar to coplanar waveguides and for this work were not favored, thus omitted from discussion. If another conductor were introduced into a waveguide, thus enabling transverse electromagnetic (TEM) wave propagation and quasi-TEM propagation, you start to form a transmission line. As PCB technology developed, transmission lines were no longer limited to the likes of coaxial cables and twin conductor lines, rather, they could be further studied to place onto and into circuit boards. Poetically, coplanar waveguides are a common type of PCB transmission line, where the structure begins to resemble their ancestors: the humble waveguide. Although, it is to be noted, transmission lines were theorized just before waveguides; however, waveguides came around before our friendly transmission line the coplanar waveguide.

Designing transmission lines is easy for two-layer boards with simple circuit designs. As circuit complexity increases, however, transmission lines become a more

14

integral part of the entire system rather than a necessary afterthought. The first step in designing transmission lines is to understand the limitations of the chosen manufacturing process. Since I have elected to use JLCPCB's four layer and eight-layer stackups, my boards must adhere to their respective design rules and impedance control [33].

2.5.2 Coplanar Waveguides

Coplanar waveguides are transmission lines with less radiation losses and enhanced noise immunity compared to the common microstrip. They also contain an extra degree of freedom in their design parameters, which can be convenient when you are locked-in to a particular manufacturing process and cannot control the substrate thickness.

Coplanar waveguides are formed by simply placing a thin signal conductor on top of a substrate, then placing a ground plane (a copper pour) coplanar with the thin conductor. A grounded coplanar waveguide (GCPWG) is the same, except there is also a ground plane on the bottom of the substrate and the ground planes are connected with vias. This is the transmission line structure that most resembles a rectangular waveguide, thus the name coplanar waveguide. The impedance of a grounded coplanar waveguide with substrate height (thickness) h, trace width W, and combined track width and ground plane spacing S, can be calculated using the following formulas using elliptical integrals of the first kind (K) [34]:

$$Z_0 = \frac{60\pi}{\sqrt{\varepsilon_{eff}}} \frac{1}{\frac{K(k)}{K(k')} + \frac{K(k_1)}{K(k_1')}} \ \Omega$$

$$\varepsilon_{eff} = \frac{1 + \varepsilon_r \frac{K(k')}{K(k)} \frac{K(k_1)}{K(k_1')}}{1 + \frac{K(k')}{K(k)} \frac{K(k_1)}{K(k_1')}} \ F/m$$

$$k = \frac{W}{S}$$

$$k_1 = \frac{\tanh\left(\frac{\pi W}{4h}\right)}{\tanh\left(\frac{\pi S}{4h}\right)}$$

$$k' = \sqrt{1 - k^2}$$

$$k_1' = \sqrt{1 - k_1{}^2}$$

Equation. 15 Coplanar waveguide design equations

2.5.3 Striplines

Striplines are a type of transmission line where a thin signal conductor is sandwiched in between two ground planes while being held in place by one or two dielectric substrates and the electric fields extend from the center conductor to both the top and bottom ground conductors. If the ground planes are equally spaced from the center conductor and the dielectrics are the same, then a true TEM wave can propagate, thus enabling the stripline to be relatively non-dispersive and less prone to EMI concerns. If ground spacings are not equal, then the line is an asymmetric stripline, and this is likely to be common with cheaper manufacturing processes; actually, even the dielectrics are likely to be different since one is prepreg and one is core when it comes to the popular

16

FR4 substrate. The impedance calculations for striplines have been omitted since they were not used in this design and the discussion of striplines was simply to enrich the discussion on "embedded" coplanar waveguides.

2.5.4 Embedded Coplanar Waveguides

When a grounded coplanar waveguide is taken and a ground plane is added on top, it begins to resemble some sort of shielded coplanar waveguide. I have called this an "embedded coplanar waveguide" since the line now exists on the spectrum between a stripline and a grounded coplanar waveguide. An easy way to understand where on the spectrum it lies is to use a tool like Ansys HFSS to view the fields associated with it. Visualizing the electric and magnetic fields of a transmission line can help develop an intuition for the design process and an intuition for potential unwanted electromagnetic interference (EMI) concerns. The electric fields for the embedded coplanar waveguides used in STAR with via stitching at 64 MHz can be seen in figure 4. The substrates were omitted for clarity.
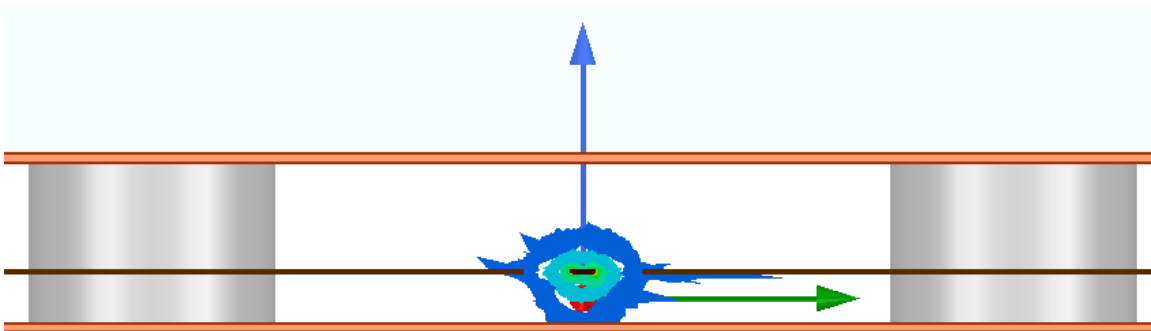
Figure. 4 Electric field magnitude of embedded coplanar waveguide at 64 MHz

The fields extend from the center conductor to both side ground planes and towards the bottom ground plane, yet they do not extend to the top ground plane. Herein lies the justification of the terminology "embedded" coplanar waveguide instead of just an asymmetric stripline.

2.5.5 Transmission Lines in STAR

Three types of transmission lines are used in STAR: coaxial cables, standard grounded coplanar waveguides, and the aforementioned embedded grounded coplanar waveguides. Coaxial cables are required to interface STAR with the RF coils and the MRI console. Grounded coplanar waveguides were used instead of microstrips on top and bottom of PCBs since they have less radiation loss, are a bit more noise resistant, and allow larger ground planes to exist on the board, thus embedded coplanar waveguides can also be introduced into the inner layers of four-layer and eight-layer boards. Although, embedded coplanar waveguides were introduced to further isolate the RF signals from noise, they also turned out to be a bit less sensitive to manufacturing tolerances, which was serendipitous.

To optimize the design parameters like transmission line width and ground gap width, HFSS was used with various parametric sweeps over the frequency range of DC to 500 MHz, hence the design was simulated for low extremely field MRI up to about 10.5T MRI. Although the designs were only used in a 1.5T system, knowing that the design philosophy and even most of the exact same circuits and PCB layouts could be used with many different main field strengths is great for rapid development and integrating similar circuits in other projects. The trace width was swept from 0.09 mm to 1.5 mm, the

adjacent ground spacing was swept from 0.1 mm to 3 mm, and the distance from the vias

to the trace edges was swept from 0 mm to 2 mm. Determining whether the result was a

standard or an embedded coplanar waveguide was done by simply viewing the electric

field inside the substrates, as previously shown. For eight-layer boards, the embedded

coplanar waveguides had trace widths of 0.09 mm and ground gaps of 0.2 mm, whereas

for four-layer boards, they had trace widths of 0.2 mm and a ground gap of 0.7 mm.

When standard grounded coplanar waveguides were required on eight-layer and four-

layer boards they had trace widths of 0.205 mm and ground gaps of 0.1 mm.

Before fully implementing the embedded coplanar waveguide into my boards, a

test board was created using the aforementioned eight-layer process. The test board

consisted of three different transmission line styles to test their performance. The first

lines were grounded coplanar waveguides, the second lines were embedded coplanar

waveguide, and the third set of lines were embedded coplanar waveguide and grounded

coplanar waveguides connected with epoxy-filled and copper-capped via. The board

layout can be seen in figure 5 alongside the physically soldered PCBA. The return loss

and insertion loss for all three transmission line systems is shown in figure 6.

Unexpectedly, the best performance came from the embedded coplanar waveguide,

followed by the via lines, and finally the grounded coplanar waveguides. Unfortunately,

standard grounded coplanar waveguides are a bit sensitive to process variations, which

likely resulted in the embedded coplanar waveguide performing best with their wider

ground spacing. Since the control parameters available for transmission line design

depends on your process, embedded coplanar waveguide ended up being optimal for

eight-layer boards in this design.

19
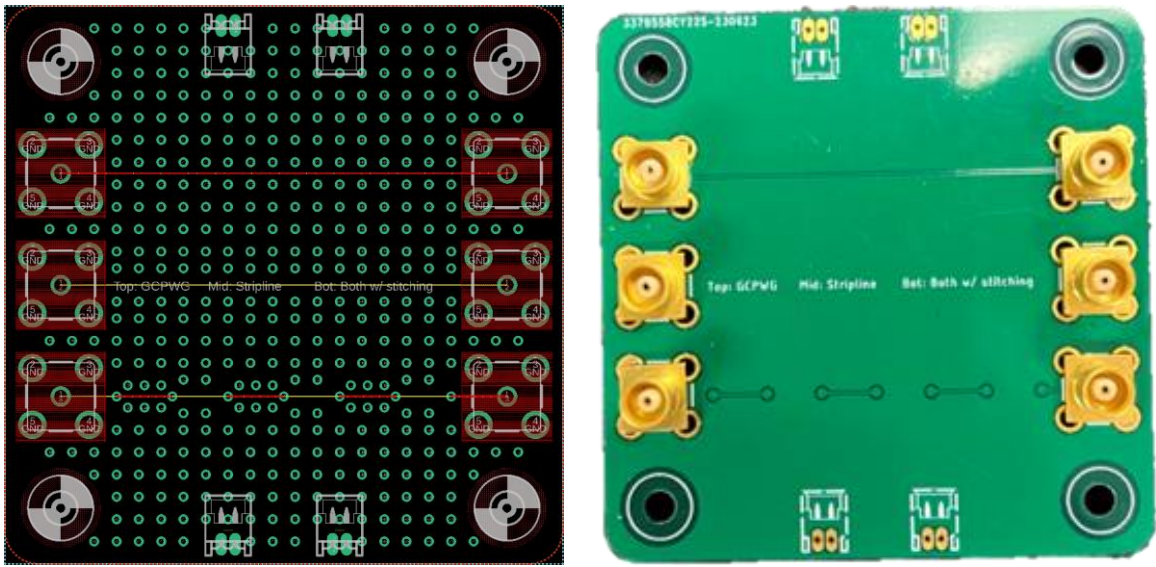
Figure. 5 Circuit layout and PCBA for transmission line testing
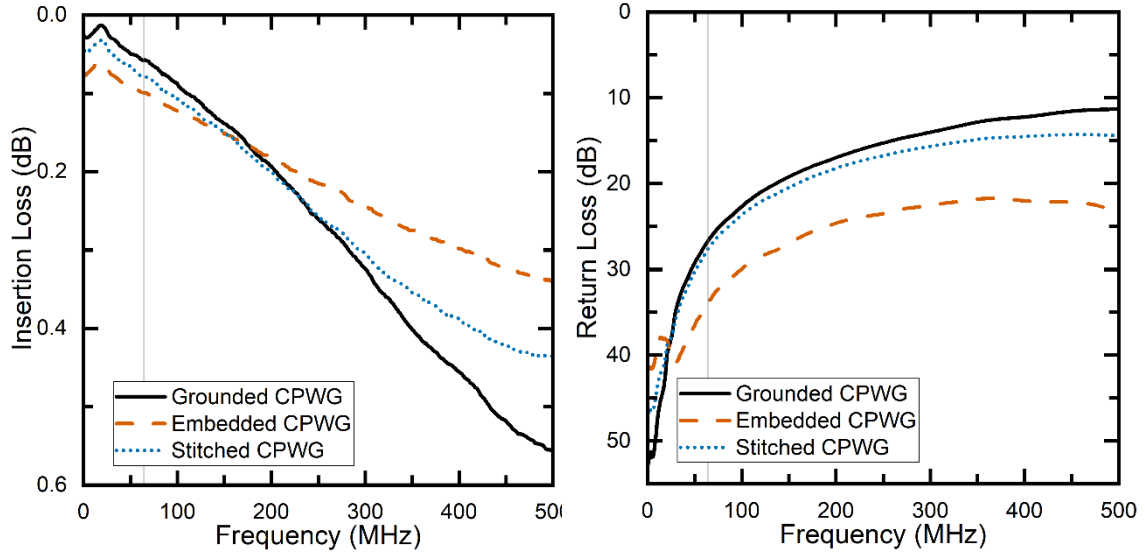
Figure. 6 Comparison of PCB coplanar waveguide return loss and insertion loss

20

2.5.6 Transmission Line Noise Coupling Measurements

A small wide-band near-field H-field loop probe, shown in figure 7, was used along with a spectrum analyzer and an RF signal generator to demonstrate the noise resilience of the embedded coplanar waveguide compared to the grounded coplanar waveguides using the transmission line test PCBA. The spectrum analyzer was connected to one of the ports on the transmission line of interest. The probe was fed a 30 dBm sine wave at 64 MHz and then moved around above the transmission line until a peak RF power was detected on the spectrum analyzer. This peak RF power was consequently captured on the spectrum analyzer. Two plots of the data are below, which have frequency in MHz on the x-axis and RF power in dBm on the y-axis. The left of figure 8 shows the grounded coplanar waveguides at 64 MHz with a peak power of -52.80 dBm and the right of figure 8 shows the embedded coplanar waveguide at 64 MHz with a peak power of -61.95 dBm. Hence, the noise coupling was reduced by 9.15 dB. This reasonably justifies the use of embedded coplanar waveguides alongside the decreased sensitivity to manufacturing tolerances.

Figure. 7 RF Explorer H-field probe used for measuring transmission line noise
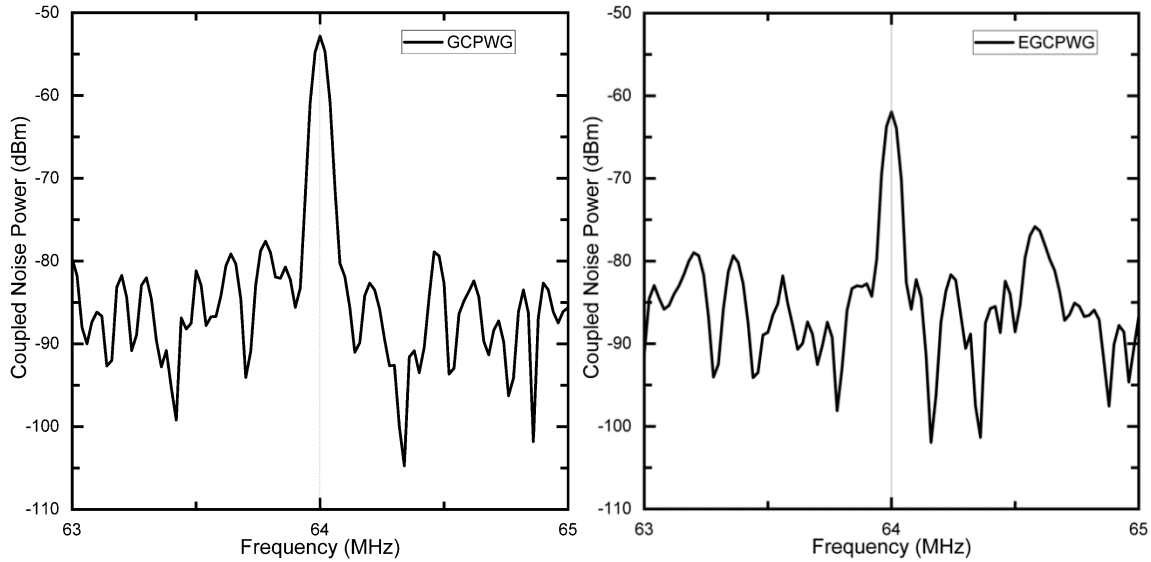
Figure. 8 Coupling spectrum measured of transmission lines on PCBA using probe

2.6 Cable Traps

When working with electrically long coaxial cables, a common mode current appears on the sheath of the cable. This current detunes your coil and increases coil sensitivity, thus necessary to remove for stable repeatable images. In modern consumer electronics, ferrite beads, shown in figure 9, are used to quench the current since they are magnetically lossy. In MRI, however, ferromagnetic materials must be kept away from the MRI scanner for both safety and B_0 field uniformity concerns. A new solution for quenching sheath currents without ferrite beads must be made.

Figure. 9 Ferrite beads photo

Plenty of research has been published on how to remove these common mode currents using tuned "cans," lattice baluns, bazooka baluns, and more [35, 36]. My favorite method is the can method where a section of coaxial cable is wound around a spool. The center conductor and the outer sheath still maintain a transmission line propagating an electromagnetic wave, but now the sheath currents on the sheath see an inductor. Then the center conductors are soldered to SMA ports and the return path conductors are soldered to each other through a capacitor. Since the wounded sheath forms an inductor, you have now introduced a parallel LC circuit that can be tuned to your Larmor frequency to eliminate the sheath currents over a narrow bandwidth, as shown in figure 10.
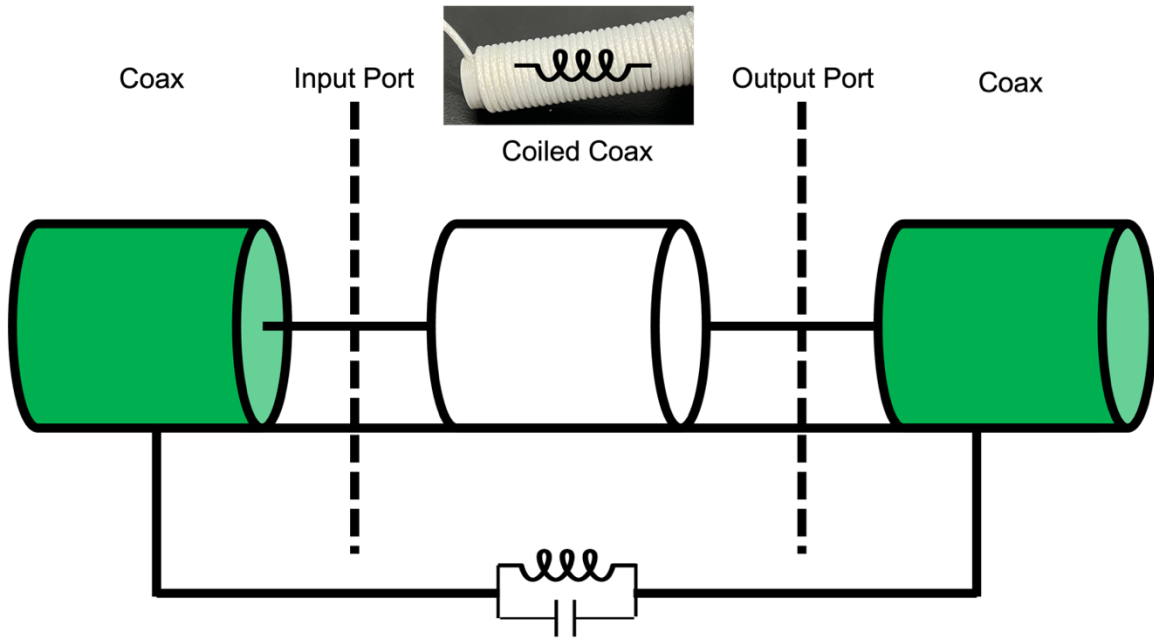
Figure. 10 Cable trap equivalent circuit

To make this process simple, I designed and 3D printed a spool, a can, and a cap. First, SMA ports are screwed into the cap and the can. Next, thin (1.25 mm diameter) coaxial cable is wound around the spool (10 mm diameter) 27 times and threaded through two holes to keep it tightly wound. Then one SMA port is soldered to one end of the coaxial cable center conductor and ground sheath. The spool is inserted into the can so that the other end can also be soldered to the other SMA port before being capped off. Copper tape is stuck around the can and soldered to one SMA port directly but soldered to the other SMA port through a tunable capacitor. The 3D models from AutoCAD and

the final built devices can be seen in figure 11. The manufactured cable trap can be seen in figure 12.
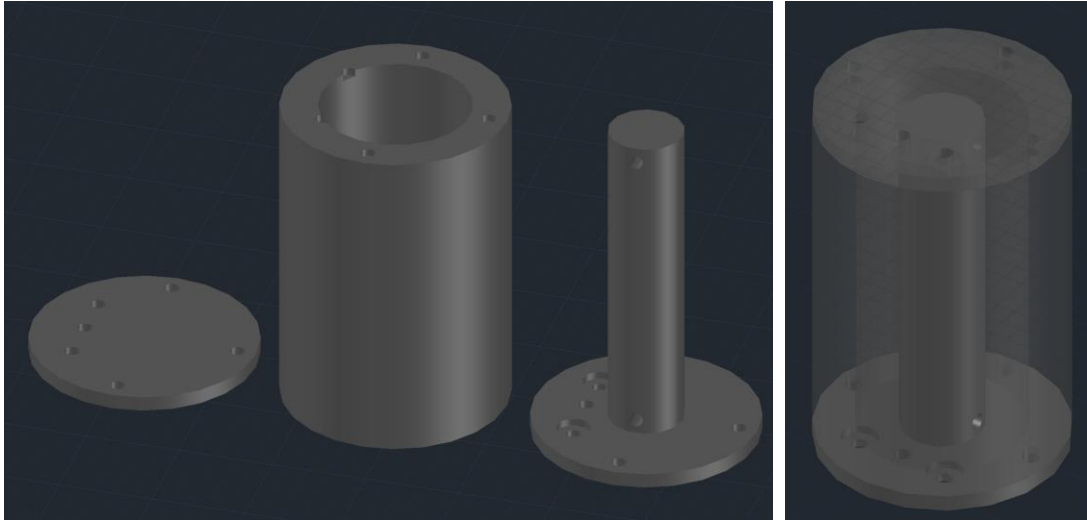
Figure. 11 3D model of cable trap

Figure. 12 Manufactured cable trap photo

The inductance was approximated as 9.89 μH according to equation 16 [37]:

$$L = N^2 R \mu \left[ln\left(\frac{8R}{a}\right) - 2 \right] \text{ H}$$

Equation. 16 Inductance of wound wire

To present a high impedance to sheath currents at 64 MHz, the tunable capacitor is approximated as 62.5 pF using equation 17:

$$C = \frac{1}{\omega^2 L}\,\text{F}$$

Equation. 17 Capacitance for resonance

The insertion loss of the cable trap is shown below in figure 13 to be about 0.5 dB at 64 MHz and the return loss is shown to be about 24 dB at 64 MHz.
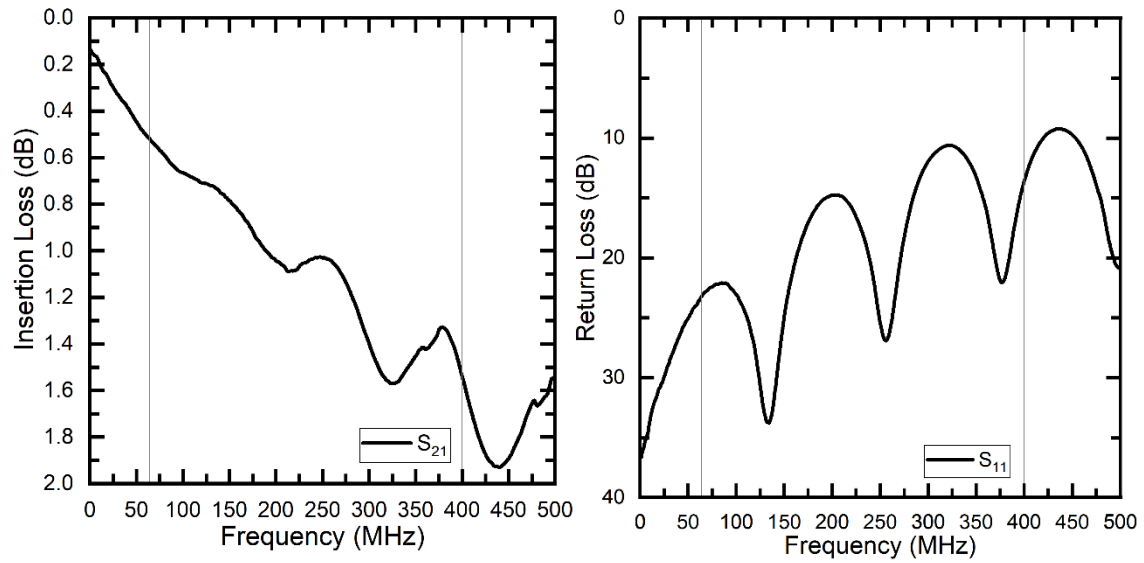
Figure. 13 Cable trap insertion loss and return loss

CHAPTER 3

MRI RF HARDWARE AND PULSE SEQUENCES

As with most systems, MRI machines are large and complex so it is convenient to break them down into smaller digestible pieces. When designing one of these pieces, it is important to understand how their design impacts the final image. Some of the more pertinent pieces for understanding how STAR differs from typical MRI are power amplifiers, low noise amplifiers, and gradient coils, and RF coils.

Power amplifiers dictate the generation of NMR signals, low noise amplifiers impact the reception of NMR signals, and coils play a role in both generation and reception. The importance of the different amplifiers, and how the coils are precisely utilized, however, are both different for STAR.

3.1 Power Amplifiers

Power amplifiers are non-linear RF circuits used in almost every system that transmits an RF signal. Denoted as such since they amplify an RF signal to a high RF power level, they also require high DC power levels to operate. MRI utilizes power amplifiers for transmitting the pulse sequence, thus each transmit channel can contain its own amplifier, as well as for driving the gradient coils. Both applications thus require tight control of how much output power is required for a pulse sequence and the slew rate of the amplifier output to understand the pulse shape. CPC amps, a company specializing in MRI amplifiers, has an excellent blurb regarding power amplifiers in the context of MRI on their website [38].

27

What this means for STAR, however, is antithetic to standard MRI. STAR uses low RF transmit power and slow-switching gradients. This means that the benefits of standard MRI power amplifier design is mut, and their associated trade-offs are problematic. If it were possible to tone-down the output RF power and slew rate of an amplifier, hence making it cheaper, require less DC power, smaller, more linear, and lowering the noise figure, then that would be optimal. This brings us to low noise amplifiers.

3.2 Low Noise Amplifiers

Low noise amplifiers are a ubiquitous RF circuit used in all receiving systems. As their name suggests, their noise figures are extremely low, which constitutes a tradeoff with their DC power consumption, gain, linearity, and output power. For standard MRI, their applications are limited to the receive chain. STAR, however, with its low RF transmit power requirement, allows LNAs to be used in the transmit chain as well. It is arguable whether a low noise transmitter even matters for STAR since STAR should be able to isolate the noise, however, if one were choosing between a high power or a low power device, low power is more sensible [26]. Multichannel STAR also uses LNAs in its cancellation channel, thus lower DC power requirements are favorable at the cost of output power, especially as channel count increases.

3.3 RF Coils

RF coils are responsible for the excitation of spins and reception of signals. RF coils are akin to antennas in modern communication systems, although their intended use and design philosophies are different. The specific term "RF coil" refers back to the

original nuclear induction experimentation where a Helmholtz coil, essentially a physically large inductor, was used for signal reception. Although the term is not entirely dated, since when the term "coil" is used in an electrical engineering context, one associates an interest with a magnetic field, B_1, which is precisely where our NMR signal originates due to the nature of spin. Gradient coils are technically a type of radiofrequency coil as well, however, the nomenclature has stuck for RF coil to refer to volume coils and surface coils, not gradient coils. Also, gradient coil design is not much different for STAR.

Two primary categories of RF coils exist for MRI: volume and surface. Volume coils are often used alone as a transceiver and surface coils are often used in arrays; although other meshed approaches exist too like using a single transmit volume coil in conjunction with two receive coils in quadrature with a hybrid coupler, for example; thus, the system only uses one transmit channel and one receive channel of the console, yet contains three coils. This could be modified to use two independent receive coils too if the console is capable of multi-channel receive. Two loop coils together in quadrate or as separate transmit and receive works too if one would like higher SNR [39]. A table highlighting the differences of both fundamental coil types is below.

Table 1. Comparison of volume coils and surface coils

Volume	Surface
Place around patient	Placed on or close to patient
High B_1 uniformity	Low B_1 uniformity
High B_1 penetration depth	Low B_1 penetration depth
Low B_1 strength	High B_1 strength
Low B_1 sensitivity	High B_1 sensitivity
Generally transceiver or transmit	Generally transceiver or receive

3.3.1 Surface Coils

The most straightforward type of RF coils for MRI is the surface coil, more specifically, the loop coil. It is, quite simply, just a loop of conductive material like copper. The finite resistance of the coil allows tuning and matching capacitors to be used to interface the loop with transmission lines to the rest of the MRI hardware. The loop coil can be represented using a first order approximation as an RLC circuit shown in figure 14. The inductor represents the self-inductance of the coil, the resistor represents the finite resistivity (conductivity) of the conductor used to manufacture the coil, and the capacitor represents the parasitic capacitance of the coil. The impedance of such a coil can be calculated using equation 18.
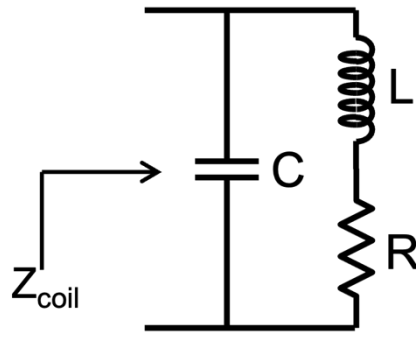
Figure. 14 Loop coil equivalent circuit

$$Z_{coil} = \frac{R}{(1 - \omega^2 LC)^2 + (\omega RC)^2} + j\frac{\omega L\left[1 - \frac{R^2 C}{L} - \omega^2 LC\right]}{(1 - \omega^2 LC)^2 + (\omega RC)^2}\,\Omega$$

Equation. 18 General surface coil input impedance

The finite resistance of coils allows tuning and matching to ensure they can be fed with a 50 Ω coaxial cable. Usually, tuning and matching capacitors C_t and C_m are used in accordance to figure 15, where the previous coil model is shown in the dotted box:
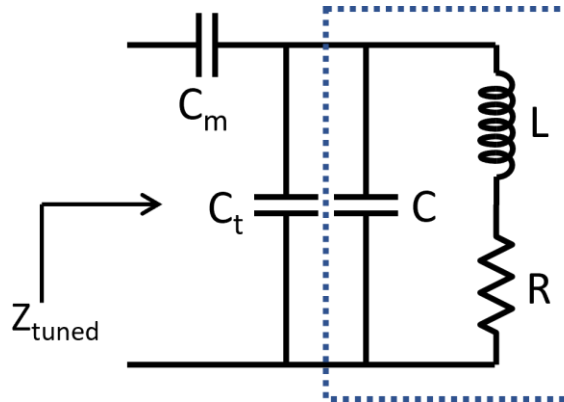
Figure. 15 Loop coil equivalent circuit with tuning and matching capacitors

The parasitic capacitance of a coil depends on its geometry, but it is usually safe to assume that the tuning capacitance is significantly larger. With that assumption ($C_t \gg C$) then Z_{tuned} can be written with the additional matching capacitor as:

$$Z_{tuned} = \frac{R}{(1-\omega^2 LC_t)^2+(\omega RC_t)^2} + j\left[\frac{\omega L\left[1-\frac{R^2 C_t}{L}-\omega^2 LC_t\right]}{(1-\omega^2 LC_t)^2+(\omega RC_t)^2} - \frac{1}{\omega C_m}\right]\Omega$$

Equation. 19 Surface coil input impedance with tuning and matching capacitors

The inductance of a simply loop coil with radius 8 cm, PCB trace width (w) 1 mm, PCB trace height (h) of 35 um, and resistance of 0.5 Ω can be calculated using equation 21 after making an equivalent wire from the PCB trace by matching their cross-sectional areas, as seen in equation 20

$$a = \sqrt{\frac{wh}{\pi}}$$

Equation. 20 Mapping PCB trace to equivalent wire radius

$$L = R\mu\left[ln\left(\frac{8R}{a}\right) - 2\right] H$$

Equation. 21 Inductance of surface loop coil

The inductance was then calculated as 5.37 uH. This would hence require a tuning capacitance of approximately 1.15 pF at 64 MHz using equation 17.

Particularly for human systems, loop coils can be quite electrically large, thus the induced magnetic field is less uniform and less predictable [40]. To combat this, the coil was segmented with capacitors, called distribution capacitors, such that each inductive

32

section of coil is electrically smaller. An example of an 8 cm diameter 1 mm trace width

PCB coil with three distribution capacitors, a built-in matching network, and an SMA

port for 1.5T clinical imaging is shown in figure 16.

Figure. 16 PCB-based surface loop coil

3.3.2 Volume Coils

Volume coils are designed such that they have high B_1 field uniformity

throughout a patient, although the B_1 field is weaker than that of surface coils. This is a

well-documented and suitable tradeoff, considering field uniformity allows the NMR

signals to also be uniformly acquired, thus the MR images have higher contrast without

artifacts; that is, there are not any bright nor dark spots in a large volume i.e. a human

head or torso. A novelty in volume coils began in 1985 when Hayes, et, al. proposed the

"birdcage coil" [41]. Birdcage coils consist of two end rings connected with N legs (rungs). Depending on the placement of ring and leg capacitors, birdcage coils fall into one of three categories: low pass, high pass, or band pass. There exist multiple modes of resonance for birdcage coils, thus the target frequency is not solely excitable [42]. There is one mode, in particular, that is advantageous for imaging; that mode is the one which excites the most uniform B_1 field inside the subject. It has been shown both empirically and mathematically that this mode corresponds to a sinusoidal current distribution through the rungs [43].

Since MRI uses relatively long wavelengths, quasistatic approximations are often used to solve for RF coil parameters, thus Kirchhoff's voltage and current laws can be employed. This is extremely useful for birdcage coils which have many current loops in this approximation. Conveniently, dielectrically loading the coil decreases the wavelength of the signal, thus bettering the approximation. Quite a few approaches exist with varying levels of rigor, some of which have been turned into calculators and programs for rapid development. For a low-pass birdcage, like that used for testing STAR on the bench, an equivalent circuit takes the following form in figure 17.
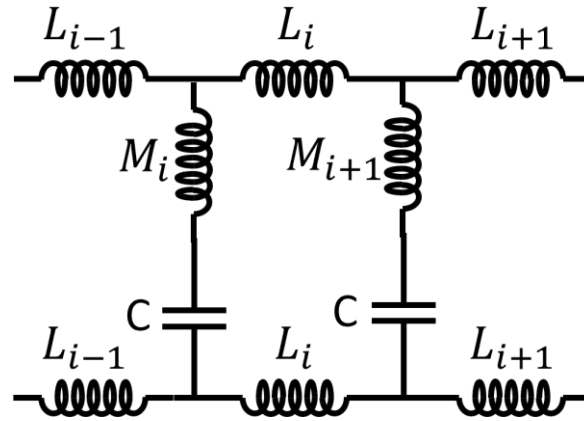
Figure. 17 Low-pass birdcage coil equivalent circuit

The leg capacitors are labeled as C, the end-ring inductors are labeled as L, and the leg inductors are labeled with M to imply that they magnetically couple with adjacent legs. This model can be repeated to represent the entire birdcage until the circuit reconnects with itself and the system can be solved. Shown in figure 18 is a linear low-pass volume coil for 1.5T clinical imaging designed using "BirdcageBuilder" with 33pF leg capacitors [44]. The coil is composed of two sections of a 3D printed frame, sixteen sections of identical PCBs, and a matching board. This modular PCB-printed design allows low-pass, band-pass, and high-pass coils to be made depending on how the user solders the pads together.

Figure. 18 PCB-based volume birdcage coil

3.3.3 Hybrid Coupler vs Power Combiner for RF Coils

Hybrid couplers are used in basic MRI coil systems to change the RF coil system from linear to quadrature. Utilizing quadrature increases the signal to noise ratio (SNR) of the received signal by a factor of $\sqrt{2}$. If we take a moment to remember that proton precession about the z-axis implies rotation in the xy-plane, then intuitively it makes sense that making the choice to use a linear coil would forgo some of your NMR signals. This was previously extensively outlined by Glover, et. al [45].

To demonstrate this visually, a simulation was run in the Advanced Design Simulator (ADS) software from Keysight. This simulation is of a single tone at 64 MHz, corresponding to 1.5T MRI, but the same principle applies for any imaging frequency. The circuit and waveform can be seen in figure 19. On the right side of the circuit we have our two coils, represented by sine wave voltage sources with 1 V amplitudes. The phase of one coil is 0° and the phase of the other coil is 90°. The transmission lines form a 90° hybrid coupler, which then feed two RF output ports. Once steady state is reached, output one is a signal with an amplitude of $\sqrt{2}$, whereas output two is a null, which in MRI would correspond to the transmit port and the receive port, respectively, of the MRI console.

To demonstrate the usefulness of a hybrid coupler compared to a power combiner, the same signals were fed into the two summing ports of a Wilkinson power combiner. The result, as shown in figure 20, is simply a phase-shifted sine wave with the same amplitude, hence an SNR increase has not been demonstrated.
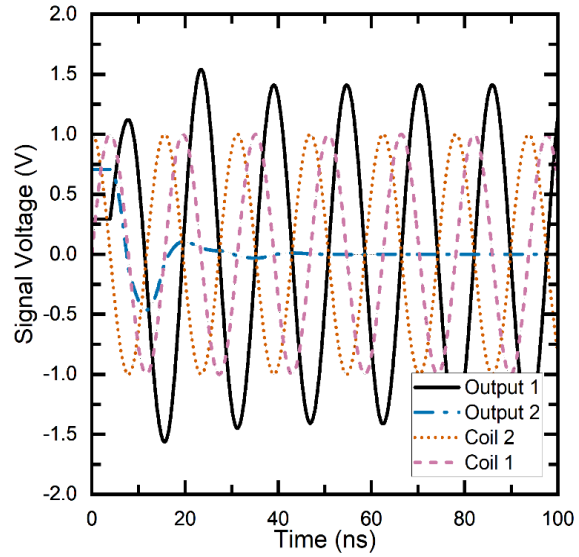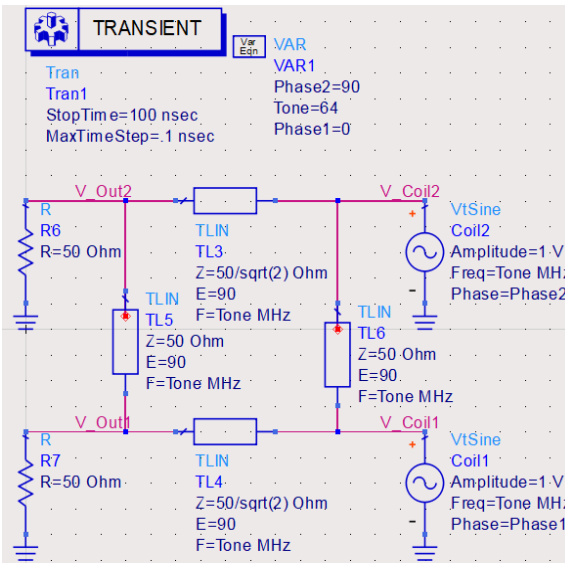
Figure. 19 Hybrid coupler circuit simulation and signals
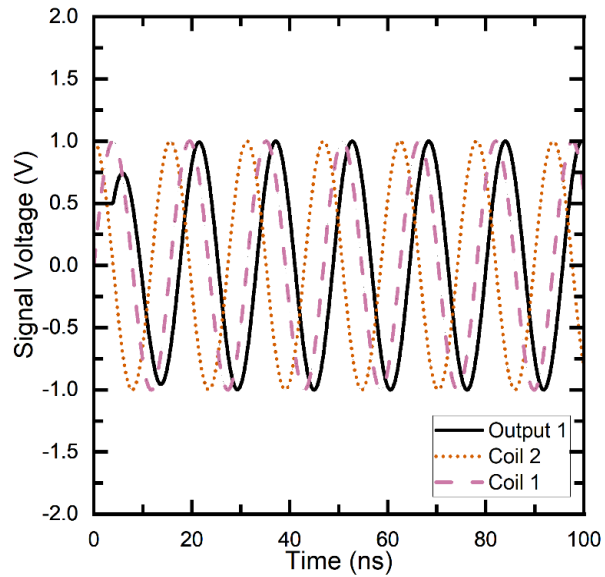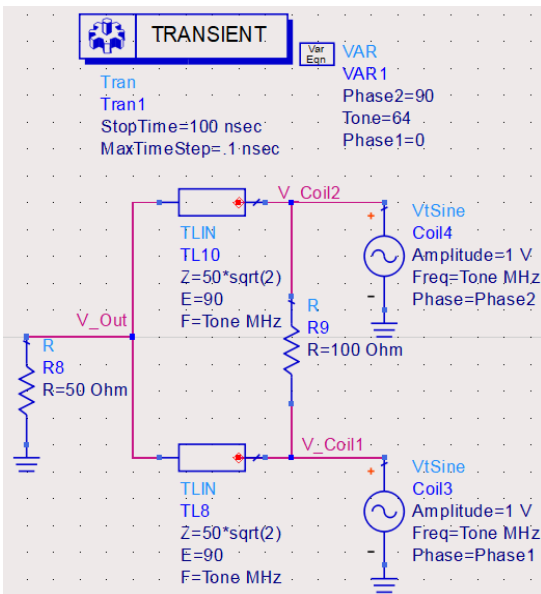
Figure. 20 Wilkinson power combiner simulation and signals

At the frequencies used in MRI, 90° transmission lines are too long for practical fabrication and application. This means that lumped element equivalents must be used instead. Finding these lumped element values is straightforward and easy to think about in terms of ABCD parameters [32]. A standard 90° hybrid coupler requires two 90° transmission lines with $Z = Z_0\ \Omega$ and two 90° transmission lines with $Z = Z_0/\sqrt{2}\ \Omega$. These can be converted into sets of shunt capacitors and series inductors using ABCD parameters as outlined in my coupler paper and shown in figure 21 and equation 22 [my paper].
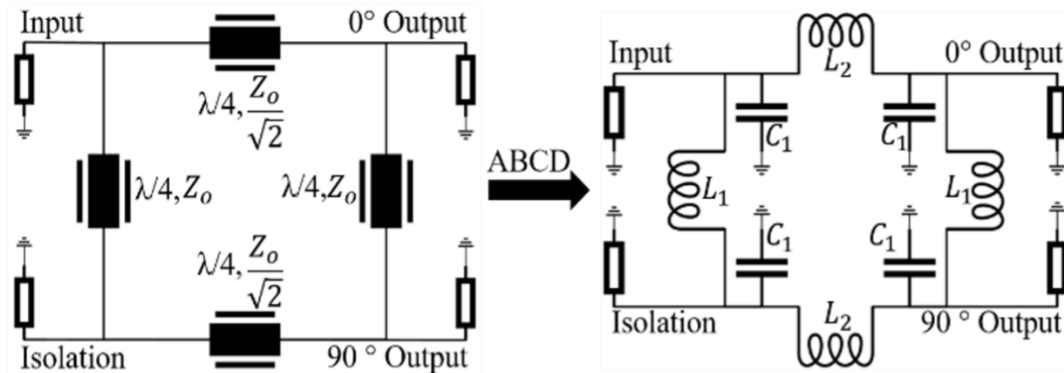
Figure. 21 90° hybrid coupler ABCD transformation

The equation to do so is below, where the left side corresponds to a transmission line with electrical length βl, admittance Y, and impedance Z. Each matrix on the right side corresponds to a lumped component; from left to right they are a shunt capacitor with admittance Y_c, a series inductor with impedance Z_L, and another shunt capacitor with admittance Y_c. Once the capacitor and inductor values are found, a quasistatic approximation can be made to approximate some capacitors as being in parallel, thus reducing component count, and resulting in the circuit shown on the right of figure 21.

$$\begin{bmatrix} \cos(\beta l) & jZsin(\beta l) \\ jYsin(\beta l) & \cos(\beta l) \end{bmatrix}_{90°} = \begin{bmatrix} 1 & 0 \\ Y_C & 1 \end{bmatrix}\begin{bmatrix} 1 & Z_L \\ 0 & 1 \end{bmatrix}\begin{bmatrix} 1 & 0 \\ Y_C & 1 \end{bmatrix}$$

$$Y_C = j\omega C$$

$$Z_L = j\omega L$$

Equation. 22 ABCD matrix transformation of transmission lines to lumped elements

3.4 Pulse Sequences

In 1966 Ernst showed sensitivity increases for pulsed MRI. As a result, continuous wave MRI was nearly abandoned outside of NMR spectroscopy. The classic spin echo is a fair choice to introduce the concept of pulse sequences. Following this discussion is gapped SWIFT and finally continuous SWIFT.

Gradient coils are used not only to shim the B_0 field, but also to encode spatial information by slightly varying the frequency and phase of isochromats within a slice of tissue. This allows a contrast between voxels, where the slice is selected with the z-gradient by linearly varying the total B_0 field on the z-axis, thus precession frequency. Frequency is also encoded with the x-gradient and phase is encoded with the y-gradient. The parallels to modulation in communication systems are that slice selection gradients change the carrier frequency, whereas frequency and phase gradients, respectively, modulate frequency and phase. The unique combination of x, y, and z gradients at any point in space containing isochromats defines our voxel dimensions.

Different pulse sequence require different shapes, power levels, and duration of RF pulses [46]. These parameters define the power amplifiers required for imaging, the SAR tissue experiences, and the power handling requirements of other RF hardware.

3.4.1 Spin Echo

Understanding spin echoes provides a fundamental basis for understanding pulse sequences in general. The spin echo was the first pulse sequence to be created and paved the way for dozens of modern pulse sequences. The gradient coils ($G_s = G_z$, $G_\varphi = G_y$, $G_f = G_x$) are used to select the voxel. The z-gradient linearly changes the frequency of the spins throughout the imaging area, thus defining our slices. The x-gradient and y-gradient then spatially encode information within the selected slice. Classically, the x-axis is frequency encoded and the y-axis is phase encoded. First a 90° pulse applied in the xy-plan knocks the spins (now called isochromats) off the z-axis into the xy-plane. They begin to dephase due to small variations in Larmor frequency within the slice and after time TE/2 ms, a 180° pulse is applied, thus they begin to rephase. After TE/2 ms they are perfectly rephased and generate the peak of a signal, referred to as the echo as shown in figure 22. It is important to note that generic square pulse were shown in the figure, however, pulse shaping and its consequential effects on k-space trajectory are a rich field of study.
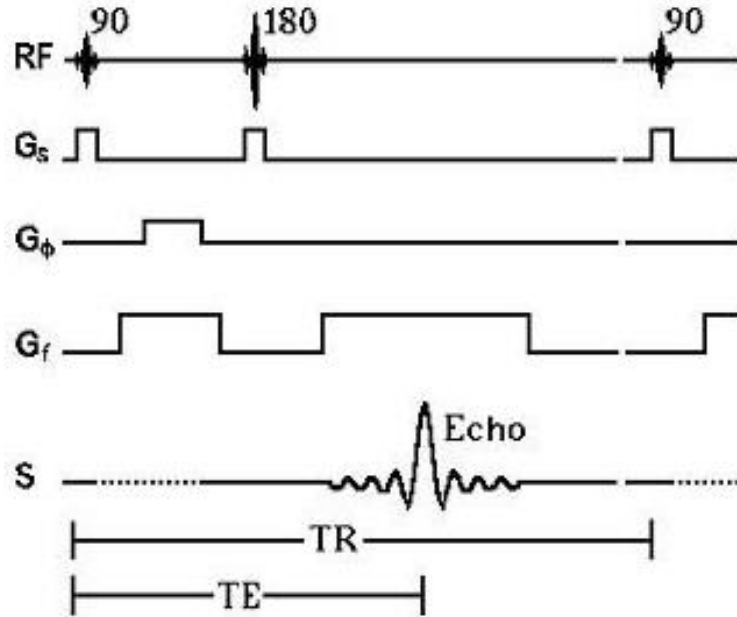
Figure. 22 Spin echo pulse sequence timing

3.4.2 Continuous Sweep Imaging with Fourier Transform (SWIFT)

Although pulsed MRI is the current industry standard, adiabatic pulse sequences still carry unique advantages over pulsed MRI and have been in the second stage spotlight again for a couple of decades. In 2006, the SWIFT pulse sequence was invented at the Center of Magnetic Resonance Research [47]. Shortly after in 2012, SWIFT was modified to develop continuous SWIFT, which thus far has been the only sequence used in my STAR work [8]. As previously mentioned, simultaneous transmission and reception of NMR signals provides two primary advantages: first, the RF coils do not undergo ringdown or dead time, thus NMR signals from tissues with a short T_2 are able to be acquired, unlocking contrast for otherwise MR-invisible tissues. Second, the sequence requires significantly less RF peak power so the hardware can be smaller,

42

cheaper, require less DC power, and more portable. Figure 23 below shows a simple signal comparison between continuous wave and pulsed MRI. The left is continuous wave MRI where the transmit signal is more than 70 dB larger than the receive signal. The right shows a typical pulse sequence with a large transmit signal that is time-duplexed with the receive signal, thus introducing ring down. The higher the Q-factor of the coil, the longer the ringdown, thus coils with intrinsically less resistive noise and consequently higher intrinsic SNR, become even less suitable for short T_2 imaging outside of unique pulse sequences like continuous SWIFT [48].
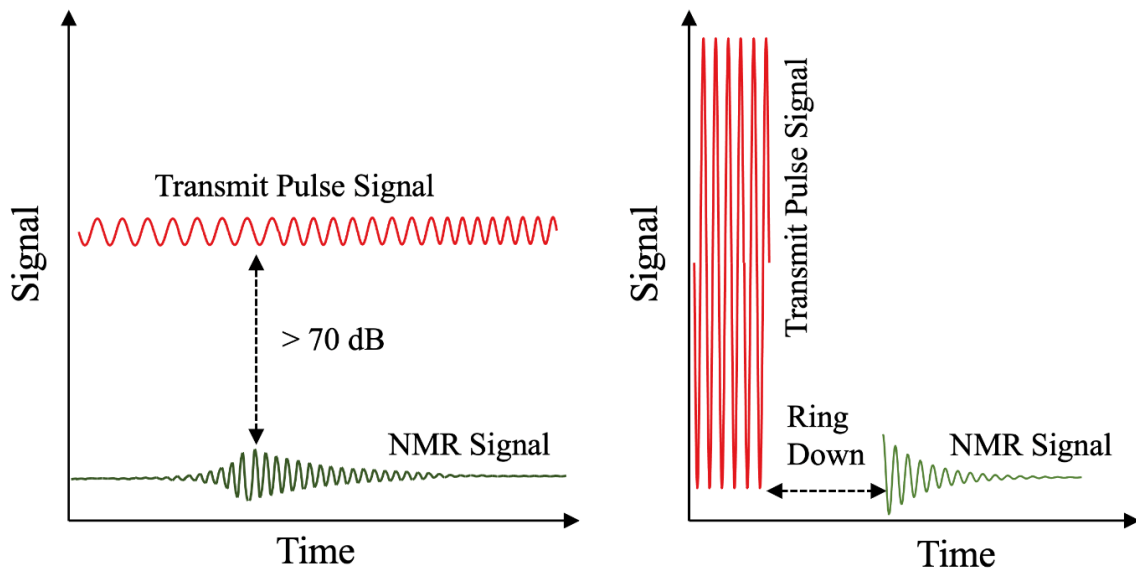
Figure. 23 Continuous wave vs pulsed pulse sequences

The pulse sequence for continuous SWIFT is shown in figure 24 with generic square pulses. The slice selection gradient first chooses the slice, then the continuously applied RF transmit pulses, phase encoding gradient, frequency encoding gradient, and receiver are engaged until the next slice needs to be selected.
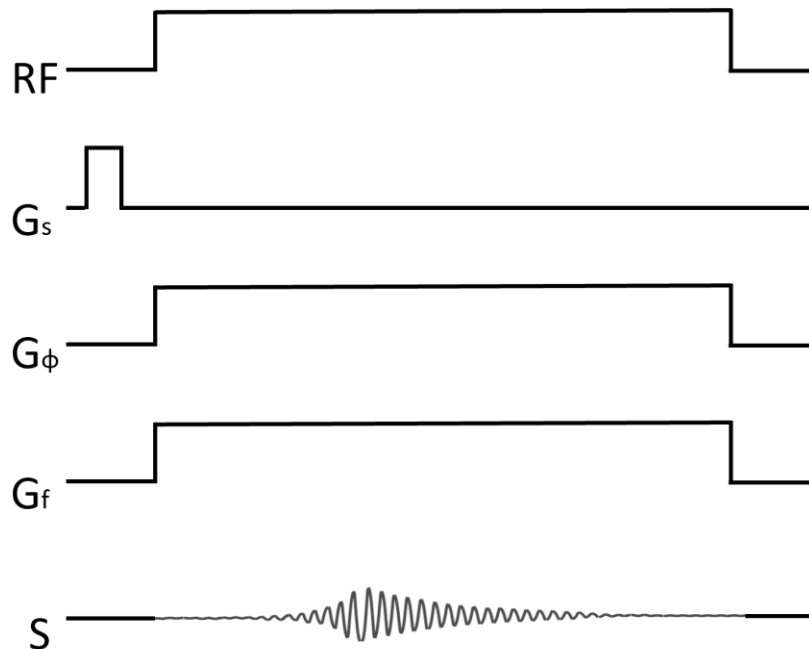
Figure. 24 Continuous SWIFT pulse sequence timing

For long T_2 tissues, like those used in standard imaging, the leakage signal is approximately linearly additive to the NMR signal. This marginally relaxes the isolation requirements of STAR, since digital isolation is also part of the isolation stack amongst other techniques. For short T_2 materials, however, the leakage signal becomes increasingly non-linearly additive to the NMR signal, requiring a more cumbersome

digital isolation effort including polynomial curve fitting. This further qualifies that the

primary intention of STAR is to provide high and stable isolation but other features could

enhance a STAR ecosystem in the future once its core intentions are met.

CHAPTER 4

SIMULTANEOUS TRANSMIT AND RECEIVE (STAR)

4.1 Simultaneous Transmit and Receive Introduction

Simultaneous transmit and receive is a multi-faceted technology with requirements extending unique hardware, software, and MRI pulse sequencing. Also denoted as "concurrent excitation and acquisition (CEA)" in the MRI community or more generally understood as "continuous-wave full-duplex" or "frequency-modulated continuous wave;" the basic concepts extend beyond just MRI. Herein exclusively referred to as STAR, the relationship between STAR and MRI begins in the infancy of NMR experimentation.

Felix Bloch first published his NMR experimentation with continuous wave technology in 1946 out of Stanford. The signal acquired was, of course, not used for spectroscopy or image reconstruction, however it formed the basis of modern MRI; specifically with a continuous-wave signal acquisition method.

The basic definition of STAR is self-explanatory, signals are transmitted and received over the same bandwidth and during the same time interval. What this means for technology, however, is more complicated and nuanced. For MRI there are two fundamental concepts to understand for STAR: exciting and acquiring an NMR signal with a continuous-wave pulse sequence and isolating the receiver from directly receiving the transmitted pulse sequence. Continuous SWIFT demonstrates the former, whereas STAR enables the latter. Everything beyond these two concepts is merely an extrapolation or improvement of the fundamental technologies.

4.2 STAR Key Concepts

Since STAR, by definition, is a continuous wave technology, there is an inherent signal from the transmitter being leaked into the receiver. This signal, the "leakage signal," is extraordinarily problematic for image reconstruction since it saturates the pre-amplifier, saturates the console analog to digital converter (ADC), and masks the NMR signal with excessive noise. Without this leakage signal, STAR as a technology would not be necessary and continuous wave MRI would produce excellent images without supporting technologies. Alas, the leakage signal is fundamental to any pair of transmitters and receivers in such proximity.

Assuming the leakage signal takes the form $A_L e^{-j(2\pi ft + \varphi_L)}$ where A_L is amplitude, f is our Larmor frequency, t is time, and φ_L is phase, then an introduced *cancellation signal* takes the same form as $A_c e^{-j(2\pi ft + \varphi_c)}$. If we combine these two signals with the intention of undergoing destructive interference, it becomes apparent that $A_L = A_c$ and $\varphi_c = \varphi_L + 180°$. This leads one to see that the amplitude and phase of the cancellation signal must be able to be independently manipulated to match an arbitrary leakage signal and the cancellation signal strength must be strong enough to match the leakage signal strength.

4.3 Previous Works in STAR

The first demonstration of STAR imaging was in 2012 with the introduction of continuous SWIFT for a 4T system [8]. This paper directly evolved continuous SWIFT from gapped SWIFT, which was introduced in 2006 [47]. The paper compared the two pulse sequences, RF peak power, image quality, hardware implications for STAR, and

more. The system did not contain any active components, rather, just a hybrid coupler feeding a coil with tediously tuned matching and tuning capacitors to produce high isolation, thus making it applicable only for inanimate objects. The term "leakage signal" was coined, hence outlining the fundamental issue with attempting STAR imaging. SWIFT, in general, was used in other applications before continuous SWIFT was introduced, such as for dental and breast imaging [49, 50]. This alludes to the fact that STAR MRI can be advantageous in any application where SWIFT has been applied and beyond.

In 2015, a CEA paper was published using a transmit loop coil, a receive loop coil, and a decoupling (transmit) coil for 3T in-vivo imaging [23]. The amplitude and phase of the decoupling coil was tuned to destructively interfere with the leakage signal coupled to the receive coil. This was an excellent first demonstration of introducing new hardware into an MRI ecosystem to remove the leakage signal, although, it would be further advantageous to not require introducing new coils.

Shortly after, in 2016, a paper was published outlining how a voltage-controlled phase shifter and voltage-controlled attenuator could be manually tuned with a transceiver coil to interfere with the leakage signal, thus forming a sort of cancellation channel for in-vivo 4T imaging [21]. This formed the basis for explicitly manipulating the phase and amplitude of a cancellation signal through a circuit channel, rather than through a decoupling coil. The same team later refined their approach for determining the phase shifter and attenuator control voltages required for imaging by using a field programmable gate array (FPGA) to implement a calibration algorithm to determine the

control voltages [22]. The system required console interaction and a remote user board with the sole functionality of telling the system to calibrate itself was introduced.

CEA came back in 2018 in two papers using loop coils for 3T [24, 25]. The first introduced a vector modulator for the cancellation channel; that is, a four-tap cancellation channel where all taps are orthogonal to one another (0°, 90°, 180°, and 270°). This allowed weighing functions (control voltages) to be applied to voltage-controlled attenuators in the vector modulator using a Raspberry-Pi controller. Shortly afterwards, they performed in-vivo imaging using a similar system, but with a single-tap cancellation channel and Matlab interface. These both worked well in terms of isolation, but the fundamental problem of modern STAR hardware was still apparent: STAR imaging lacks resolution and has a surplus of noise.

In 2020 we presented an abstract on a passive tunable decoupler that could be manually tuned using variable capacitors and inductors to isolate transmit and receive channels [51]. The circuit was extremely sensitive to tuning parameters, difficult to work with, thus lacked most functionality of current STAR systems. It was, however, compact and passive, therefore it could readily integrate into a coil frame, thus theoretically has future applications in something like a "fully integrated STAR coil system." A similar and less sensitive circuit was published in 2008 [52].

The first paper to pay special attention to noise was published in 2020 [26]. Rightfully so, it tackled spurious transmit noise, its sources, how it affected the dynamic range of the receive chain, and how a well-designed STAR system should be able to adequately handle spurs. They also demonstrated the isolation degradation due to movement and discussed the importance of STAR isolation bandwidth. STAR systems

thus far, including my own, have extremely low bandwidths since they are tuned to just the Larmor frequency. Sohn et. al increased isolation bandwidth by using a coupler to feed energy into the coil and sending the backwards-coupled signal into the cancellation channel, thus the signal now carries information regarding the coil tuning and matching, which can be readily manipulated as well by the cancellation channel [21]. I have previously attempted to increase bandwidth through "Q-spoiling" the isolation of a transceiver system. In other words, by intentionally lowering the STAR isolation, the peak isolation decreases but the bandwidth increases. Reasonable success was found on the bench but imaging was never possible and current STAR work still prioritizes high and stable isolation.

Another promising method of uniquely implementing STAR was demonstrated in 2021 by using a switched transmission circulator to implement a gyrator between the transmit and receive paths, which was later demonstrated for applications in communication electronics as well [53-55]. Various other methods of coil and antenna decoupling have been reported, such as parasitic elements and dielectric loaded coils too [56-58].

Standalone STAR was published in 2023 to kickstart the development of feature-rich STAR systems and forms the basis for multichannel STAR, both of which are outlined in the proceeding text.

4.4 Standalone STAR

This section outlines the published single channel standalone STAR system and also forms the basis for the multi-channel standalone STAR system [27]. Standalone self-calibration is defined such that the STAR system does not require any externally applied RF or control signals from the console to calibrate. This allows the STAR system to be retrofitted with as many MRI machines and coil configurations as possible. Although, other control signals from the user are required through a wireless userboard, such as tuning the center frequency of the system and beginning calibration.

4.4.1 Standalone STAR System Outline

The basic system can be broken down into seven fundamental sub-systems, which exclude the console and coils. The first sub-system contains the microcontroller and FPGA for algorithmic decision making and establishing a user interface. This also includes the onboard ADC of the FPGA for output signal power detection. The second sub-system is the digital to analog converters used to allow the FPGA to control the cancellation channel devices with analog control voltages. Third is the voltage-controlled oscillator and filter for generating our calibration signal during calibration, which is shut off for imaging. Fourth is the RF switch and power splitting board that interfaces STAR with the MRI console and determines whether the calibration signal path or the imaging signal path is enabled. The chosen input path is then split, thus sending one signal to the cancellation channel and another signal to the coil system. The fifth system is the two-tap cancellation channel where each tap contains a single voltage-controlled phase shifter and a single voltage-controlled attenuator. Sixth is the Wilkinson power combiner and filter

that combines the signals from the cancellation signal and receive RF coil. The combined

output is sent to the power detection system for qualifying the leakage signal. Finally, the

last sub-system is the power detection circuit used to communicate the leakage signal

power level to the onboard ADC of the FPGA.

A block diagram of the STAR system is shown in figure 25 and the figure of the

physical system from the paper is reproduced in figure 26, but the discussion of the

STAR circuits will be saved to be discussed in detail in *4.5.3 Multichannel STAR*
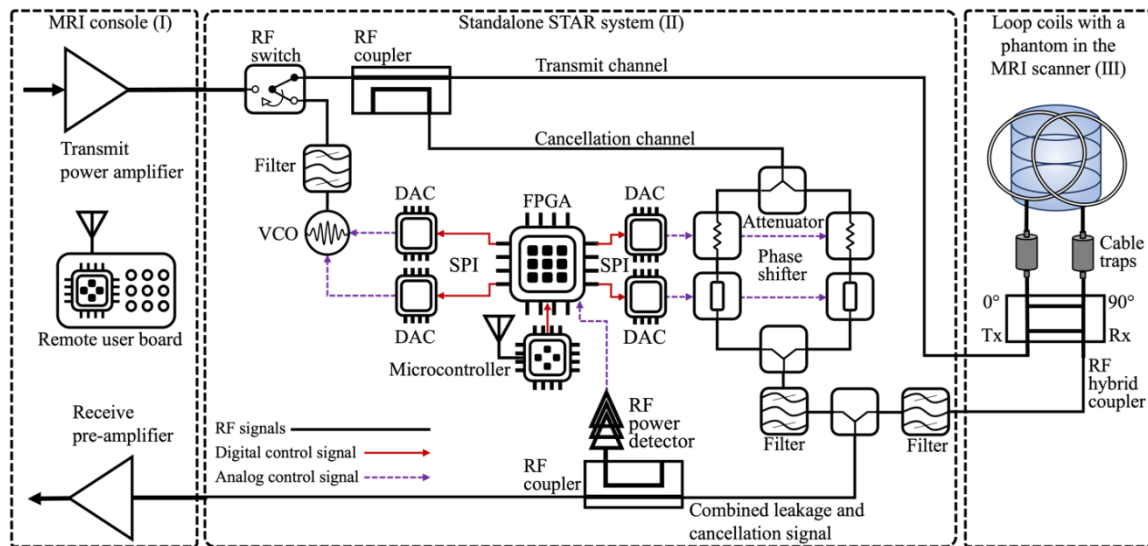
Circuitry.

Figure. 25 Original standalone STAR system block diagram
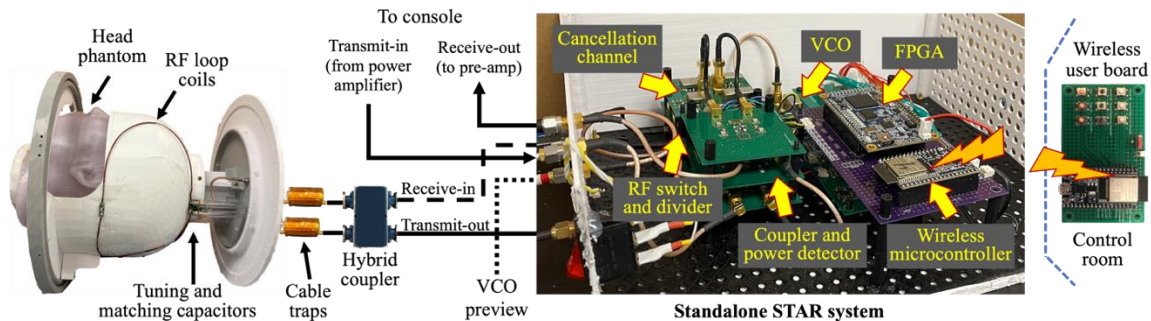
Figure. 26 Original standalone STAR system physical circuits and coils

The user can interface with the STAR circuitry using a remote user board with the following functions: increase/decrease voltage controlled oscillator (VCO) control voltage, increase/decrease phase shifter control voltage, increase/decrease attenuator control voltage, begin calibration, enter power-down mode, reset, and change digital to analog converter (DAC) resolution. Originally, this user board was a physical PCB containing a microcontroller and some pushbutton inputs. This worked well, however, was difficult to upgrade for future functionalities like multi-channel, thus has been replaced with an Android app. A photo of the physical PCBA user board originally used is shown below in figure 27, and a photo of the first Android app replacement is in figure 28.
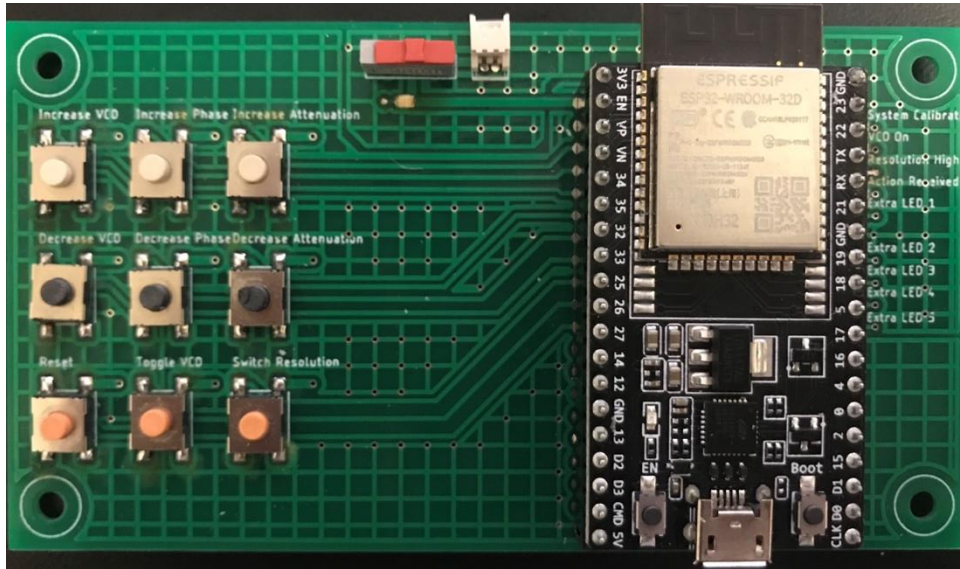
Figure. 27 PCB-based user board with ESP32 microcontroller
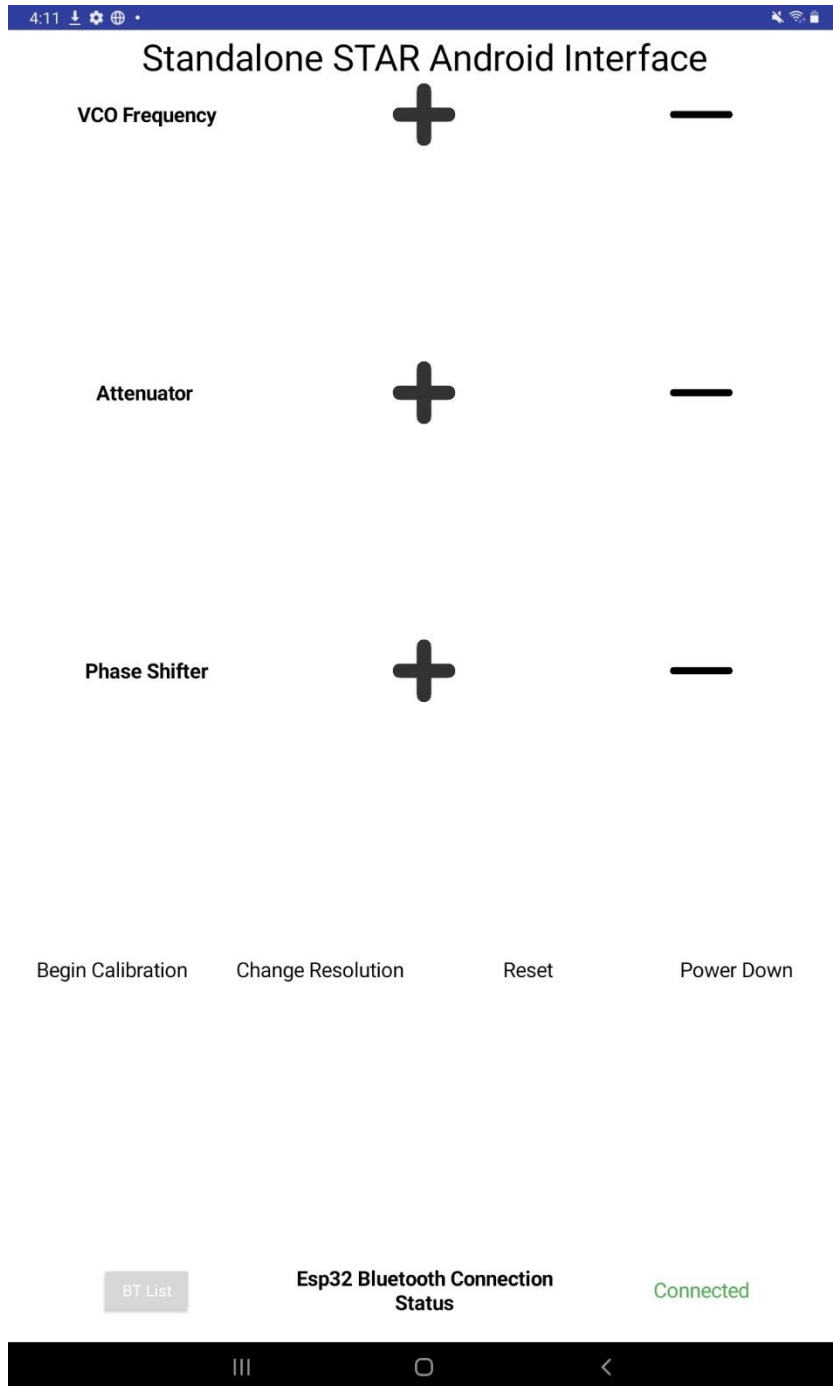
Figure. 28 Android application user interface for standalone STAR

Three different coil systems were tested with standalone STAR. The first consisted of two loop coils using a hybrid coupler, thus they operated in quadrature. The second was a single linear birdcage coil operating alone as a transceiver. A hybrid coupler was used here as well, although not for quadrature, rather, just for isolating the transmit and receive ports of STAR. The third was using the linear birdcage coil as a transmitter along with a loop coil as a receiver since one intention from the original standalone STAR publication was to demonstrate the feasibility of not only transceiver coil STAR but also STAR using separate transmit and receive coils. This paved the way for multichannel STAR since the efficacy of STAR without the added isolation of a hybrid coupler was demonstrated. The loop coil and birdcage coil are reproduced in figure 29 alongside the combination of the two.

Figure. 29 PCB coils used in standalone STAR

The isolation for the original system data with the quadrature copper loop coils, single linear birdcage coil, and separate birdcage transmit coil with a receive loop coil, can also be seen below in figure 30 from 60 MHz to 70 MHz and tabulated in table 2 for 63.7 MHz. Clearly, the isolation is first at some nominal value with just the coils due to geometric isolation, then increases once the hybrid coupler is added, increases again from STAR, and maximizes from the userboard.
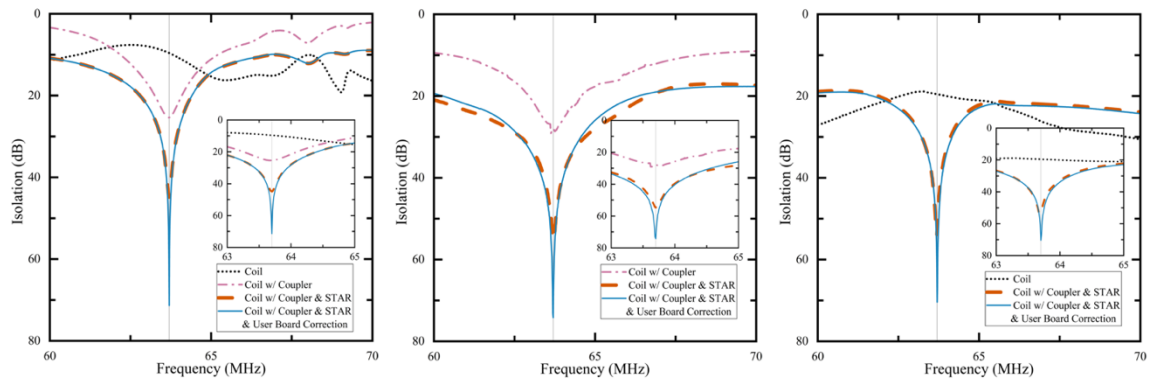
Figure. 30 Standalone STAR isolation for three coil systems

Table. 2 Standalone STAR isolation data for 63.7 MHz

RF coil	Geometric Decoupling	Hybrid Coupler Isolation	STAR Automatic Isolation	STAR Userboard Isolation
Two Loop	9.6 dB	25.4 dB	44.8 dB	71.3 dB
Linear Birdcage	NA	28.0 dB	54.6 dB	74.2 dB
Linear Birdcage with Single Loop	19.5 dB	NA	52.7 dB	70.4 dB

When using quadrature feeding for many coils, the concept of phase arrays naturally arises. Hybrid couplers find their home with two quadrature loop coils or a quadrature-fed birdcage coil. However, the concept of quadrature can be extended to four loop coils as well (or even sophisticated birdcages) if the phase of the coil feeds are 0°, 90°, 180°, and 270°. This requires a feeding mechanism capable of producing such phases with approximately equal magnitudes. The solution I have presented was referred to as an *extended coupler* [59]. That is, an eight-port coil feeding circuit that brought together many discrete hybrid couplers in a small formfactor to readily feed a four-coil system, whose schematic and PCBA are shown below in figures 31 and 32 with component values tabulated in table 3 and scattering parameters in figure 33.
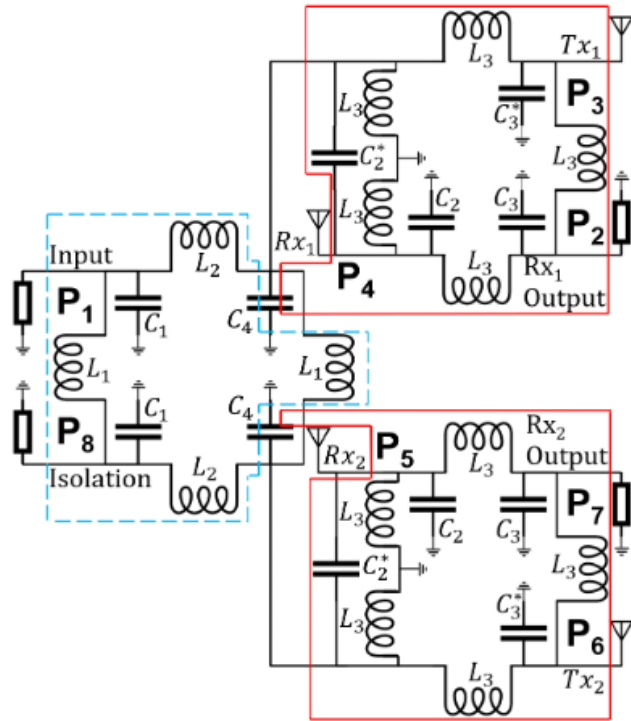
Figure. 31 Extended eight-port coupler schematic
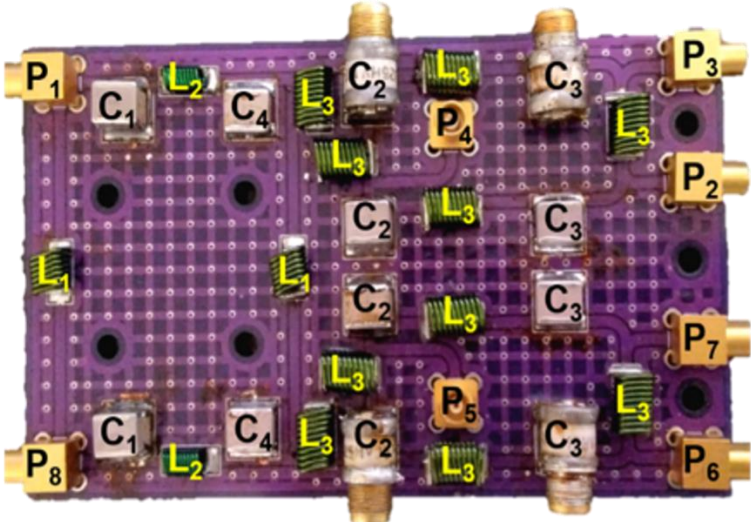
Figure. 32 Extended eight-port coupler PCBA

Table. 3 Extended eight-port coupler component values

Component	Calculated Value	Physical Value
C_1	120.072 pF	121 pF
C_2	35.169 pF	48 pF
C_2^*	35.169 pF	24 pF
C_3	70.337 pF	75 pF
C_3^*	70.337 pF	62 pF
C_4	155.241 pF	150 pF
L_1	124.339 nH	110 nH
L_2	87.992 nH	82 nH
L_3	175.843 nH	180 nH
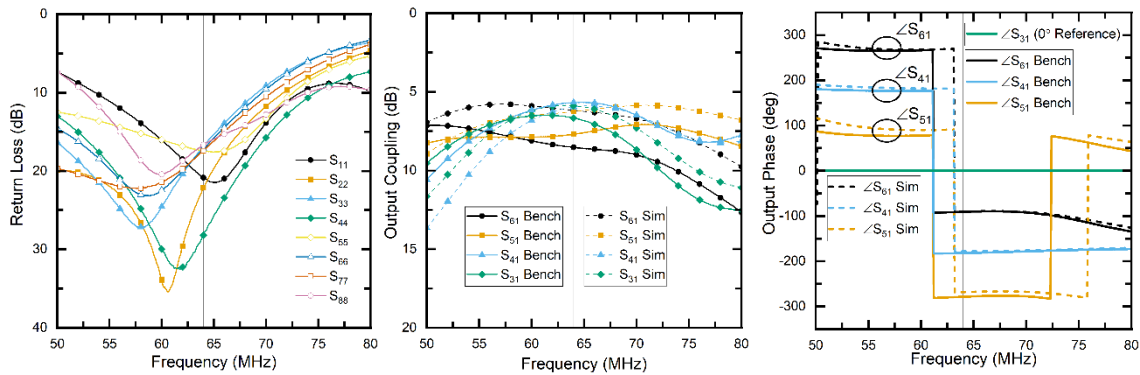
Figure. 33 Extended coupler scattering parameters

All three plots extend from 50 MHz to 80 MHz. The left plot shows the measured return loss of all eight ports from 0 dB to 40 dB, where it can be seen that all ports are impedance matched well enough to have a minimum return loss of 16 dB at 64 MHz. The middle plot shows the coupling factor of the output ports to the input port in both simulations and on the bench. By definition, the minimum coupling factor from splitting energy between four ports is 6 dB, as shown by the simulations, and the worst-case

scenario for the measured data is 8.5 dB. The final plot shows the phase of the output

ports with port three used as the reference. Clearly, the bench measurements match well

with the simulations to make four orthogonal ports.

4.4.2 System Functionality

The system begins by booting-up the electronics from the power supply,

whereafter, the FPGA establishes control over the DACs and tells the RF switch to

enable the calibration signal path. The VCO is now outputting a sinusoid at

approximately 64 MHz. Each MRI machine operates with a slightly different magnetic

field strength, thus different Larmor frequency, so the user may use the user board to tune

the VCO output frequency (optionally viewable with an oscilloscope) to match the exact

machine. Once the VCO frequency matches the bore, the user presses a button to tell the

system to begin calibration. After the system finishes calibrating itself, it immediately

disables the VCO and enables the console RF path with the RF switch; upon which, the

user may view the isolation on the console. If they are not satisfied with the isolation,

they may increment and decrement phase shifter and attenuator control voltages until

isolation criteria have been met. Once satisfied, they can either begin imaging with the

console or tell the STAR system to enter a low power mode first, then begin imagining. A

block diagram of this procedure is shown in figure 34.
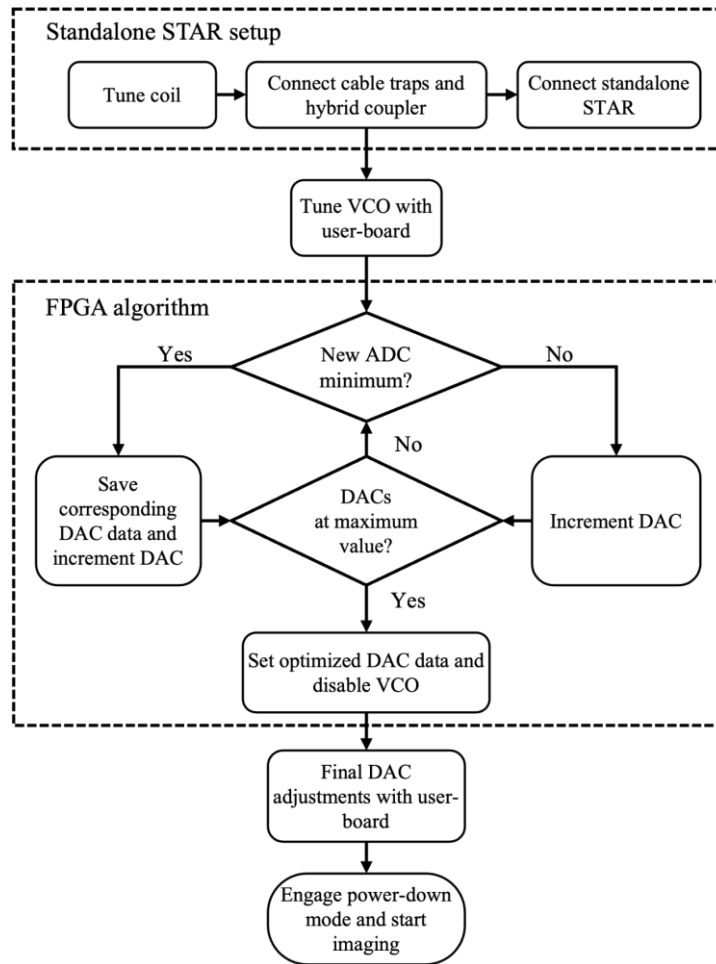
Figure. 34 Standalone STAR calibration flow chart

STAR imaging was performed using the system and coils shown in figure 26 with

approximately 40 mW (16 dBm) of RF peak power. Imaging was first performed with a

resin-based human head phantom containing approximately 2 L of water, 260 g of sugar,

and 3 g of salt thus approximating the human brain tissue dielectric properties of $\varepsilon_r = 82.6$

and $\sigma = 0.4$ S/m at 64 MHz [60, 61]. Figure 35a shows this initial image, which is

extremely noisy. This noise was combatted by employing the low noise mode for the

FPGA and microcontroller and imaging was done again, producing the image in figure

35b. Clearly, the noise was greatly reduced and the system was ready for in-vivo

imaging. A human subject was consequently imaged and this produced the image in

figure 35c. The most noticeable issues with this image is the noise, low signal intensity in

tissue, and the bright spots from a nonuniform coil. It is difficult to point to exactly what

caused such low quality images but the high-level next steps were clear: increase signal

intensity and decrease noise.
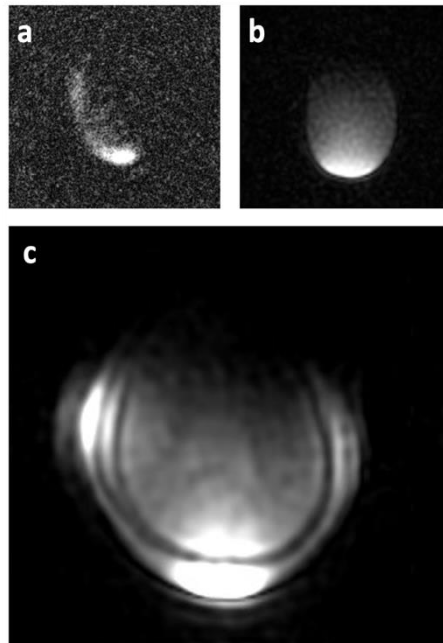
Figure. 35 Standalone STAR images of a head phantom and in-vivo

4.4.3 Standalone STAR System Discussion

The original standalone STAR publication used two cancellation channel "taps" to manipulate the cancellation signal. Each tap contained a single voltage-controlled attenuator and voltage-controlled phase shifter, and the output of each tap was combined to form a single cancellation signal. Conceptually, two taps allowed imaging power to be increased by 3 dB, enabled two phase shifters with 270° ranges to be used in parallel to cover the full unit circle, and allowed the "Q-spoiling" technique to be attempted by intentionally mismatching phase shifter control voltages. The paper, however, did not take advantage of the potential advantages of this two-tap system; the control voltages of both phase shifters were equal and the control voltages of both attenuators were equal. A 360° phase shifter, or pair of phase shifters would mitigate this strategy anyway. The primary advantage to orthogonal taps, in my opinion, would like in using four fixed taps at 0°, 90°, 180°, and 270°, thus increasing linearity, power handling, and matching. At first, this appears to reduce losses too, however using four taps requires six power dividers/combiners, hence requiring an LNA in the channel, which is an appropriate solution.

The cancellation channel method worked well for isolating the leakage signal, although with a limited phase range of 200°. This implied that two sets of cables were required to compensate for the lack of complete phase range for standalone STAR to guarantee a calibration state where the leakage signal is highly isolated. As a result, even though standalone STAR worked well, it ended up feeling a bit lackluster. The

multichannel system thus uses two series phase shifters in the cancellation channel to achieve a 360° range for each channel.

The limited range of the cancellation channel lacks feature, however, it is not the system fatal flaw; the compensation was not preferable yet possible and the solution for the next generation was feasible. As can be seen in the MR image, the unpredicted fatal flaw of the system was noise. If it is assumed that the MRI room is a Faraday cage, then the noise must have been internally generated by the STAR system. Upon seeing the noisy image, two types of noise were predicted: that induced by shared ground planes and that generated by the microcontroller for Bluetooth communication. Due to imaging time constraints and cost, further discussion was not had whilst imaging, just in the lab. I believe that multichannel STAR is impressive on its own due to adding new features, however, taking time to fix flaws is vital. Designing multichannel STAR to mitigate noise is arguably more important than multichannel capabilities themselves. Two methods of mitigation were thus introduced: decoupling digital circuits from their RF and analog acquaintances and shielding sensitive RF transmission lines from wireless radio signals.

Finally, the lack of tissue signal intensity is important to qualify as well. The first thing to consider is the amount of input power into the STAR system and consequently into the transmit coil. Unfortunately for us, the power amplifier used for imaging was new in the console and never previously tested or qualified, so its performance was limited to the data sheet provided by the manufacturer. Perhaps, the amplifier was not sustainably outputting the RF power we measured, the transmit noise figure was too high, or STAR could not handle the spurious emissions. Regardless, STAR should be able to

handle hundreds of milliwatts of input RF power for imaging, and in the future a low noise amplifier should bypass the power amplifier, instead.

The insertion loss that the NMR signal undergoes through the receive channel, including STAR, is paramount to defining image SNR, thus it was quantified for multichannel STAR.

4.5 Multichannel STAR

Up to this point, an assumption about the MRI console used for STAR imaging is that it contains a single transmit channel and a single receive channel. Many modern machines, however, contain multiple transmit channels and multiple receive channels. Multichannel is a common term used in both industry and research; unfortunately, it is at first also rather confusing and ambiguous. At first glance, multichannel could mean multiple individual coils, multiple coil systems, or multiple digitized signals being reconstructed into an image by the console. The latter is the most formal definition, which is now known as "parallel MRI."

Enabling multichannel STAR to be standalone means empowering the user to command the entire system, which then means all channels requiring isolation need to be manipulatable, therefore requiring more user buttons. This motivated the transition from a PCB user board to an Android app, which was initially tested with standalone STAR.

As previously mentioned, SNR was the most pertinent issue seen in the STAR images. The methods used to remove this noise are discussed here in detail, however, the MRI machine was decommissioned before imaging could be re-performed. Therefore, multichannel STAR was only tested on the bench and not used for imaging.

Modern MRI was revolutionized with the introduction of parallel MRI. Parallel MRI introduces multiple channels, that is, multiple RF coils and receive ports in the MRI console. This allows digitization and digital signal processing of many different signals from different locations on the patient together to reconstruct an image. The first demonstration of parallel MRI used two RF transceiver coils on opposite sides of a human head, thus they were assumed to be decoupled from each other and time duplexed to the console using a single channel. This allowed them to considered as independent signal sources, as shown on the left of figure 36 [62]. For comparison, a single channel equivalent using a hybrid coupler is shown on the right of figure 36. For the next decade, many articles and conference proceedings advanced the new field of parallel MRI, with an excellent summary published in 2012 by Deshmane, et al. [64].
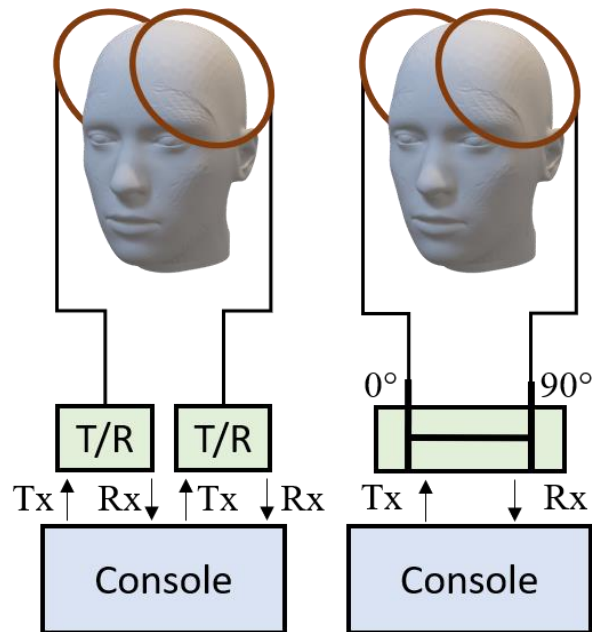
Figure. 36 Parallel imaging and multi-coil single channel

To enable multichannel STAR, a single birdcage transmit coil was used for optimal transmit B_1 field uniformity with multiple loop receive coils for maximum receiver sensitivity, as shown below in figures 37 and 38 [65]. This allows STAR isolation to be optimized individually between each loop coil and the single transmit coil, instead of operating as a transceiver where each coil would have to be isolated from every other coil.
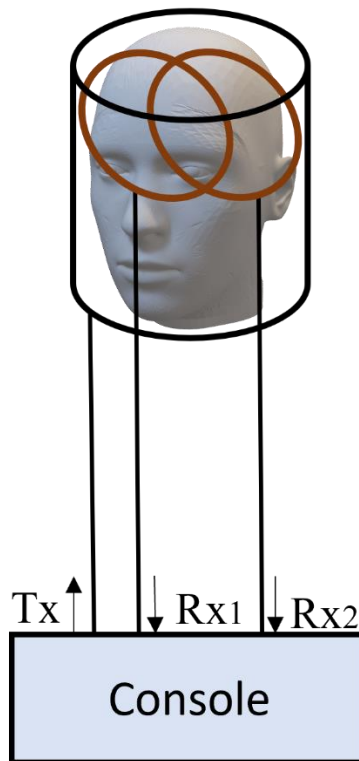
Figure. 37 Linear birdcage transmit coil with two linear loop receive coils
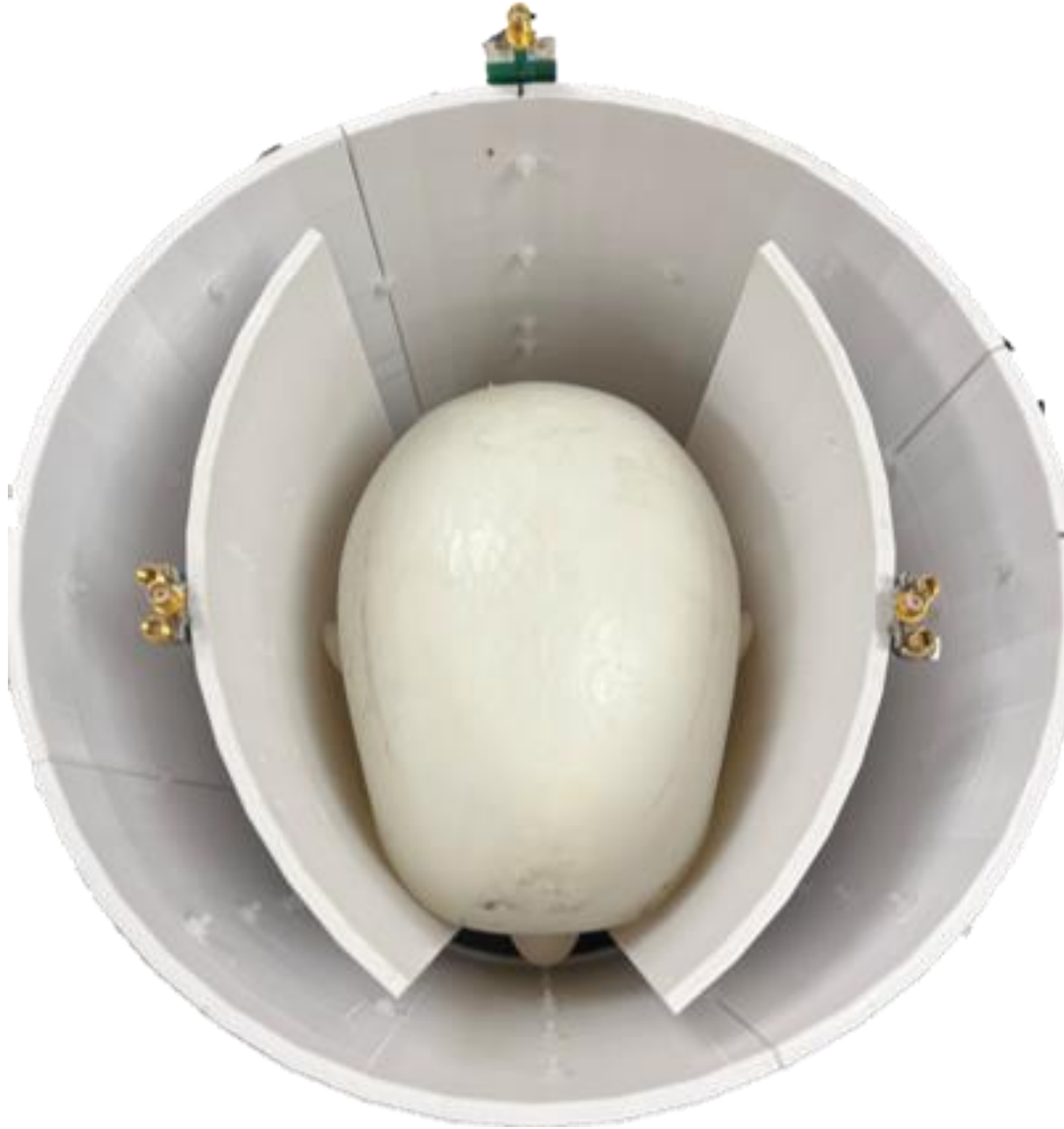
Figure. 38 PCB linear birdcage transmit coil with two PCB linear loop receive coils

4.5.3 Multichannel STAR Circuitry

To implement multichannel multiple hardware upgrades had to be made on the original standalone STAR system. Originally, all the modular circuits stacked together or just fit together nicely in a way that primarily benefited organization. Multichannel

STAR does the same, however, now the stacks more accurately reflect the upgradability of the system as a whole. Three high-level sections are now present. The first is the FPGA board, the second is the mutual stack, and the final section contains the receive stack. All boards that require power have linear voltage regulators on board.

The FPGA board is populated by the FPGA, the microcontroller, the DACs, and noise decoupling circuits. The mutual stack contains the power distribution board, the VCO board, the transmitter switching board, and the Wilkinson power divider that feeds the receive stacks. Finally, we arrive at the receive stack, which contains the cancellation channel, the Wilkinson power combiner, and the power detector board. This stack is especially important to consider for multichannel STAR because it can be duplicated for as many channels as are required for imaging.

Noise induced into RF signals is a fundamental problem in all RF circuits. For MRI, this directly translates to noise in the image, thus decreasing SNR and degrading image quality via poor contrast and artifacts. Digital electronics pose an enormous threat to RF signal integrity when sharing physical circuit space, such as mutual ground planes and coupling due to close-proximity transmission lines.

The first STAR system I published performed its cancellation algorithm excellently and worked well with the user-board, however, they needed further optimization to reduce noise. When previously imaging with the 1.5T system we saw an incredible amount of noise in the image while the microcontroller and FPGA were enabled, as shown previously. We also viewed a lot of noise on the MRI console from the wireless communication of the microcontroller. Fortunately, the ESP32 microcontroller natively contains five different sleep modes to shut down non-essential sections of the

controller, the DACs lock-in their current output voltage until told otherwise (via SPI), and the FPGA does not even need to be turned on at all for imaging. Even so, if any FPGA operations or wireless communication would like to be performed during future imaging, such as adaptive control of the cancellation channels, then it is essential to further decouple the digital devices from the RF systems as much as possible. The STAR system was upgraded in three primary ways to allow future multi-channel imaging to be as successful as possible.

First Optocouplers were introduced between the power detector and the ADC input of the FPGA. At first glance, we have the power detector feeding a signal to the optocoupler and then the optocoupler feeding a signal to the ADC. Unfortunately, it is not this simple. Optocouplers are current controlled current sources, whereas the power detector and the ADC require voltage signals. To integrate these devices together, a voltage controlled currented source is required, which is simply a MOSFET. However, the gate voltage range of this MOSFET must be controlled to correspond to a specific drain current range, therefore an opamp buffer must also be introduced in between the power detector and the MOSFET. The design method is discussed in detail in *4.5.3.9 Combined Signal Tapping and Power Detection*.

The next method to decrease noise was introducing digital isolators between the FPGA and the DACs. In recent years, digital isolators have begun to replace optocouplers for digital signals [66]. Digital isolators are finding a home in today's market as an alternative to optocouplers with comparable isolation, faster switching speeds, and less propagation delay. With devices like the Texas Instruments ISO676x series, which have six inputs and six outputs, it is also extremely easy to implement them with a system like

mine. Each isolator can handle two DACs-worth of signals at 50 MHz SPI operation (data, clock, and chip select), thus not limiting system speed. The only real concern for using digital isolators is the PCB layout and Texas Instruments published a guide on how to optimize your layout for multi-layer boards [67]. They do not require any external circuitry or buffering and can also act as logic shifters with the added bonus of galvanic isolation.

Finally, my circuits were upgraded to ensure RF signals propagating on grounded coplanar waveguides are via stitched into middle layers of the PCB as outlined in *2.5 Transmission Lines*. The board layer count was increased from two to four or eight, depending on the application. Boards requiring power planes, digital traces, or analog traces certainly used eight layers while purely RF boards used just four layers.

Before diving into the circuits that power multichannel STAR, a summary of the key components and integrated circuits used is tabulated below, followed by a photo of the STAR circuits integrated together on a 3D printed bed in figure 39. The largest board is the FPGA board, the bottom left stack is the mutual stack, and the receive stacks (one for each receive channel) are shown in the bottom center and bottom right.

Table. 4 Multichannel STAR key components

FPGA	DE0-Nano Development and Education Board
Microcontroller	ESP32 WROOM-32D
Digital to Analog Converter (DAC)	AD5761
Analog to Digital Converter (ADC)	ADC128S022 (on board FPGA)
Optocoupler	TCMT4106
Digital Isolator	ISO676xF
Voltage-Controlled Phase Shifter	JSPHS-51+
Voltage-Controlled Attenuator	RVA-3000+
Low Noise Amplifier (LNA)	PHA-13LN+
Power Detector	AD8310
RF Switch	HSWA2-30DR+
Coupler	ADCB-82+
Linear Voltage Regulators	ADM7150, ADP7104, ADR4525, LM78L12
Operational Amplifier	MAX44246
MOSFET	ZVN3320F
Voltage-Controlled Oscillator (VCO)	CVCO55CL-0060-0110
Wilkinson Power Divider	ADP-2-1W+
Digital NOT	SN74LVC2G04DBVR
Digital OR	74AHCT1G32DBVRG4

A block diagram of the multichannel STAR system can be seen in figure 40. It uses the fundamental building blocks that standalone STAR used, however, now there are more cancellation channels and receive coils, no hybrid coupler, added noise decoupling circuits, and the user board has been replaced with an Android tablet, shown in figure 41.
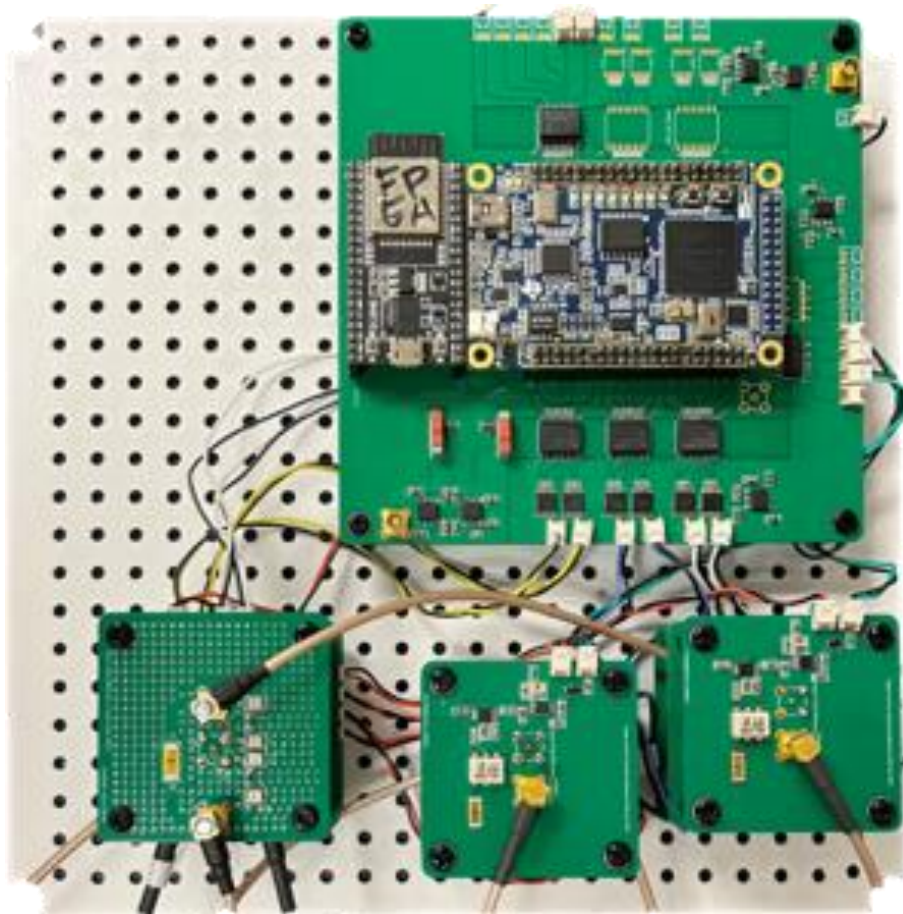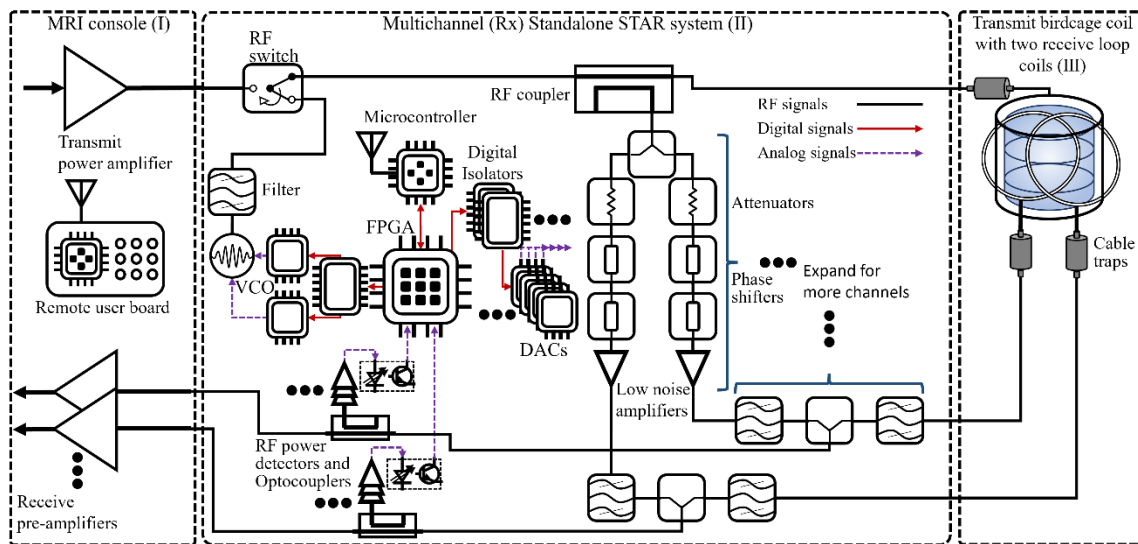
Figure. 39 All physical STAR circuits
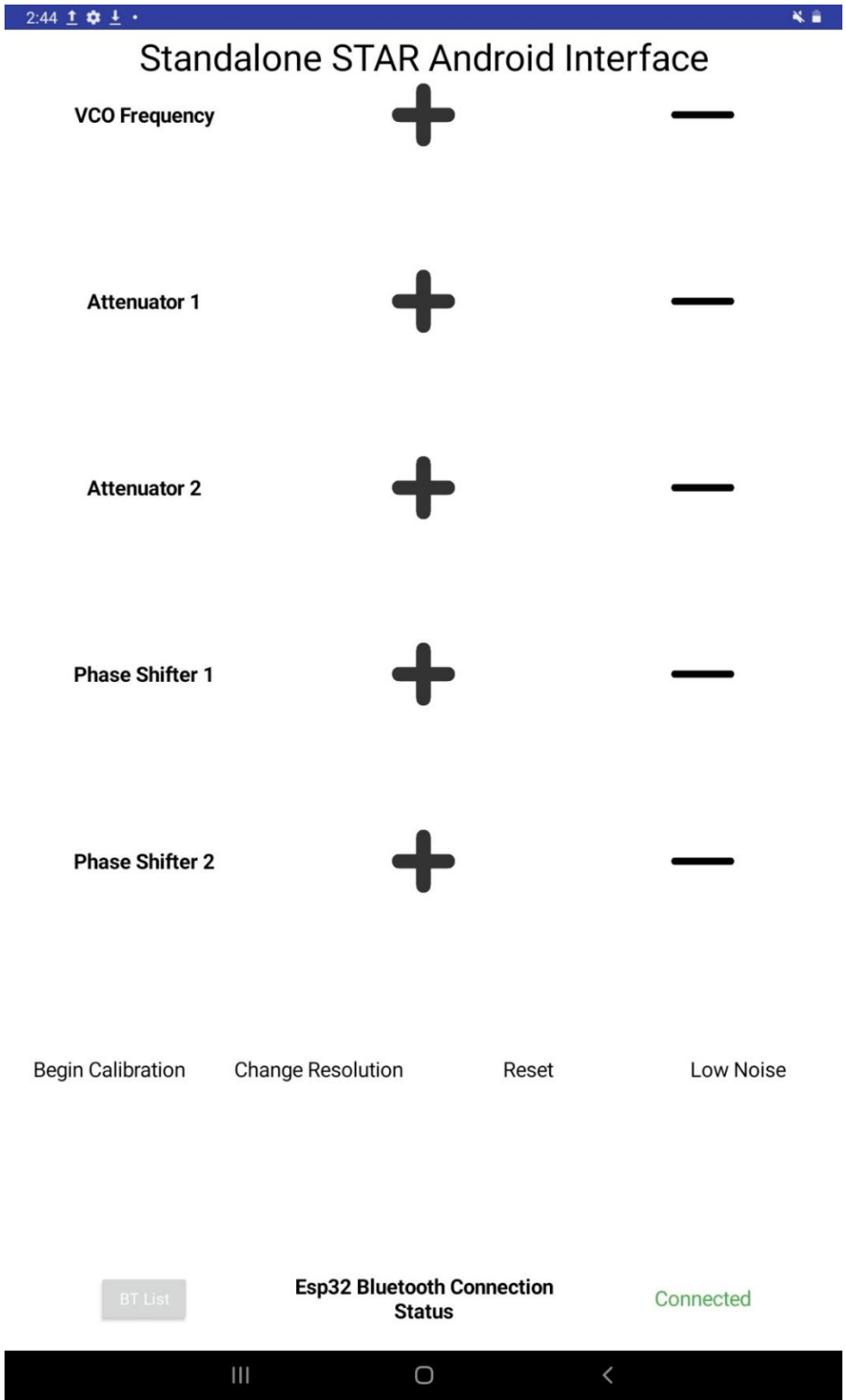

Figure. 40 Multichannel STAR block diagram

Figure. 41 Android application user interface for multichannel STAR

4.5.3.1 FPGA and Microcontroller

The brain of STAR is the FPGA with a microcontroller peripheral for user interaction. The FPGA communicates with the DACs using SPI for setting attenuator, phase shifter, and VCO control voltages, communicates with the RF switch for enabling the calibration signal path or the imaging signal path, digitizes the analog signal generated by the power detector with its onboard ADC for qualifying the leakage signal, iterates through $\sim2^{15}$ control voltage combinations for optimizing the cancellation signal, and receives commands from the microcontroller when user input is required.

All FPGA design and synthesis was done using Verilog in Quartus on a DE0 Nano Development board equipped with a Cyclone IV FPGA, shown in figure 42. The onboard reference clock operates at 50 MHz and sets the ceiling for data rates in conjunction with the DAC timing. The onboard ADC, however, only operates at up to 3.2 MHz, thus limiting the system speed drastically if every single control voltage transaction needs to be read. Slowing the system down to match the ADC maximum rate is optimal for now, however, the other hardware chosen and digital transmission line design practices implemented support up to 50 MHz to match the onboard reference clock.

The microcontroller used was the ESP32 WROOM 32D devkit C, shown in figure 43. The wireless communication capabilities via WiFi, Bluetooth, and ESP-now and the ease of programming it with the Arduino interface made it attractive for STAR.

The FPGA-microcontroller board is the most complicated in the entire system and its layout and PCBA can be seen in figures 44 and 45 along with the DACs, digital isolators, and optocouplers.
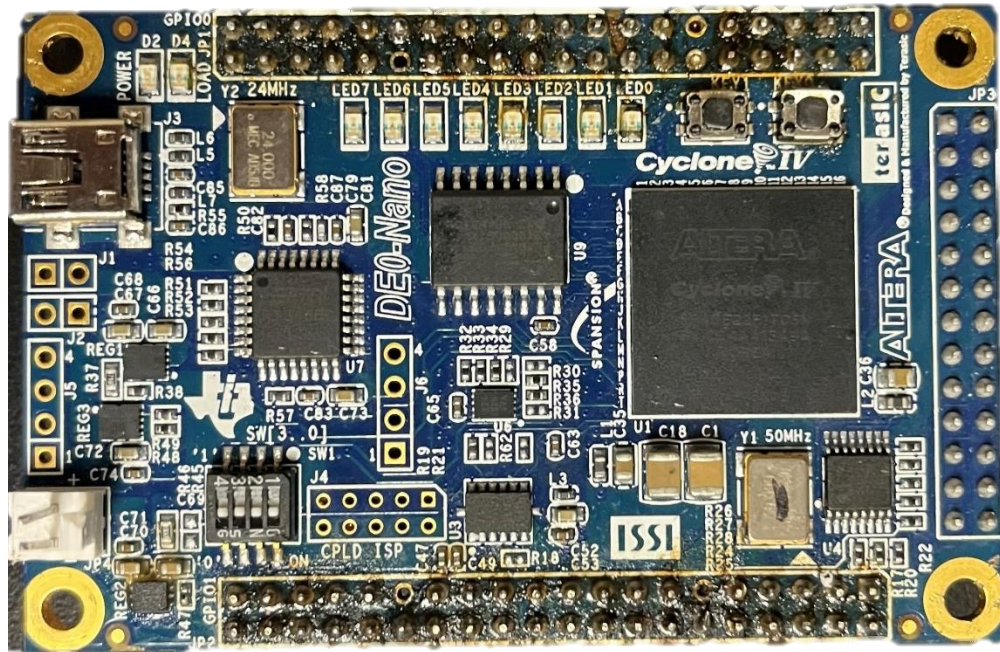
75

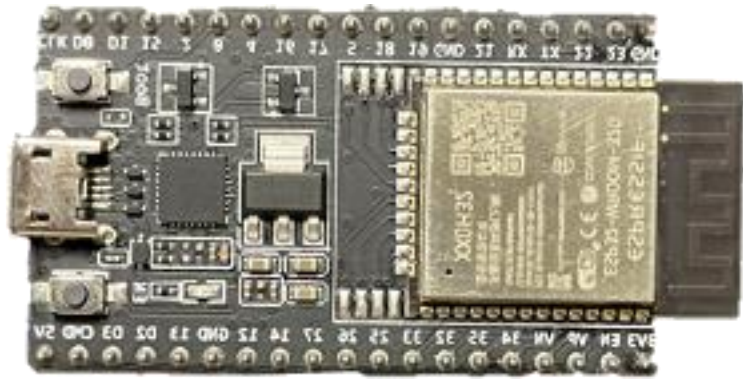Figure. 42 DE0 nano development FPGA

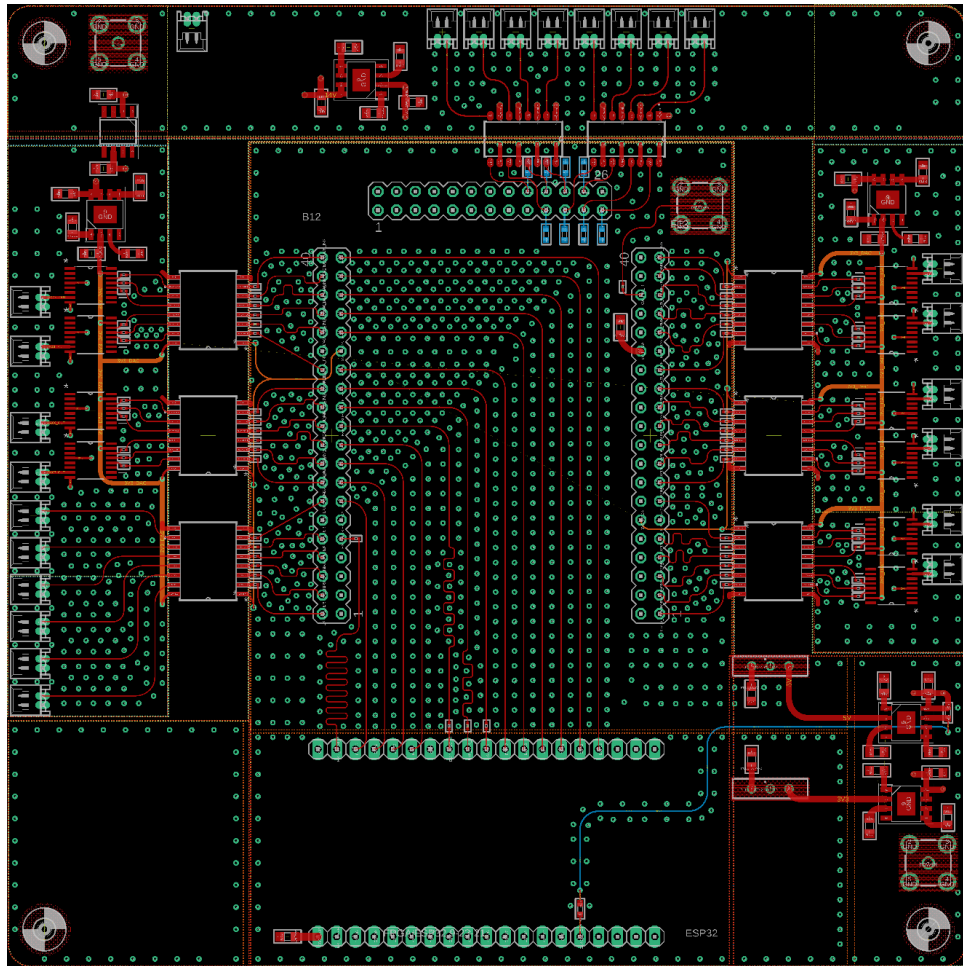Figure. 43 ESP32 WROOM 32D devkit C

Figure. 44 FPGA and microcontroller board layout
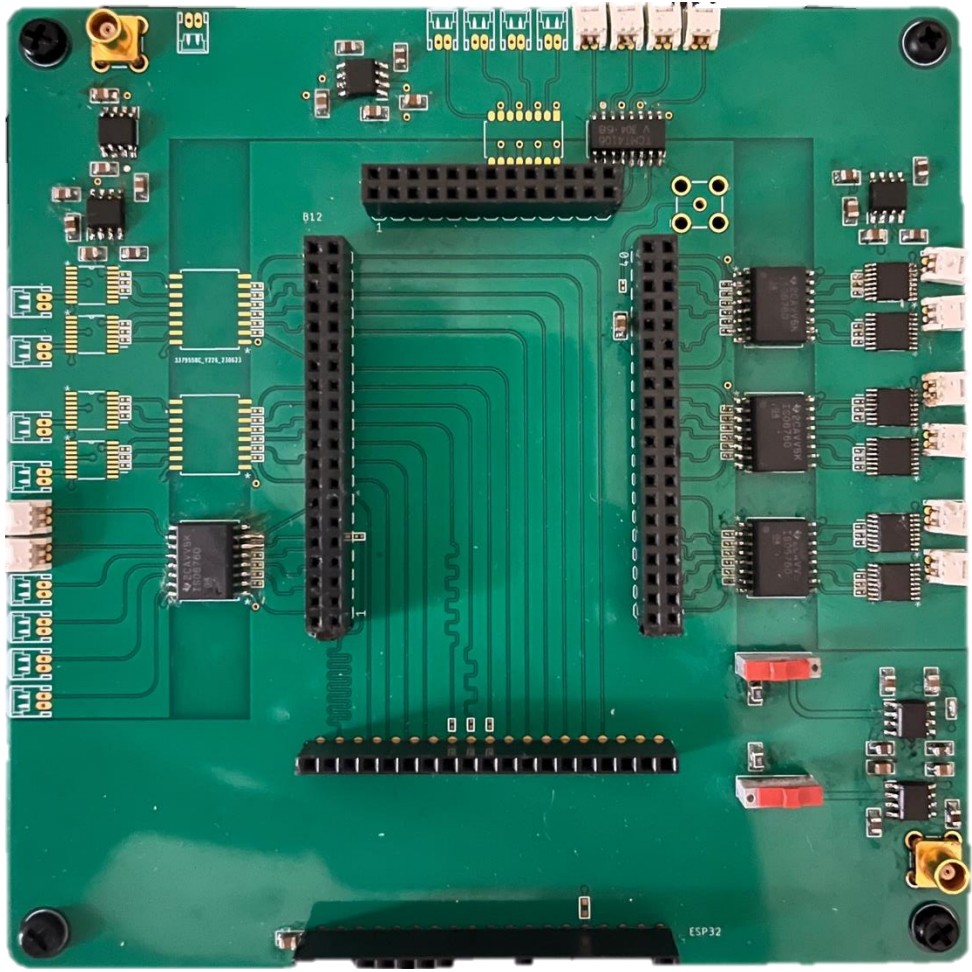
Figure. 45 FPGA and microcontroller PCBA

4.5.3.2 The Mutual Stack

The PCBAs presented hereafter have input and output ports symmetrically placed in the center of the boards. Since almost all boards in the system measure 5 cm by 5 cm, the input and output ports are placed such that boards can be rotated to accommodate whichever project requires them and to stack with one another using MCX ports and plastic spacers.

Figure 46 shows the mutual stack. From bottom to top we have the power board, the VCO board, the switching board, and a Wilkinson power divider. The power board does not output any signals to other boards in the stack via MCX; it is just simply convenient to place it here to save space in the system. The VCO board outputs one VCO signal via an MCX port for the switch and another for the user to read with an oscilloscope. Third in the stack is the switch board that outputs a signal to a power divider or coupler. One signal is intended for the transmit coil and the other for creating cancellation signals for the cancellation channels. The Wilkinson on top is used to take the single cancellation signal from the switch output and split it into two cancellation signals: one for each cancellation channel. An N-channel system would require and N-splitter here instead.

The next stacks are for the channels. Each channel stack contains a cancellation channel board, a Wilkinson power combiner, and a power detecting board. The inputs to the cancellation channel PCBs come from the Wilkinson power divider in the mutual stack, hence beginning our cancellation signal chain.
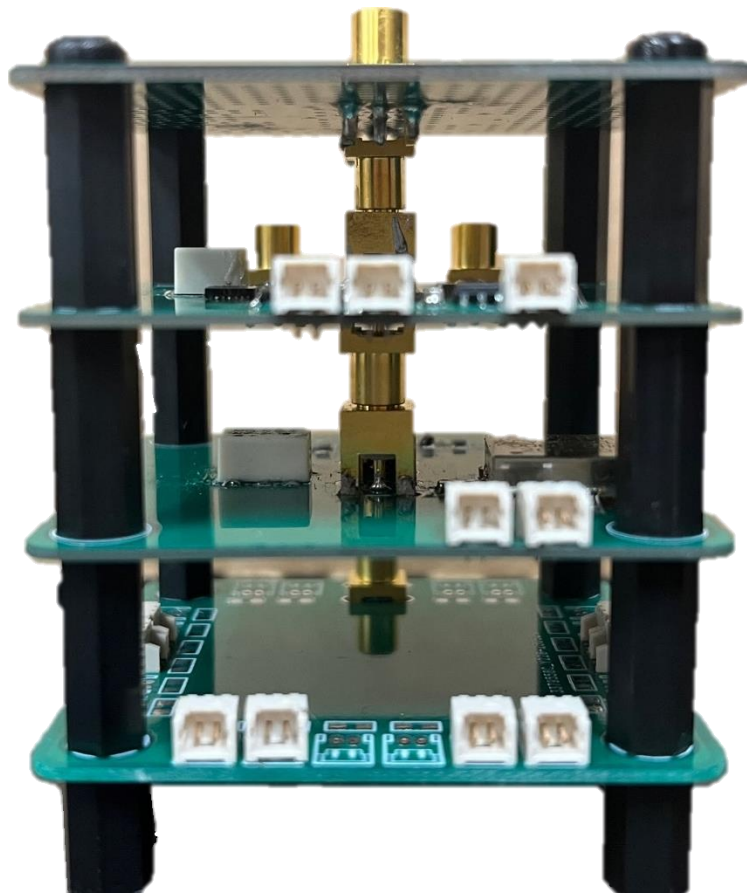
Figure. 46 The mutual stack

4.5.3.3 Power

Each board in STAR contains its own linear voltage regulators for managing power. This means that a single supply can be used for every circuit except the FPGA board, therefore requiring some form of power distribution. The phase shifters require 12 V for their operating range, thus assuming a 1 V headroom, a 13 V supply is required and every board must be able to handle this, except the FPGA board since it uses a different supply for noise decoupling. Fortunately, most circuits needing 13 V draw less than a few milliamps of current, thus the regulators do not need to burn up much power, even when dropping more than 10 V. The power distribution board is shown below. An MCX input accepts 13 V from a DC power supply and outputs 22 power lines through Molex picoblade connectors for other boards. This is certainly overkill for two channel STAR, but the PCB had ample space. Each output has room for a power network distribution smoothing capacitor too if the capacitors on the other boards do not seem to be enough. Figure 47 shows the circuit layout and physical PCBA.
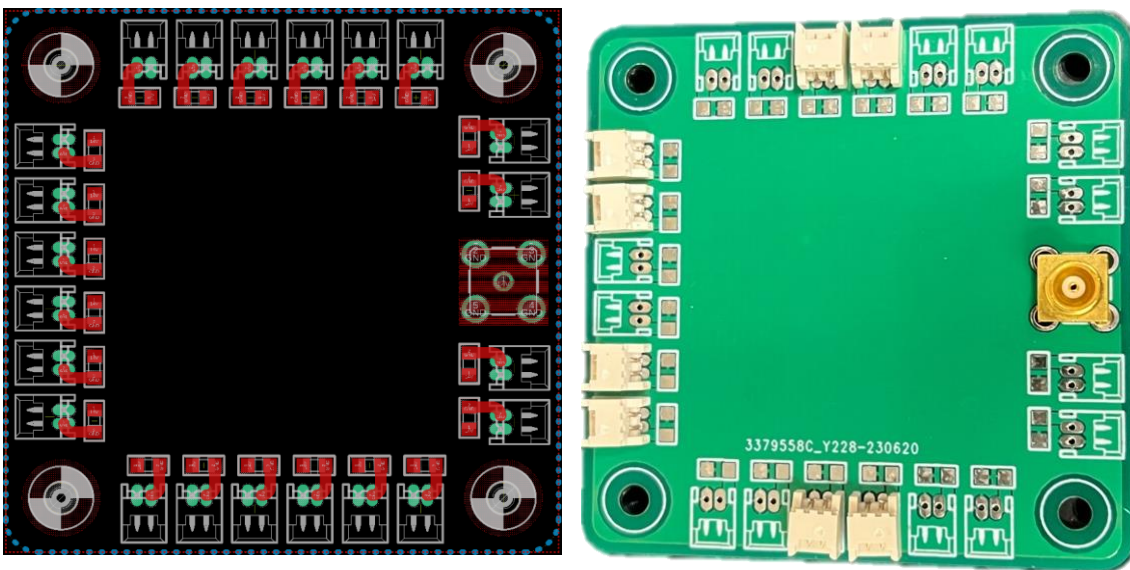
Figure. 47 Power distribution board layout and PCBA

4.5.3.4 VCO

The VCO is necessary to consider STAR as standalone because it is used to generate our calibration signal without any input from the console. Usually, VCO requirements must consider frequency tuning range, tuning resolution, phase noise, settling time, DC input power, and RF output power, and more; however, for STAR, all we really care about is the input current draw and RF output power. It's also nice to understand the tuning range for a more intuitive userboard control. As long as the input current is less than 25 mA then we can supply the VCO power with a DAC, thus readily controlling the VCO entirely using the FPGA and SPI signals, then any VCO is likely a fair choice The stronger the RF output power, then the better the isolation the can be found by STAR, which ultimately ends up being limited by the amount of power available at the power detector input. The VCO outputs two signals; one for calibration and one for optional user viewing, hence a power divider was used to split the output post-filtering. The relevant VCO board parameters are found in table 5.

Table. 5 VCO characteristics

Parameter	Measurement
Output power	-4.2 dBm
Tuning range increment	8 MHz/V
Current (power) draw	15 mA (75 mW)

A 3rd order Butterworth bandpass filter topology was chosen and designed in Elsie to filter the VCO output, as seen in the ADS schematic in figure 48 with tabulated component values for 64 MHz in table 6.

82
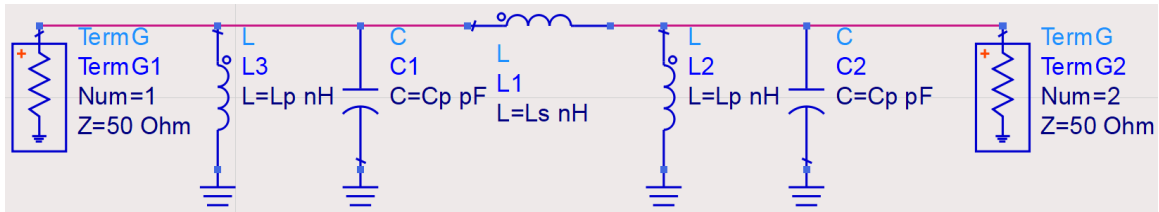
Figure. 48 Schematic of VCO filter

Table. 6 VCO filter component values

Component	Values	
	Ideal	Real
L_p (nH)	12.0558	12
C_p (pF)	562.569	560
L_s (nH)	124.34	120

The filter was simulated in ADS and the results for insertion loss and return loss are also shown in figure 49. The x-axes represent frequency from 50 MHz to 80 MHz and the y-axes represent return loss from 0 dB to 40 dB and insertion loss from 0 dB to 20 dB. We can see that the insertion loss is minimal (< 1 dB) and the return loss es excellent (> 30 dB). Figure 50 shows the circuit layout and PCBA.
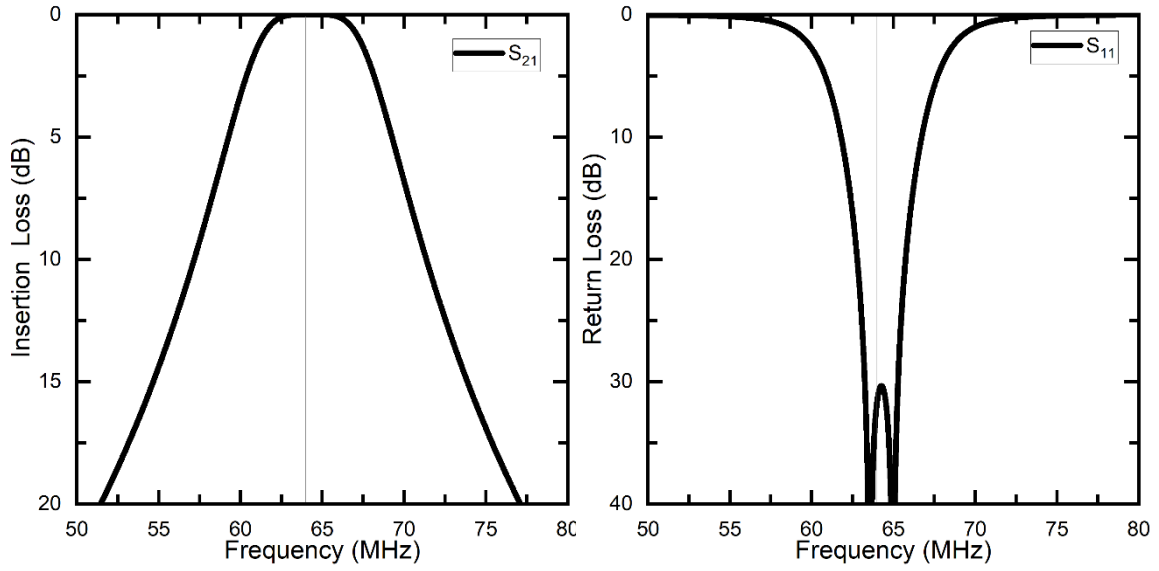
Figure. 49 VCO filter insertion loss and return loss
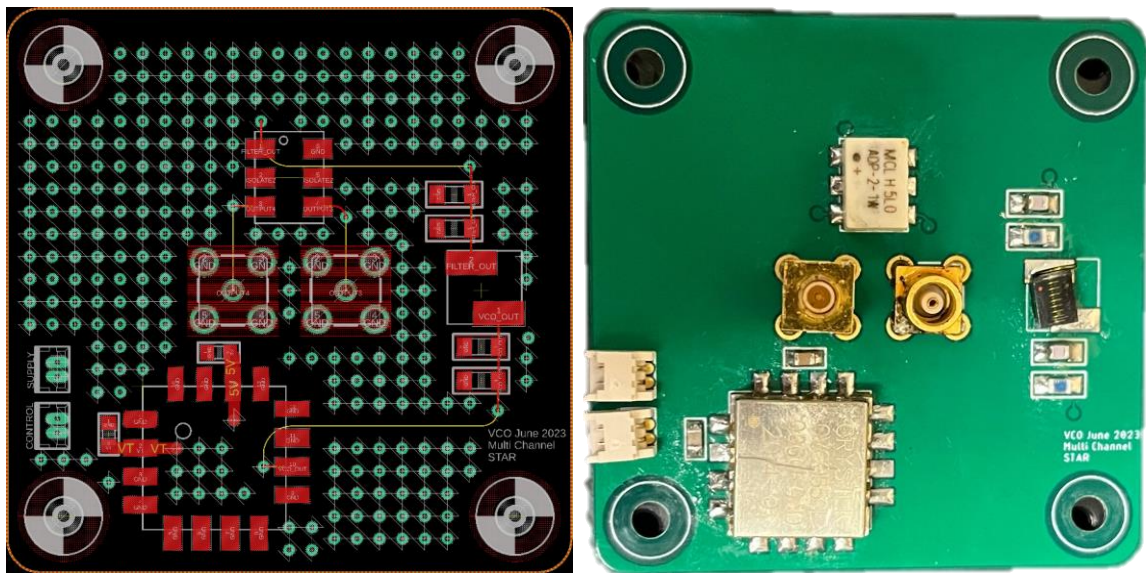
Figure. 50 VCO circuit layout and PCBA

The RF switch requires two control signals to be used to enable/disable two RF pathways. The default mode of operation of the switching circuitry was designed to propagate the console signal, thus only propagating the VCO signal when explicitly told by the FPGA during calibration.

The switching and splitting circuit requires buffering to maintain the default operation and to operate during imaging if the user would like to completely turn off the FPGA. "Buffered Control 1" thus pertains to the console signal and "Buffered Control 2" pertains to the VCO calibration signal. This buffering is simple to implement with a few digital logic gates that map to the following truth table and two circuit choices:

Table. 7 Mapping input control signals to buffered control signals

Input Control 1	Input Control 2	Buffered Control 1	Buffered Control 2
0	0	1	0
0	1	0	1
1	0	1	0
1	1	1	0
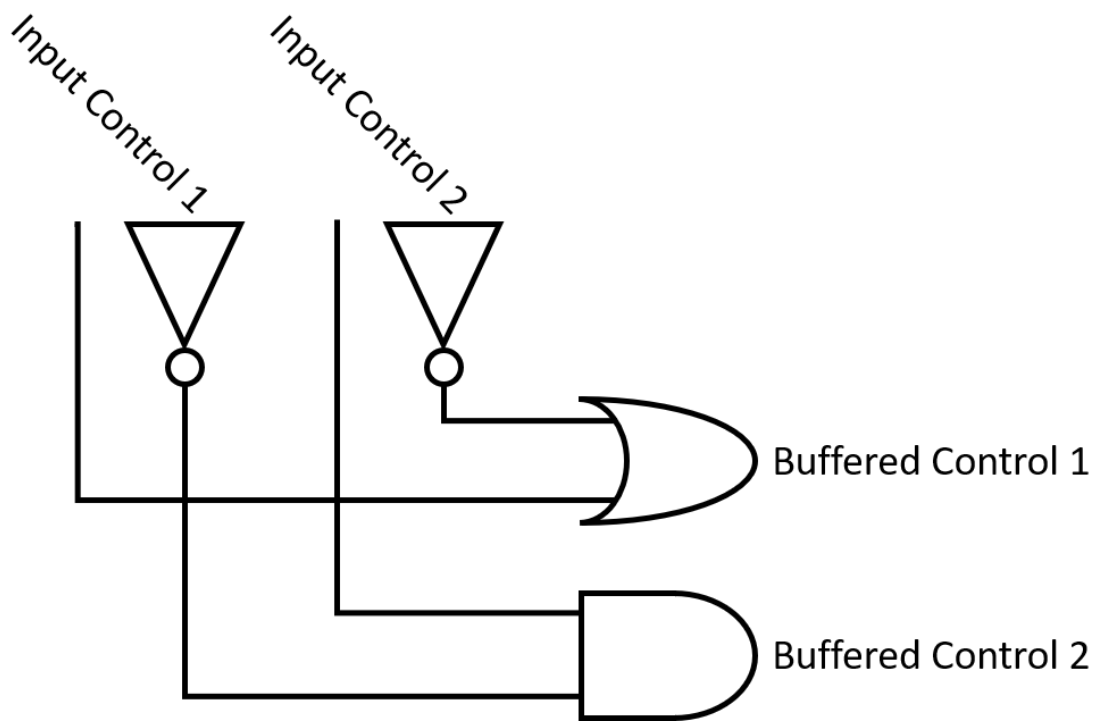
Figure. 51 RF switch buffering circuit option 1
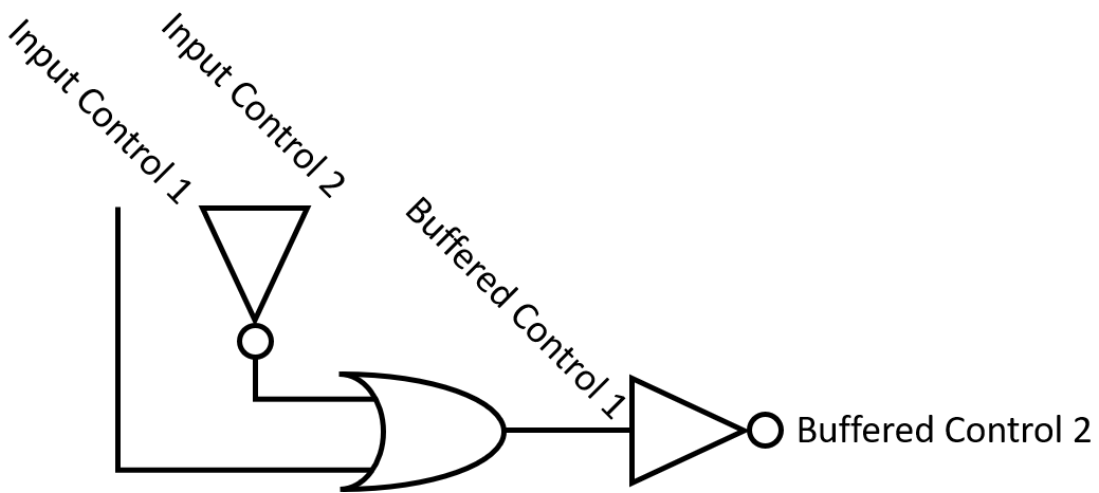
Figure. 52 RF switch buffering circuit option 2

Figure 51 shows a more stable system, however, figure 52 shows a more conveniently built system, provided the console signal is not enabled immediately following the VCO being disabled. This is a fair presumption for STAR, thus the buffering circuitry in figure 52 was chosen.

The switch & split board contains four RF ports: 1. the console input for the pulse sequence during imaging, 2. the VCO input for calibration, 3. the transmit coil for both imaging and calibration, and finally 4. the cancellation channels. The RF ports of the board were characterized using scattering parameters and shown in figures 53, 54, and 55 for both switch states, where the x-axes represent frequency from 50 to 80 MHz and the y-axes represent return loss, insertion loss, and isolation in dB.
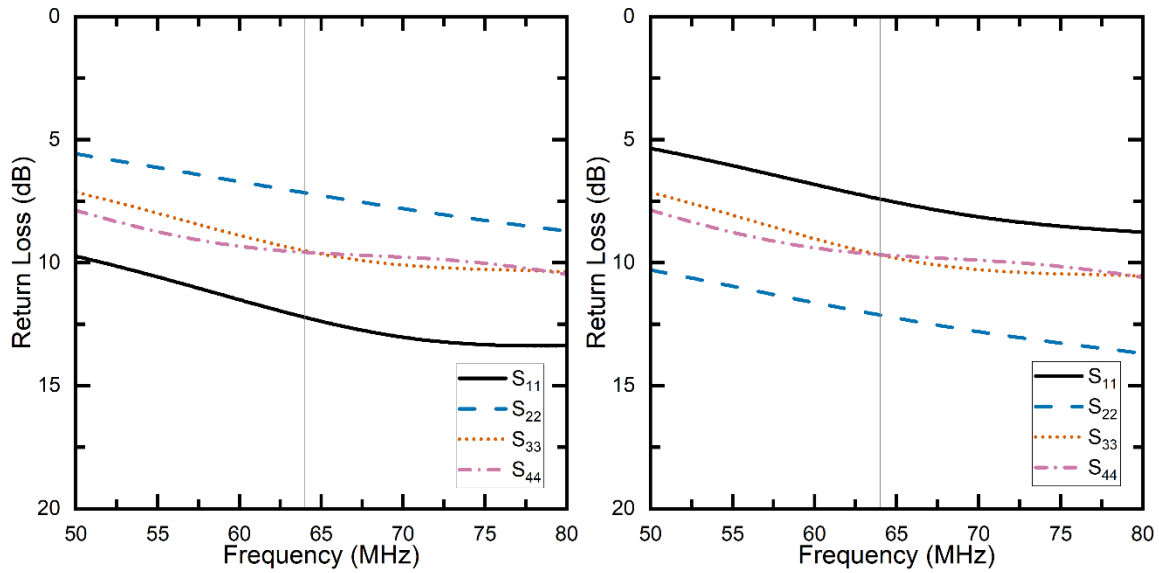
Figure. 53 Switching circuit return loss of all ports for both switch states
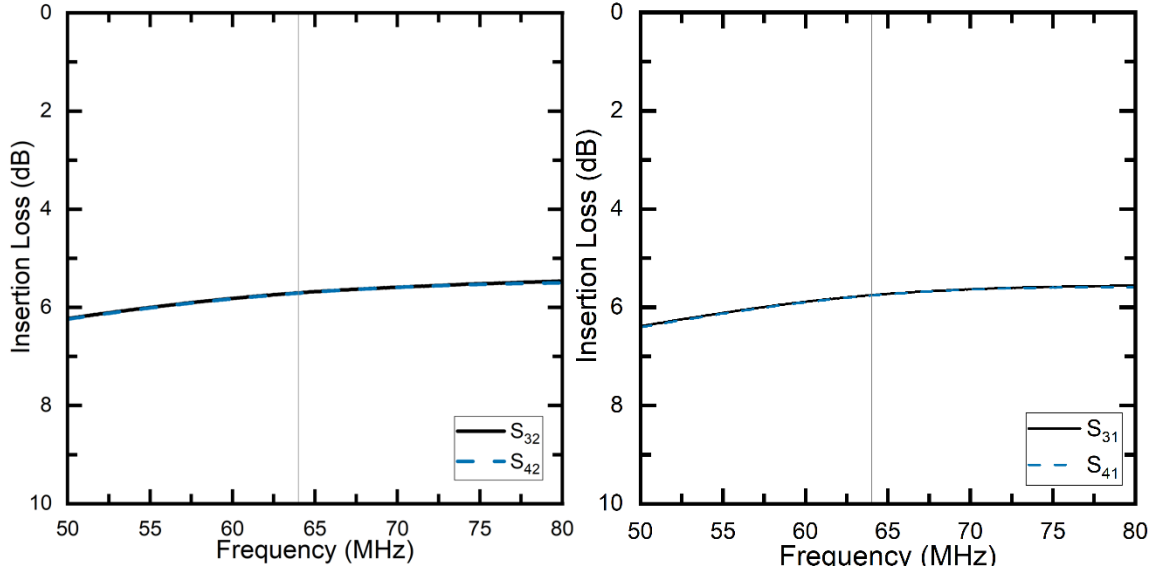
Figure. 54 Switching circuit insertion loss of transmit paths for both switch states
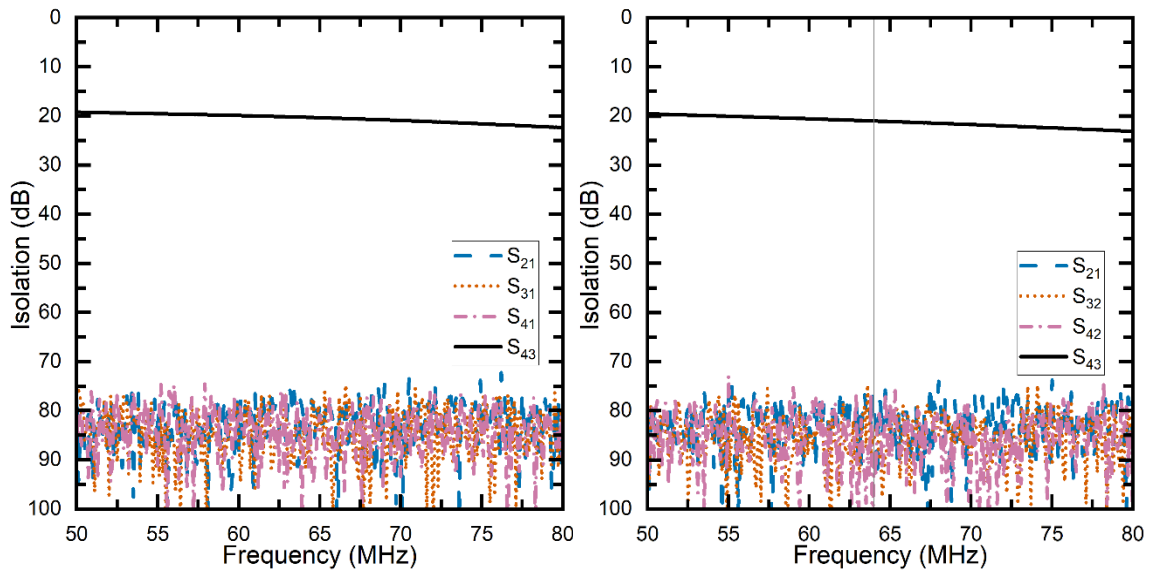
Figure. 55 Switching circuit isolation for both switch states

In theory, any coupling factor can be chosen for the coupler or power divider used to generate the cancellation signal. Two versions were created for the current multichannel STAR system: one using a 3 dB coupling factor and one with a 20 dB coupling factor. The layout for both is shown in figure 56, however, only the 3 dB coupling system was built and used, whose physical board is also shown. The coupler chosen presents a tradeoff between imaging power available and the amount of receive channels that multichannel STAR can support. An equal split enables more receive channels to be used, but reduces imaging power available, thus a 20 dB coupler would be favorable for only two channels.

The insertion loss was a bit higher than expected (> 6 dB) and the return loss a bit lower than expected (< 15 dB). This is likely due forcing RF signal through poorly designed vias. In the future, the via modeling should be taken more seriously as a vital component in the signal path.
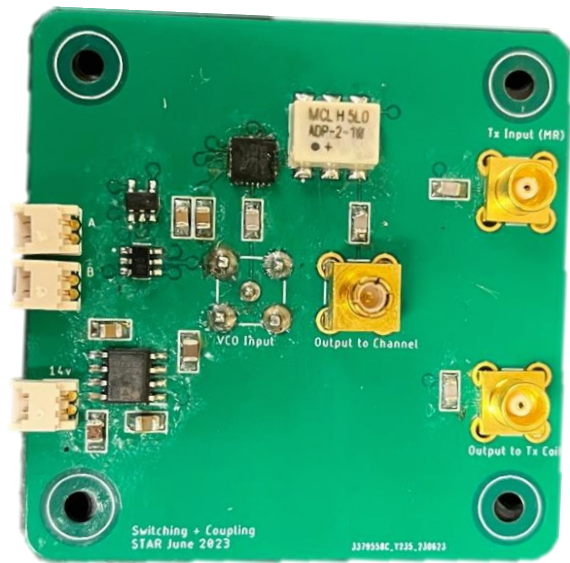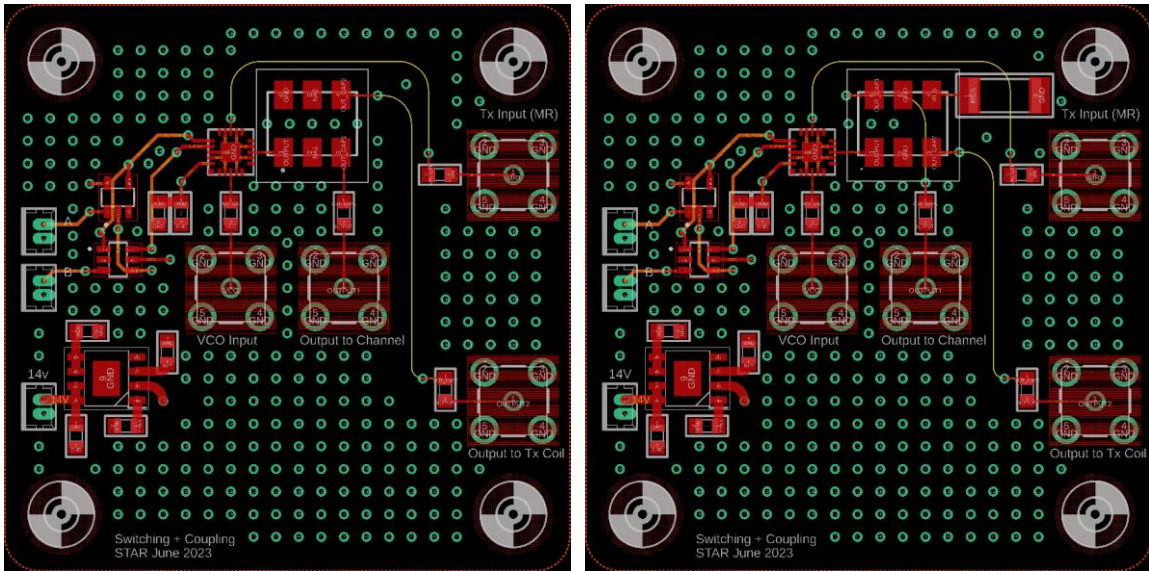
Figure. 56 Circuit layout and PCBA for switching board

4.5.3.6 Wilkinson Power Dividers

The Wilkinson power dividers are used for two purposes in two channel STAR. The first is to split our cancellation signal into two separate cancellation signals for the cancellation channels, hence one for each receive channel. The second is to combine the receive signals with the cancellation signals, therefore enforcing destructive interference. This means three total Wilkinson PCBs are required for two channel STAR. If four channels are requested, then a four-way split Wilkinson would be required for feeding the cancellation channels and four standard Wilkinsons would be required for combining signals, thus a four-way split board was also made in case STAR would like to be upgraded to four channels. Beyond four channels, more hardware would have to be developed.

Since Wilkinsons require 90° length transmission lines, they are nominally too large for the wavelengths used in MRI. Thus, the transmission lines must be converted to lumped element equivalents. A shunt capacitor, followed by a series inductor, and another shunt capacitor works well over a narrow bandwidth, as previously shown in *3.3.3 Hybrid Couplers vs Power Combiners for RF Coils*. Once solved, the reduced-size Wilkinson can be designed and. The layout and a photo of the physical PCBA are shown in figure 57.
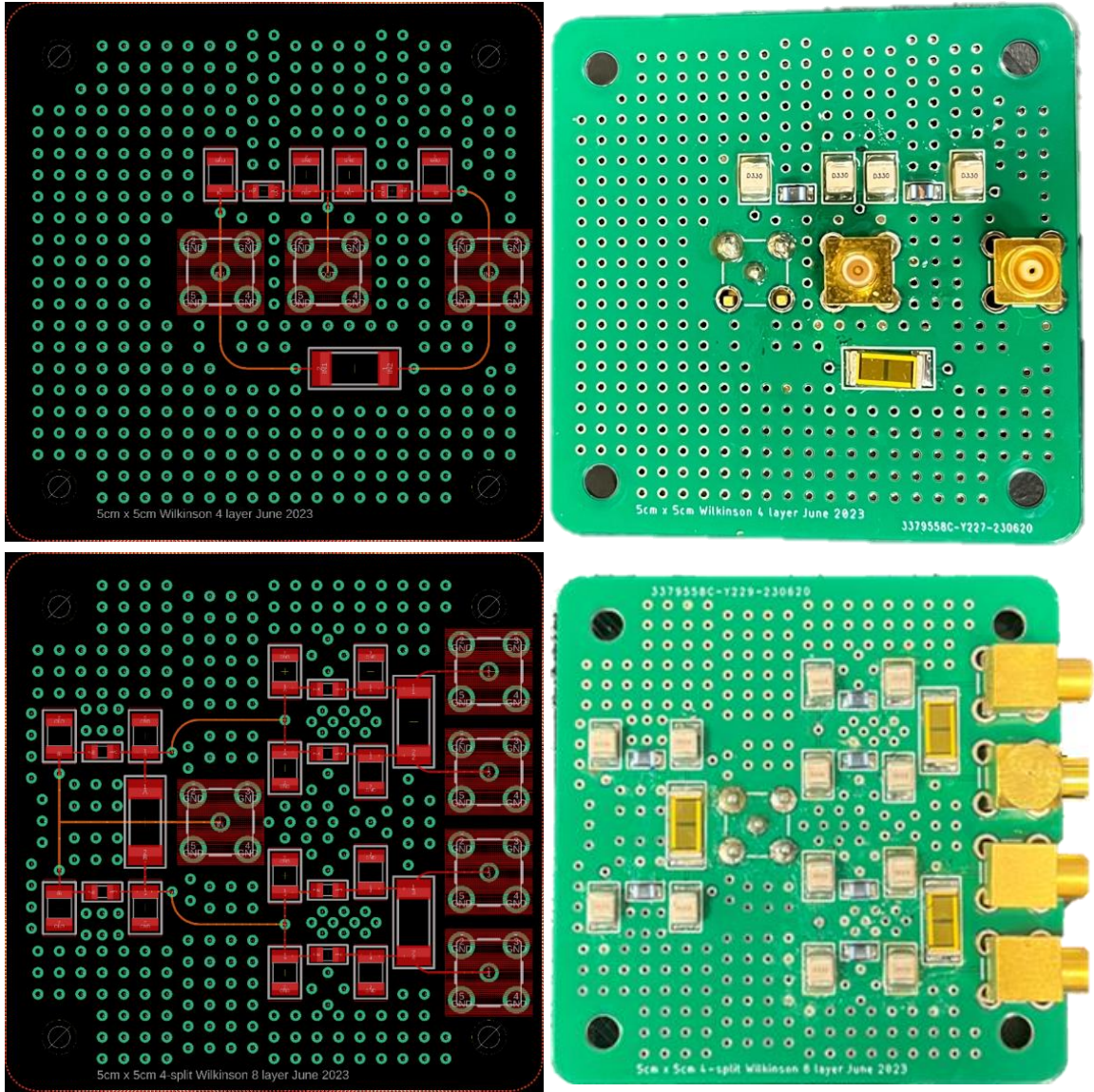
Figure. 57 Circuit layout and PCBA for Wilkinson power combiners

The return loss and insertion loss plots are shown below in figure 58 for the standard Wilkinson. The x-axes are frequency from 50 MHz to 80 MHz and the y-axes are insertion loss, isolation, and return loss from 0 dB to 40 dB. The insertion loss of the circuit is minimal, the isolation is excellent, and the return loss, thus matching, is also excellent over the narrow bandwidth, hence acting as a pass-band filter as well.
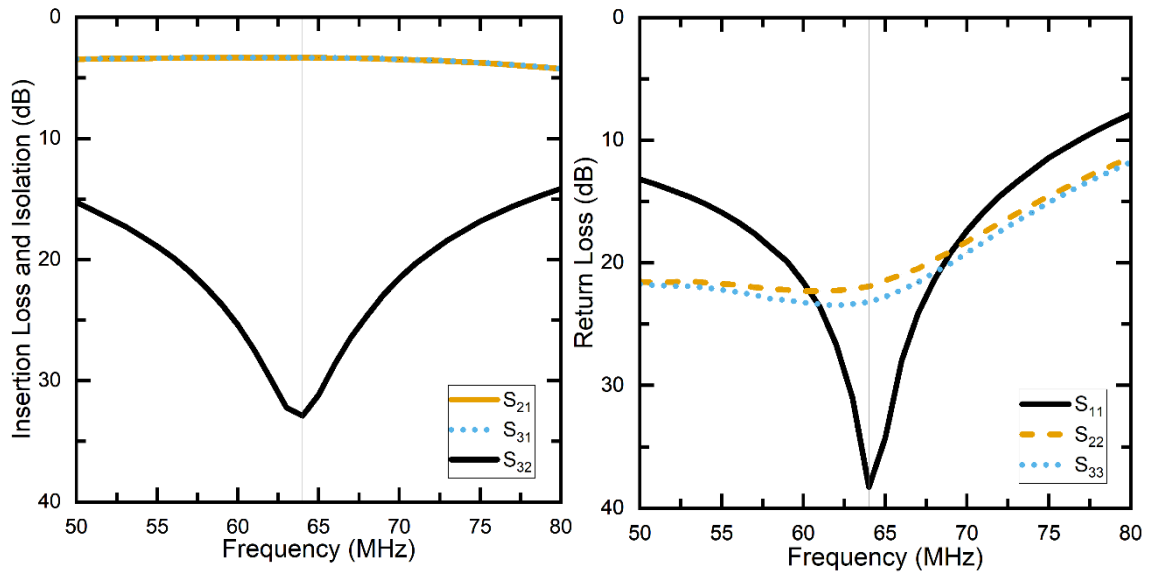
Figure. 58 Wilkinson power combiner insertion loss, return loss, and isolation

The two new boards introduced for the channel stack were the cancellation channel and the power detector board. Also included is the Wilkinson power combiner, however, that was discussed in the mutual stack. The modularity of multichannel STAR truly shines with the channel stack. If more channels are required for imaging, then simply build another channel stack and interface it with the FPGA board using control voltage lines and the mutual stack using MCX coaxial cables. Figure 59 shows the two channel stacks used for multichannel STAR where the cancellation channel is on bottom, thus feeding into the Wilkinson power divider, which outputs the combined cancellation and leakage signal to the power detection circuit.
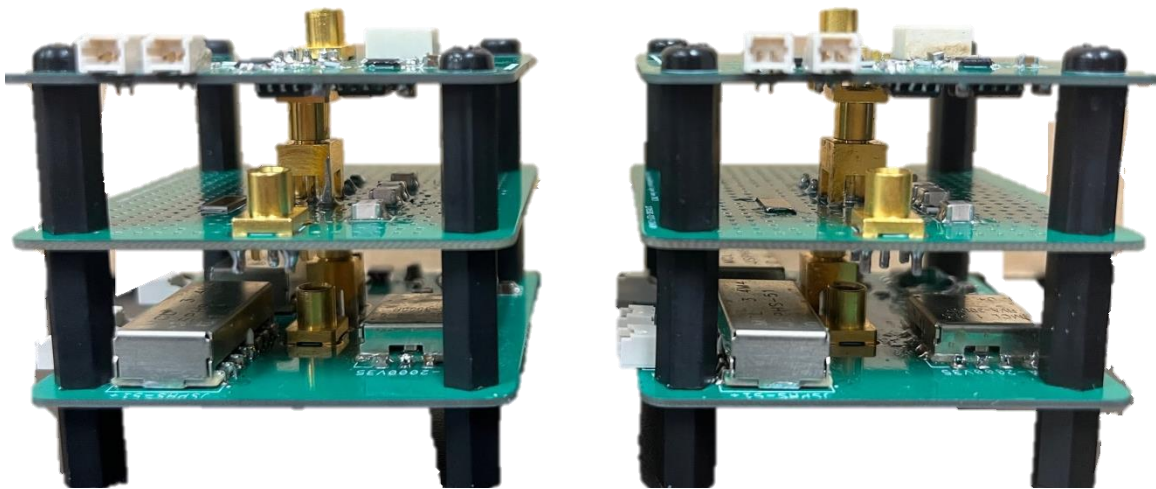
Figure. 59 Two receive channel stacks for two channel STAR

A separate cancellation channel is required for each receive channel, thus receive coil. Each channel contains two voltage-controlled phase shifters in series that share a single control voltage, one voltage-controlled attenuator, and an LNA with its associated biasing and matching circuitry, shown in figure 60.
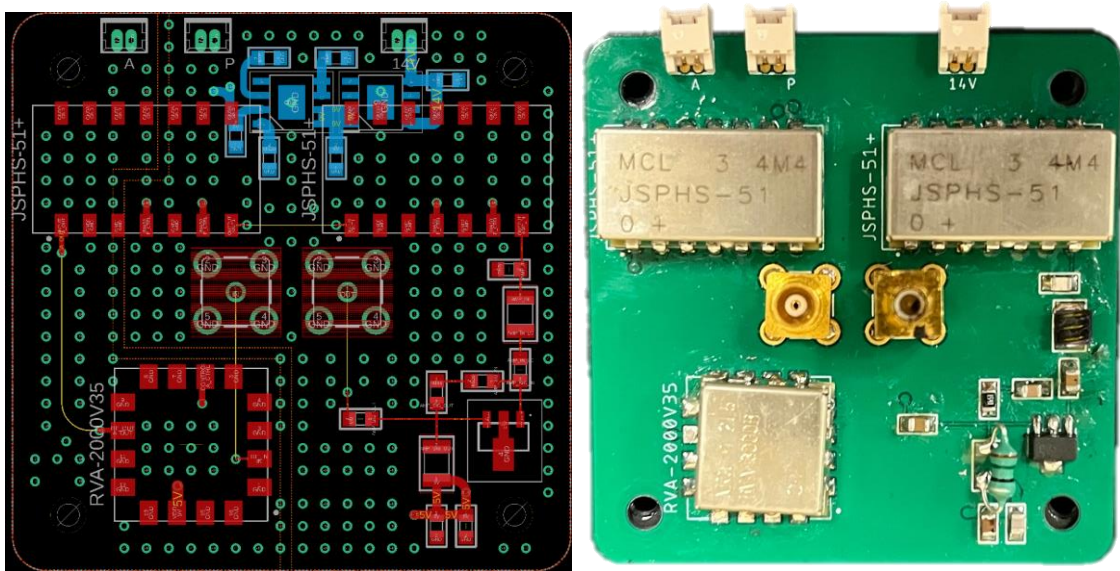
Figure. 60 Circuit layout and PCBA for cancellation channel

Characterizing the cancellation channel primarily involves showing that a full 360° phase match can be made over a range of control voltages. Of course, also required is a demonstration of the amplitude matching able to be provided. The LNA is intended to guarantee that amplitude matching is guaranteed with high isolation between cancellation channels for this original implementation of multichannel STAR. If we represent the coupling factor of the coupler used to split the signal between the

cancellation channels and the coils as C dB, the insertion loss of the coupler as IL dB, the number of channels as N, the minimum attenuation of the attenuator as α_{min} dB, the maximum insertion loss the phase shifter as θ_{IL} dB, the gain of the LNA as G_{LNA} dB, the insertion loss of the cable traps as CT dB, and the geometric isolation of the transmit coil to the receive coil as ISO dB, then to fully cancel the leakage signal, the losses of the cancellation channels must be lower than the losses of the leakage signal. This is represented by equation 23.

$$C + 3\log_2 N + \alpha_{min} + \theta_{IL} - G_{LNA} < IL + 2CT + ISO$$

Equation. 23 Loss of cancellation channel vs loss seen by leakage signal

If one would like to explicitly solve for the amount of channels STAR can support with chosen circuit and coil parameters, then solving for $3\log_2 N$ results in equation 24.

$$3\log_2 N < IL + 2CT + ISO - C - \alpha_{min} - \theta_{IL} + G_{LNA}$$

Equation. 24 Determining how many channels STAR can support

This makes characterizing how STAR can be extended for future multichannel endeavors quite simple, however, a couple apparently beneficial design choices should not be made. The insertion loss of the coupler and the cable traps should not be artificially increased for the sake of cancellation; this reduces imaging power and increases imaging noise. Beneficial design choices include decreasing phase shifter insertion loss, decreasing the minimum attenuation of the attenuator, and increasing

amplifier gain. Also of important discussion is the intrinsic geometric decoupling of the coil system. STAR is complimentary to intrinsically well-isolated coils. For simple multichannel systems, geometric decoupling can be nearly forgotten since STAR can have plenty of RF power available for cancellation, however, as channel count increases or hardware changes are made, the entire imaging ecosystem needs to be reevaluated. For example, if a system has been designed to send maximum transmit power to poorly isolated coils with a highly directive coupler, then using reasonable values IL = 0.2 dB, C = 20 dB, CT = 1 dB, ISO = 5 dB, α_{min} = 3 dB, θ_{IL} = 3 dB, and G_{LNA} = 22 dB, the maximum number of support channels is two. If the coils are repositioned such that their geometric isolation increases from 5 dB to 10 dB, then six channels are supported. The current STAR system uses a Wilkinson power divider instead of a coupler for sending a strong signal to the cancellation channels for the sake of characterization. In a real imaging system, this would be less appropriate since it reduces the amount of power available for actual imaging.

The cancellation channel was coarsely characterized to demonstrate the 360° phase range and the ability for the channel to attenuate or provide gain to the cancellation signal.

The first solid black plot represents the attenuator tuned to 2 V and the phase shifters swept from 0 V to 12 V in 0.5 V increments, the second dashed blue plot represents the attenuator tuned to 3 V and the phase shifters swept from 0 V to 12 V, and the third dotted orange plot represents the attenuator tuned to 4 V and the phase shifters swept from 0 V to 12 V. For the 2 V attenuator plot, the input return loss was always more than 14 dB, the output return loss was always more than 14 dB, the gain was up to -11.4 dB, and the isolation was 60 dB. For the 3 V attenuator plot, the input return loss was always more than 23 dB, the output return loss was always more than 15 dB, the gain was up to 7.5 dB, and the isolation was 42 dB. For the 4 V attenuator plot, the input return loss was always more than 17 dB, the output return loss was always more than 14 dB, the gain was up to 10.3 dB, and the isolation was 40 dB.
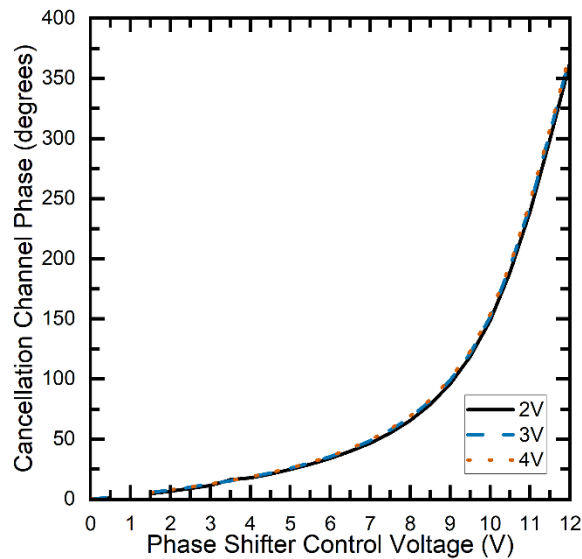
Figure. 61 Phase shifter control voltage vs phase range within the cancellation channel

As figure 61 shows, it does not matter what the contribution to the total phase the attenuator has with various control voltages. As long as the phase shifters can shift the entire unit circle, then the cancellation channel can force the cancellation signal to match the leakage signal phase.

4.5.3.9 Combined Signal Tapping and Power Detection

Optocouplers are an industry standard for galvanic isolation between circuits. Although they are slowly being phased out in digital applications by digital isolators, a handful of signals in STAR are analog, thus both were used in conjunction. Optocouplers were used to map the power detector output to the ADC input with entirely separated current paths. LTSPICE was used to simulate the driver and optocoupler system before doing a PCB layout using all the exact components and models, except for the optocoupler itself since their models are scarce; instead, a similar optocoupler native to LTSPICE was simulated. The schematic of the system is shown below in figure 62.
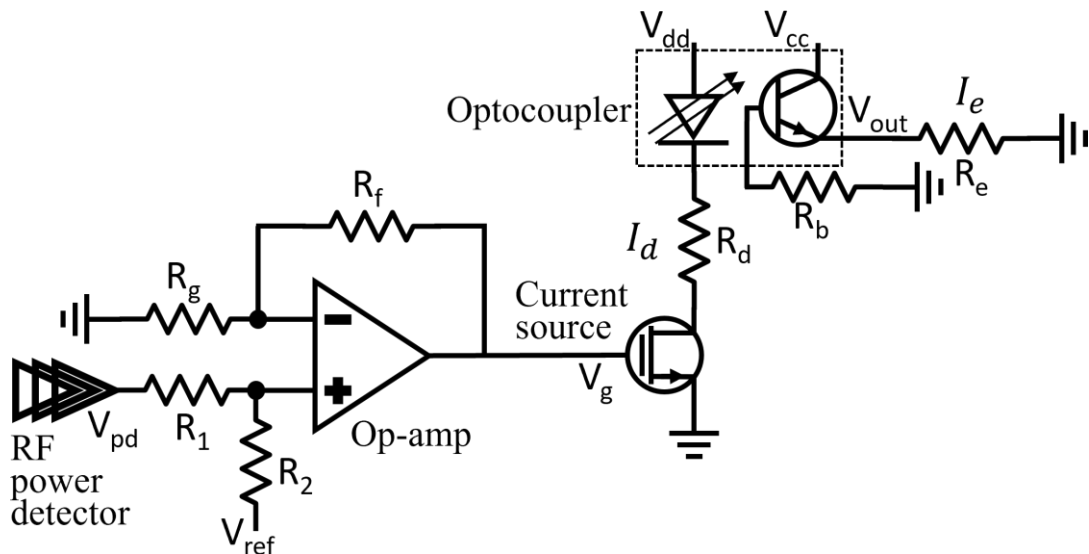
Figure. 62 Schematic of optocoupler and driver

The design methodology to find all the resistor values is as follows:

1. Choose an optocoupler BJT emitter current range (I_e) and emitter resistor (R_e) value that correspond to our preferred ADC voltage input range (V_{out}).

2. Determine the optocoupler LED current range (I_d) that corresponds to the optocoupler BJT emitter current range by using the optocoupler current transfer ratio.

3. Determine the MOSFET gate voltage range (V_g) that corresponds to the optocoupler LED current range, which equals the MOSFET drain current. This also likely requires a resistor (R_d) in series with the MOSFET channel, whose channel resistance in denoted as (R_0).

4. Design the op-amp feedback and biasing circuits (R_1, R_2, R_g, R_f) to map the power detector output voltage range into the MOSFET gate voltage range.

Each of these steps were individually approximated by hand and simulated in LTSPICE. LTSPICE was used to tune the values, which resulted in the following simulation data. The only problem with the simulations is that it is difficult to find optocoupler SPICE models published online. Because of this, a similar built-in optocoupler device was chosen just for simulation. The opamp and the transistor models were available, however, so the simulations were expected to reasonably approximate the physical design. The equations used to start the design process are as follows:

$$V_{out} = I_e R_e$$

$$I_e = \alpha I_d$$

$$I_d = \frac{V_{dd} - V_{LED}}{R_d + R_0}$$

$$V_g = V_{in} \left(\frac{R_2}{R_1 + R_2} \right) \left(\frac{R_F + R_G}{R_G} \right) + V_{ref} \left(\frac{R_1}{R_1 + R_2} \right) \left(\frac{R_F + R_G}{R_G} \right) = V_{in} m + b$$

$$V_{g1} = V_{in1} \cdot m + b$$

$$V_{g2} = V_{in2} \cdot m + b$$

Equation. 25 Design equations used for the optocoupler driver

The former three equations define your output voltage from a MOSFET gate voltage and the latter three equations map your power detector output voltage range to the MOSFET gate voltage range. Thus, it is important to understand your power detector range and to ensure the circuit does not overload anywhere if you happen to operate outside of that range.

The LTSPICE results are tabulated in table 8 and plotted in figure 63 where the x-axis is power detector output voltage from 0.3 V to 2.7 V on both plots. The BJT emitter and MOSFET drain currents are on top in pink and blue from 0 mA to 50 mA. The power detector output voltage, MOSFET gate voltage, MOSFET drain voltage, and ADC input voltage are shown in grey, blue, red, and green, respectively in the bottom plot from 0 V to 4 V.
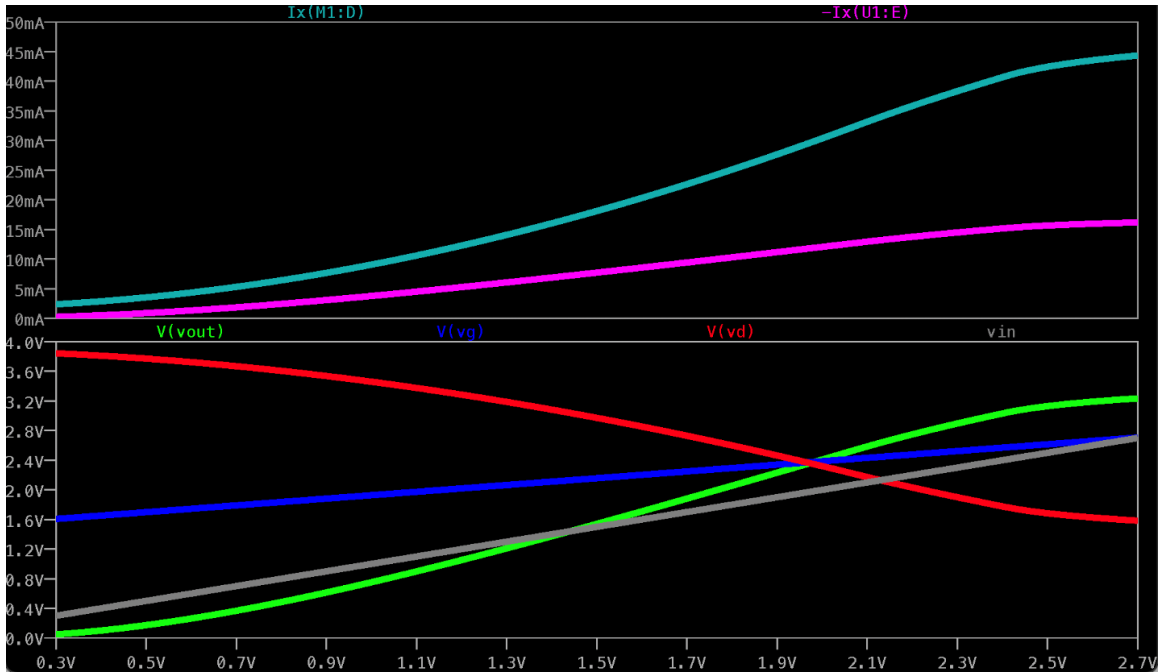
Figure. 63 Optocoupler and driver LTSPICE simulation data

Table. 8 Pertinent design quantities and ranges of optocoupler driver simulation

Value and range	Minimum	Maximum
Power detector output voltage (V_{pd})	0.3 V	2.7 V
MOSFET gate voltage (V_g)	1.55 V	3.0 V
MOSFET drain current (I_d)	4 mA	44 mA
Optocoupler BJT emitter current (I_e)	2 mA	16 mA
ADC input voltage (V_{out})	0.4 V	3.2 V

The final two linear equations are a partial result of empirically finding the gate

voltages required to drive the solved drain current. They also require an input range of

voltages for the transistor gate, which were calculated and approximated to correspond to

the expected output range of the power detector. The expected output range must

correspond to the calibration RF power used from the VCO and all the insertion losses

accrued throughout the leakage signal path. There is a fundamental trade-off now

between power detector output range and the corresponding ADC resolution. Since we

only care about finely characterizing the lower RF power inputs (thus high leakage signal

cancellation and isolation), the system was designed to seek out low RF power levels

while lumping together, thus practically disregarding higher RF power levels. Higher RF

powers do not matter for calibration but the system could later be redesigned for when

STAR wants to be integrated into other systems like power monitoring. The full RF

power detection system was characterized and plotted in figure 64. The x-axes represent

the RF power input to the PCBA in dBm and the y-axes represents the output voltage to

the ADC in mV. It can be seen that the system is most linear from around -40 dBm to –

25 dBm but there is a noticeable signal change from -50 dBm up to -49 dBm, thus the

system can find high isolation.

R_1 and R_G were selected as 11 kΩ, thus not straining the current requirements of

the opamp and allowing reasonable values of R_2 and R_F for which to be solved. R_2 and R_F

were found to be 52.47 kΩ and 9.75 kΩ, respectively. R_d was selected to be 54.9 Ω and

R_e was selected to be 60.4 Ω. The final circuit layout and PCBA are shown in figure 65.
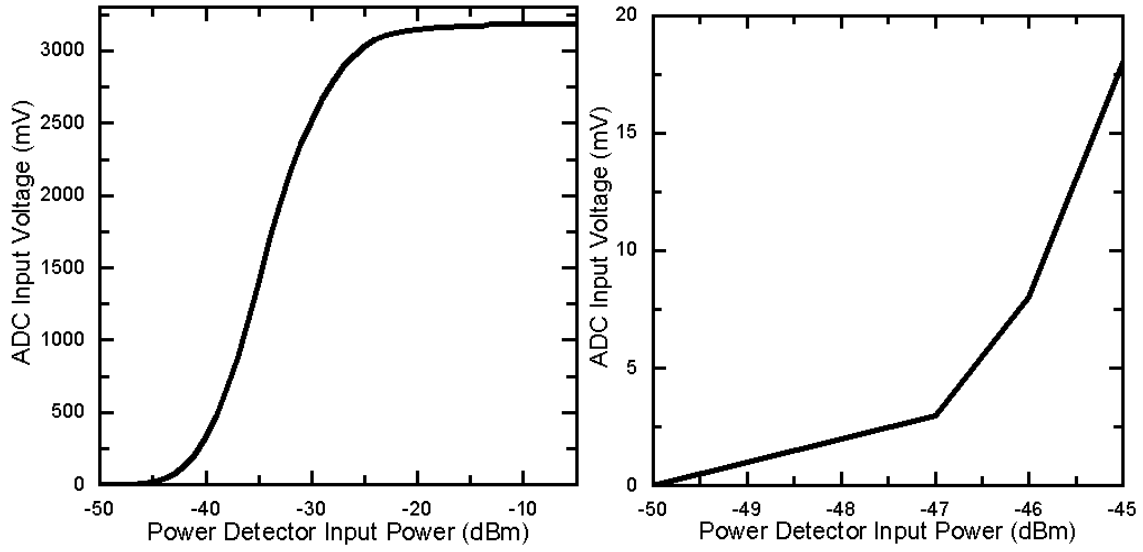
Figure. 64 Circuit layout and PCBA for output power coupler and detector
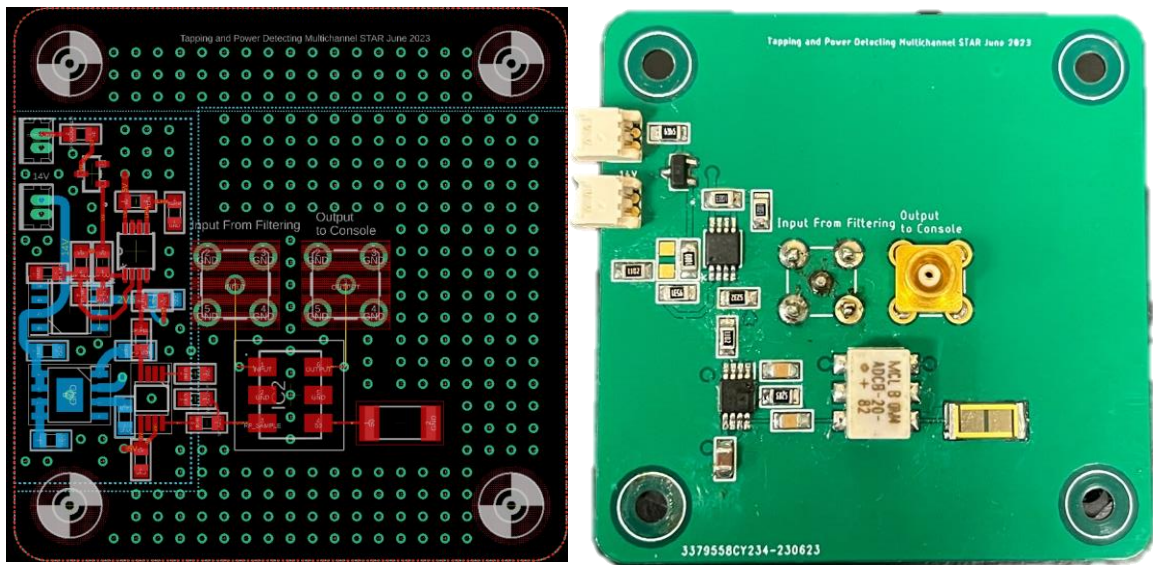
Figure. 65 Power detector with optocoupler driver layout and PCBA

4.5.3.10 STAR NMR Path Insertion Loss

The insertion loss of a STAR system is defined here as the insertion loss the NMR signal undergoes, thus the insertion loss of the receive chain. This path is shown explicitly in figure 66 by the thick green arrow where the signals goes through the following stages after being picked-up by the RF coil(s): cable traps, filters, power combiners, RF sampling couplers, and of course, all the coaxial cables used to connect these various components. Keeping this insertion loss to a minimum is necessary with the current system due to the lack of an LNA on the receive coil. STAR would greatly benefit from an extremely low noise and low gain amplifier attached to each receive coil, since the noise figure of the receive chain would decrease. Also, this would further increase the isolation of each receive coil from one another for a multichannel system, similar to the LNA now used in the cancellation channels. The insertion loss and return losses of the NMR signal path without the cable traps, since they were individually characterized previously, and without the coaxial cables, since they would be nominally unknown in a random imaging experiment, was measured and shown in figure 67. Port 1 is the input to the filter and port 2 is the output of the power detector coupler.
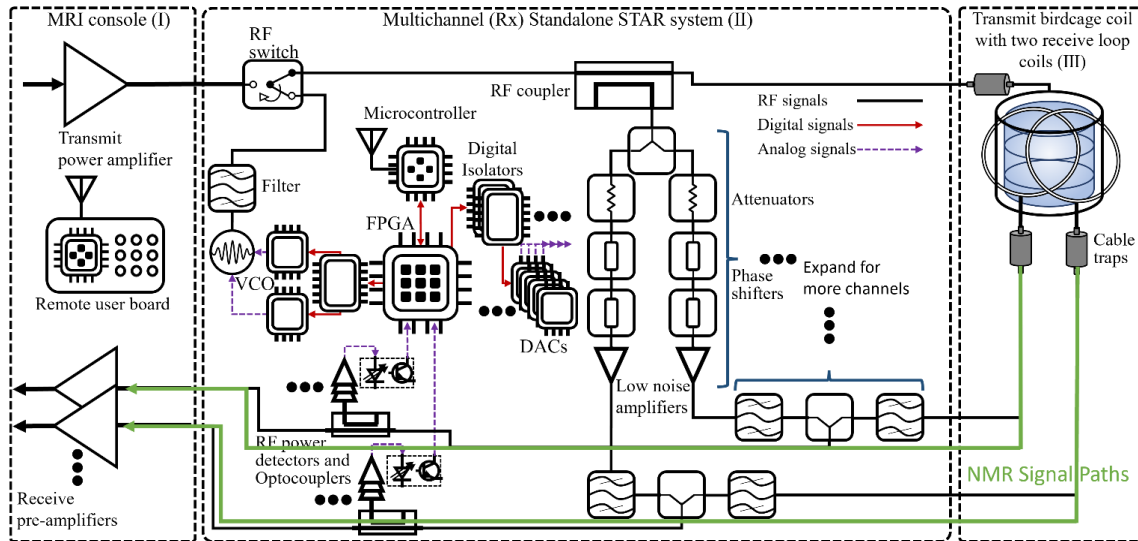
Figure. 66 STAR NMR receive chain path

The minimum insertion loss is 3 dB due to the Wilkinson power combiner required in the NMR signal path. This loss could be mitigated, however, if a small LNA were placed within the matching circuit of the receive coils, thus drastically increasing the SNR of the NMR signal. The return losses were measured at 64 MHz to be 24.65 dB and 27.64 dB and the insertion loss was measured to be 4.22 dB, thus 1.22 dB above the minimum.
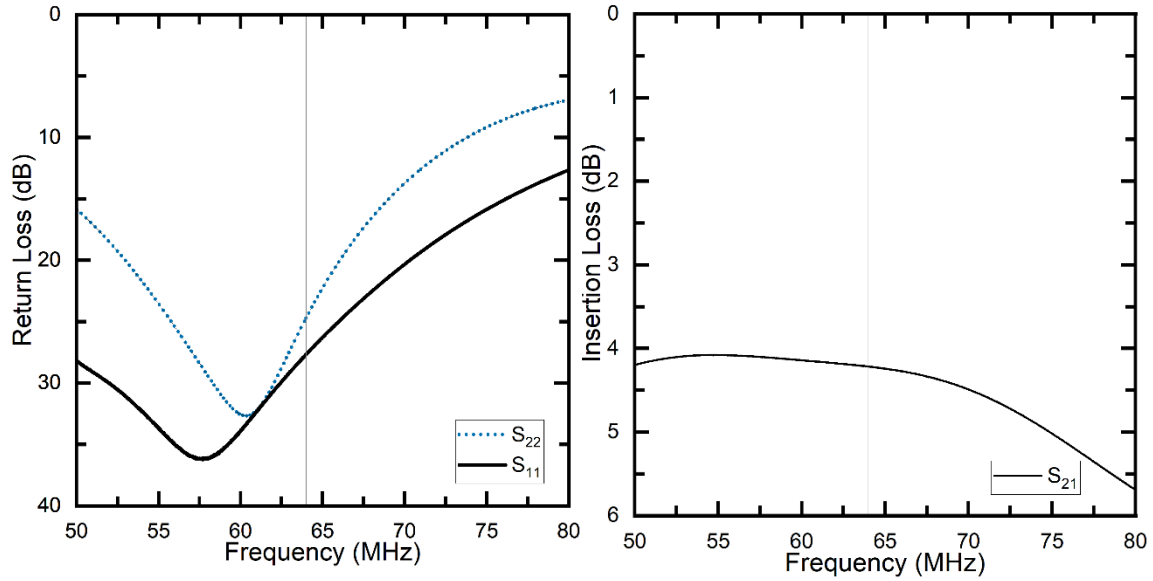
Figure. 67 NMR path return loss and insertion loss

4.5.3.11 Multichannel STAR Isolation Data

Multichannel STAR was implemented and tested with a single transmit volume coil (coil 1) and two individual receive surface loop coils (coils 2 and 3). The coils used were previously shown PCB coils and the same as those used in the standalone STAR publication.

First, the coils were tuned to resonate at 64 MHz and their return loss and geometric isolation were measured. S_{31} and S_{21} represent the isolation between the transmit coil and each of the receive coils, which is the fundamental measurement required to characterize a self-interference cancellation system. S_{32}, represents the isolation between the two receive coils. Figure 68 show the return loss for each coils 1, 2, and 3 to be 24 dB, 37 dB, and 21 dB, respectively at 64 MHz. Figure 69 show the

geometric isolation between coil 1 with coil 2, coil 1 with coil 3, and coil 2 with coil 3 to

be 25 dB, 12 dB, and 6.8 dB, respectively.
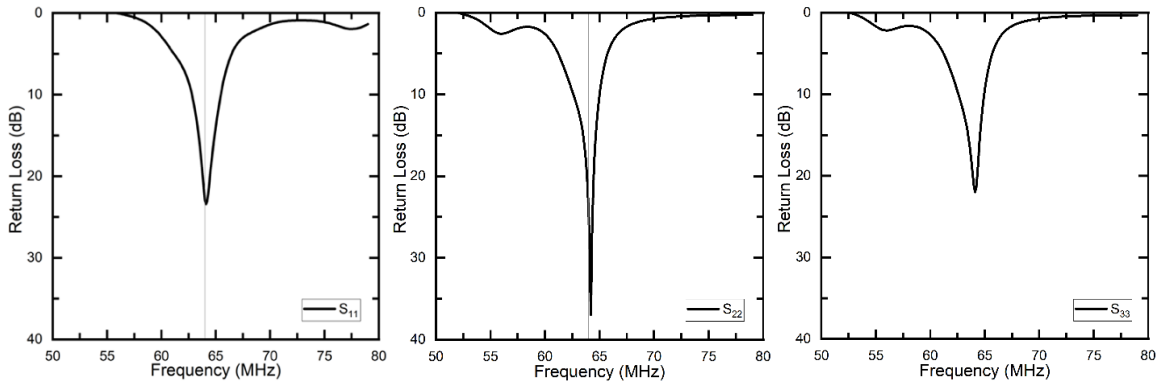
Figure. 68 Multichannel STAR RF coil return loss
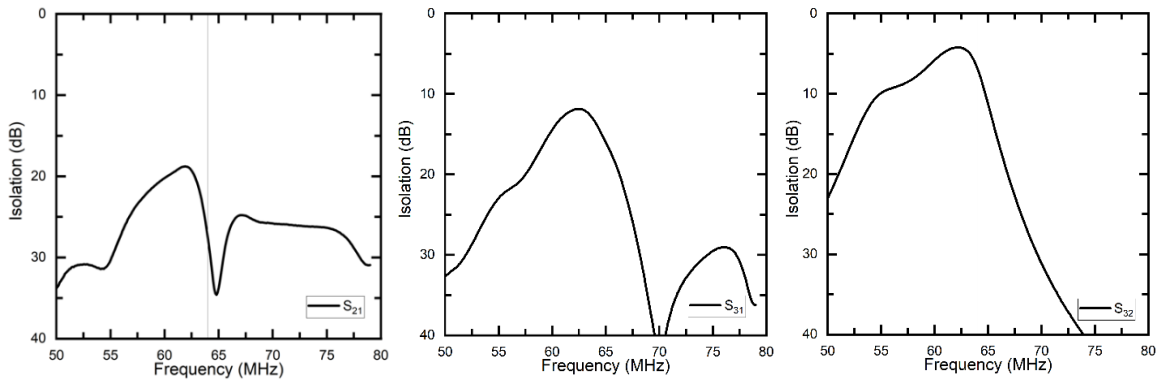
Figure. 69 Multichannel STAR coil geometric isolation before calibration

Unique to parallel MRI and multichannel STAR, however, is S_{32}. S_{32} represents the isolation the receive channels have between each other. This is important to consider since a receive coil leaking energy into another receive coil can cause image artifacts. This is a general problem in parallel MRI and a general measurement for multichannel systems involves sensitivity matrices to characterize channel isolation. Unique to STAR is coupling energy between one receive coil and the cancellation channel of another receive coil. This would inject a signal from one channel to another through a circuit path and detune the cancellation signal. This means that high receive coil isolation and cancellation channel isolation must also be intrinsic to the system. One reason why the cancellation channel LNA was chosen was due to its high reverse isolation (S_{12}), thus assuring the coupling of energy between receive coils does not detune their cancellation signals. After measuring the intrinsic coil isolation and return loss, the STAR system was connected to the coils, the microcontroller was connected to an Android tablet, and the STAR algorithm was initiated with the Android tablet. Phase shifters were swept from 0 V to 12 V and attenuators were swept from 1 V to 4 V. Once completed, the tablet was used to fine-tune the control voltages and optimize S_{21} and S_{31} as high as possible. The new isolation data is shown in figure 70 where it is clear that the isolation has reached more than 60 dB for both channels. Interestingly enough, the S_{32} isolation also increased as shown in figure 71. I believe this is primarily due to the slight impedance change of the cancellation channel due to different control voltages and the impact should not have any negative consequences on the image, rather, the increased isolation would decrease the chance of image artifacts.
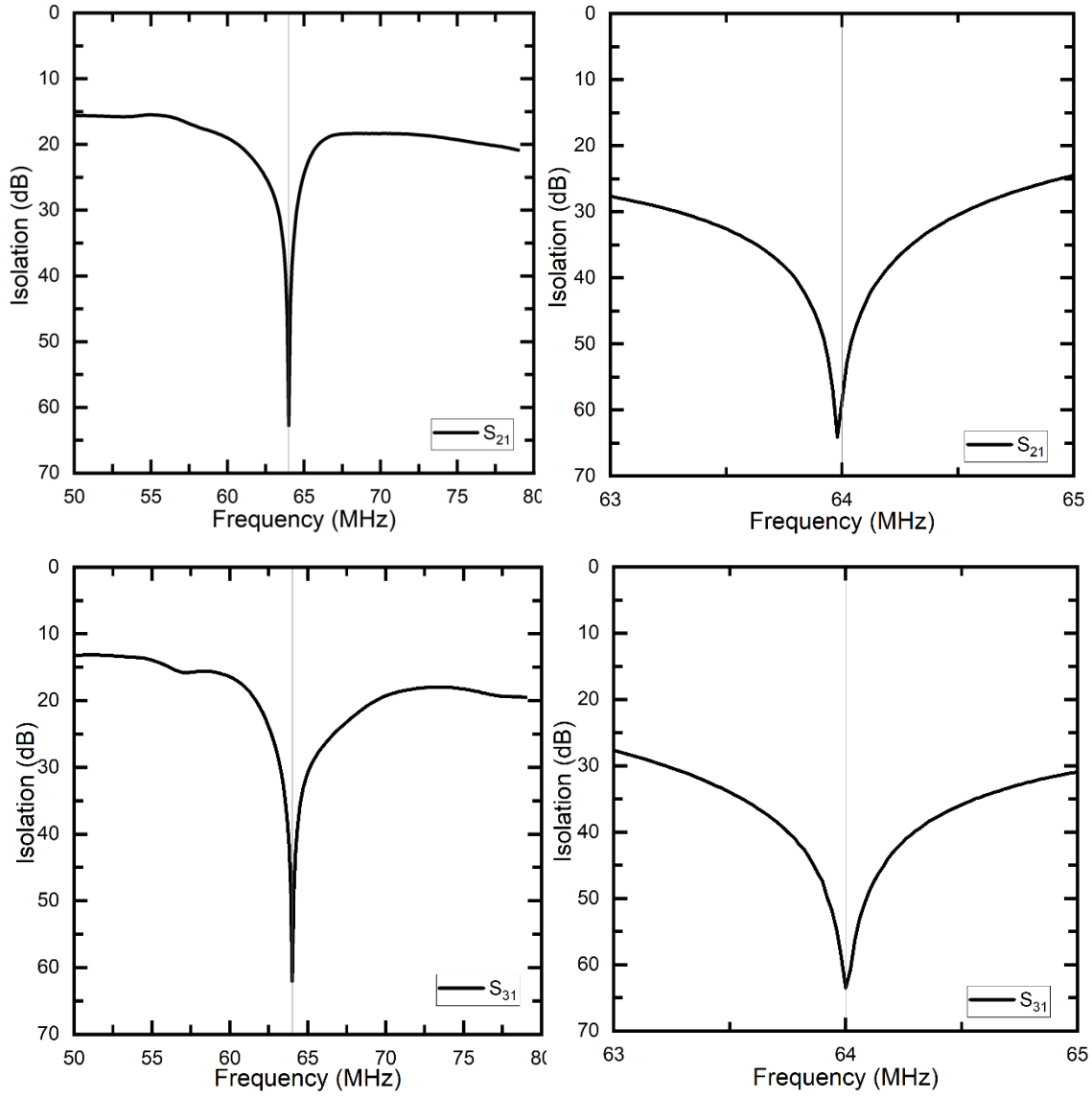
Figure. 70 Multichannel STAR transmit-receive coil isolation after calibration
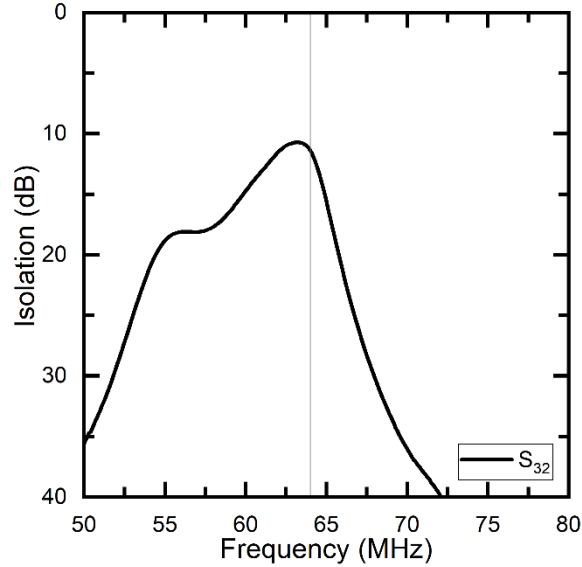
Figure. 71 Multichannel STAR receive coil isolation after calibration

The current primary two issues with STAR are isolation stability and isolation bandwidth. Both of which hopefully have future solutions now enabled by reducing system noise. If the STAR system can be programmed to do a small recalibration in short intervals during imaging, then the stability is less impactful since a high isolation state would be consistently reintroduced. This could either pair with a trigger signal from the console or be internally timed, similar to the self-calibration, to occur during less impactful k-space acquisitions. This is precisely where system timing begins to show impact. The quicker the recalibration, then the less impact the calibration would have on the final image. The same idea can be expanded to bandwidth. As the Larmor frequency is slowly swept, STAR could also sweep the phase shifter control voltages to match with high isolation. Both of these example concepts require extremely high noise decoupling between the STAR electronics and the RF signal paths.

4.6 System Timing

The entire system timing depends on the reference oscillator fed into the FPGA. The DE0 nano development board has an onboard 50 MHz oscillator and a phase locked loop module for hence creating a 50 MHz clock reference clock that can be slowed down as needed. Other potentially pertinent considerations for timing are that the DACs have a maximum settling time of 9 us, the optocouplers have a maximum settling time of 20 us, the digital isolators have a propagation delay of 11 ns, and a channel-to-channel max skew time of 6 ns and the ADC has a maximum clock input of 3.2 MHz.

The DACs used (AD5761, Analog Devices) use a 24-bit serial peripheral interface (SPI) transaction to set the output voltage from the FPGA. The output voltage range can be configured by sending commands to the control register, which was set to the range of 0 V to 16 V to accommodate the voltage-controlled phase shifter range and set to 0 V to 5 V to accommodate the voltage-controlled attenuator range. Setting up the DACs is a simple three step process: 1. Send the reset command. 2. Configure the control register. 3. Send the DAC data as needed. A diagram of a DAC transaction can be seen below in figure 72, which is a screenshot of a logic analyzer viewing FPGA pins. The top plot is the clock, the following plot is the chip select, and the next six plots are of the data being sent to each of the six DACs. The first two data outputs are for the VCO control and power and the following four are for the phase shifters and attenuators.
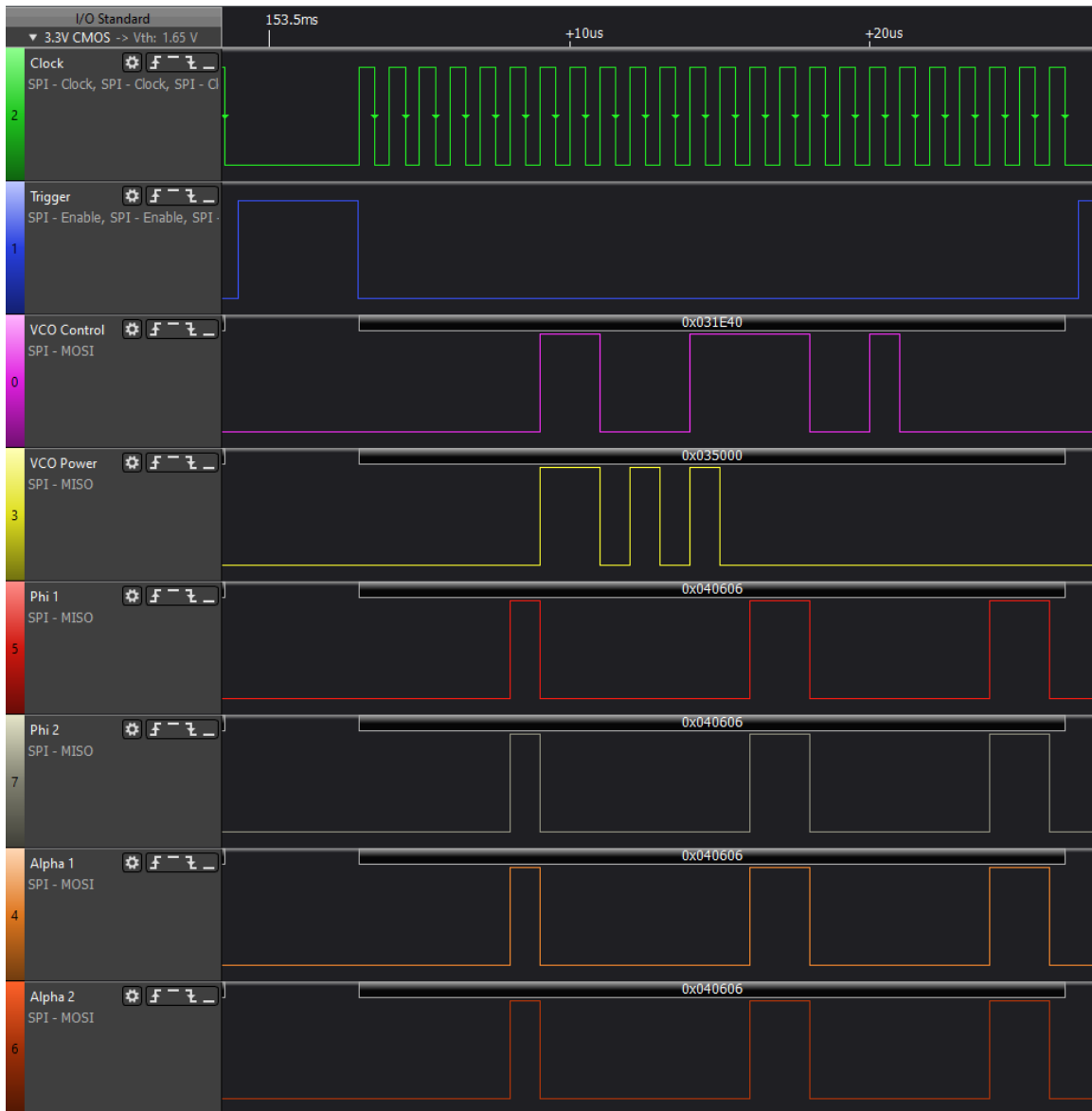
Figure. 72 Example DAC SPI transactions for all six DACs used in two channel STAR

Calculating the total calibration time can either be done using the device control voltage ranges and voltage increments or done in the binary world using the data that corresponds to the voltage increments. Either way, the same result is achieved and the conversions between the two worlds are tabulated below for clarity. The conversion

113

between binary data and the voltage output of the DAC is done simply by using equation
26.

$$\frac{V_{max}}{2^{16}} \times Binary = V_{out}$$

Equation. 26 Conversion from binary data to voltage output of the DACs

Table. 9 Phase shifter and attenuator voltages and corresponding binary data

Component	Measured Value	Voltage	Binary
Phase Shifter	V_{max}	12 V	1100_0000_0000_0000
	V_{min}	0 V	0000_0000_0000_0000
	ΔV	16/256 V	0000_0001_0000_0000
Attenuator	V_{max}	4 V	1100_1100_1100_1101
	V_{min}	1 V	0011_0011_0011_0011
	ΔV	5/256 V	0000_0001_0000_0000

The total calibration time is dependent on how many channels are present (N), the
clock rate, how many clock cycles are required to increment a DAC data register, the
increment voltage of the phase shifter and attenuator, and the voltage ranges of the phase
shifter and attenuator as shown below in equation 27.

$$Total\ calibration\ time = \ N\frac{\left(\frac{V_{max1} - V_{min1}}{\Delta V_1}\right)\left(\frac{V_{max2} - V_{min2}}{\Delta V_2}\right)\left(\frac{clock\ cycles}{\Delta bit}\right)}{clock\ rate}$$

Equation. 27 Total calibration time of multichannel STAR

Using the control voltage data provided above in table 9, a 28-bit transaction for incrementing a bit and a clock of 1 MHz yields a total calibration time of only 3.67 seconds for two channel STAR. If more resolution is required for a more accurate calibration, then the increment voltages can be decreased at the expense of time. Although multichannel STAR digital hardware was designed to operate with faster clock rates, a 1 MHz clock is clearly not critically disadvantageous for a fast calibration. As channel count increases, however, the system should be sped up to accommodate. One can also notice that the phase shifter is only swept up to 12 V instead of the full range of 16 V and the attenuator is swept from 1 V to 4 V instead of the full 5 V range. Since only a phase range of 360° is needed to match any RF coil, 4 V of control voltage range was able to be removed and speed up the system 25%. Similarly, the addition of the LNA in conjunction with the highly-nonlinear attenuator, only a small range of attenuation values must be swept, thus speeding up the system an additional 40%.

The DACs require 24 bits to be transferred in each transaction and the ADC only requires 12 bits, the system timing revolves around the DAC updating. This also drastically reduces the effective update time required from the optocoupler, thus even a 1 MHz optocoupler can be reasonable for a 25 MHz system.

4.7 Digital Signal Integrity

For RF engineers signal integrity is often boiled down about to terms of SNR. This includes many different components such as impedance matching, standing waves, transmission line coupling, noise sources from components, radiation losses, other electromagnetic interferences, and more. Although these are all important for modern systems to function, high speed digital circuits and power delivery networks also face the same issues and are worth exploring for a STAR system.

Transmission lines are not reserved for narrowband RF signals; they are also driven with digital data, where the functionality of transmitting high bandwidth square waves is paramount to transfer data safely. The maximum frequency of operation for the FPGA used in STAR is 50 MHz, for the DACs is 50 MHz, for the ESP32 is 80 MHz, and for the digital isolators is 50 MHz (actually 50 Mbps with SPI pushing 1 bit/second). Although these top speeds were not realized in the system, it is good to recognize how the system could advance in the future and make sure the hardware is ready.

Keeping PCB traces at similar lengths is important, lest a clock edge and a data read/write could not be synched, and the entire communication fails. When routing signals from the GPIO pins of one device to those of another, this can be difficult to achieve since the designer is at the mercy of device layout. This leads us to meandering. Meandering is the idea of artificially lengthening some of your lines to match the natural length of your longest line. Meandering was performed on all SPI lines on the board. The longest digital line on the PCB with digital devices is 78 mm between the FPGA and the microcontroller. This was intended to be used for SPI communication therefore the other three SPI lines were meandered to also be 78 mm for timing. All of the other digital lines

were under 12.5 mm, thus calibration time is practically able to be faster than FPGA-microcontroller communication. Unfortunately for signal integrity, the rise time for the FPGA signals can be as low as 0.5 ns, depending on the pin driving technology chosen. If we use the unterminated rule-of-thumb presented by Bogatin that the signal travel time over the transmission should be shorter than the rise time, then the longest line should thus be less than 15 mm [Bogatin]. Since this is not entirely possible with the current design, system parameters involving signal integrity were simulated.

The FPGA and microcontroller are at the heart of the system and use the digital isolators and DACs as peripherals. Thus, to understand the FPGA driving requirements, we need to understand the rise times of the pins generating data signals, their driving impedance, and the pin capacitances of the devices receiving digital signals. As previously mentioned, the FPGA generates signals with a rise time as small as 0.5 ns and has a pin capacitance of up to 8 pF. The digital isolators generate signals with a rise time of 3.2 ns and have a pin capacitance of 2.8 pF. The microcontroller has a pin capacitance of 2 pF yet the data sheets do not provide information about signal rise time. Finally, the DACs have a pin capacitance of 5 pF. If we can formulate a relationship between capacitance, rise time, and operating voltage, we then know how much current the FPGA must source to drive faster data rates to the digital isolators, and how much current is needed for the digital isolators to drive the DACs. Currently, the FPGA receives simple rising edge signals from the microcontroller, thus the other device relationships are more appropriate to explore in terms of signal integrity. The first order approximation for drive strength is simply the current required to be sourced to a capacitive load shown in equation 28.

$$i(t) = C\frac{\partial V(t)}{\partial t}$$

Equation. 28 Current drive needed for a capacitive load

For example, if the FPGA is driving the digital isolator using 3.3 V logic with a 0.5 ns rise time and a 2.8 pF pin capacitance, then the maximum current required is approximately:

$$i \approx 2.8\ pF \cdot \frac{3.3\ V}{0.5\ ns} = 16.8\ mA$$

The GPIO pins on the DE0 nano development board operate by default using a 2.5 V LVTTL driver technology with a fortunately configurable 50 Ohm series resistor that drives up to 8 mA of current and can be reconfigured to drive up to 16 mA, thus the slew rate of the FPGA pins should be configured to increase the rise time. It should be noted that the 2.5 V LVTTL standard operates with voltage levels of 3.3 V, thus the naming is a bit confusing. Regardless, the same calculation can be applied to any digital connections where the devices have understood voltage and current standards and the pins have defined impedance and rise times. The same calculation applied between the isolators and the DACs yields a driving current of 5.16 mA.

ADS simulations were done with the FPGA, microcontroller, and digital isolator parameters to view a realistic maximum data rate with which they could communicate without causing damage over 12.5 mm and 78 mm grounded coplanar waveguides. This same simulation can be performed between any two components talking digitally. There are methods of mitigating damage, of course, which involve techniques such as resistive

matching or employing snubbing resistors to decouple two chips. Knowing exactly which values to use can be difficult to predict so software like ADS.

The ADS schematic in figure 73 is the circuit used for testing, which includes the 50 MHz clock, the driving resistance, the transmission line used, the load resistance, and the load capacitance.
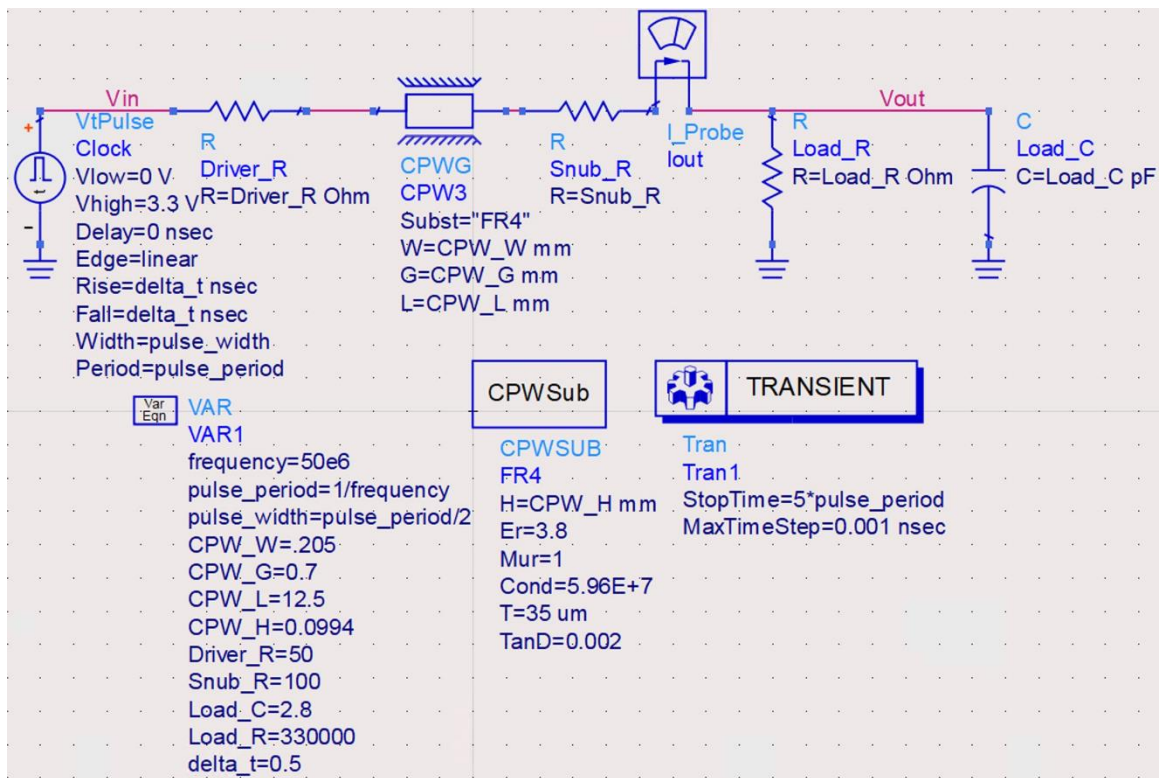
Figure. 73 ADS signal integrity schematic

Snub resistor values from 0 Ω to 100 Ω were tested with rise times down to 0.5 ns. Since the FPGA driver is 50 Ω, the snub resistors did not change the results much other than the drive current. For example, a 78 mm transmission line with a load capacitance of 2 pF, a load resistance of 66 MΩ, and a rise time of 0.5 ns, a snub resistor of 0 Ω required 13.43 mA and a snub resistor of 100 Ω required 10.81 mA. These results

are rather insignificant. To highlight the importance of understanding your driver and termination parameters, the driver resistance was reduced to 10 Ω and the snub resistor swept again from 0 Ω to 100 Ω. Since the driver resistance was so low, the snub resistor once again did not have much of an effect, although this time, the clock was completely unacceptable and the current driving is not possible to meet, as shown in figure 74.
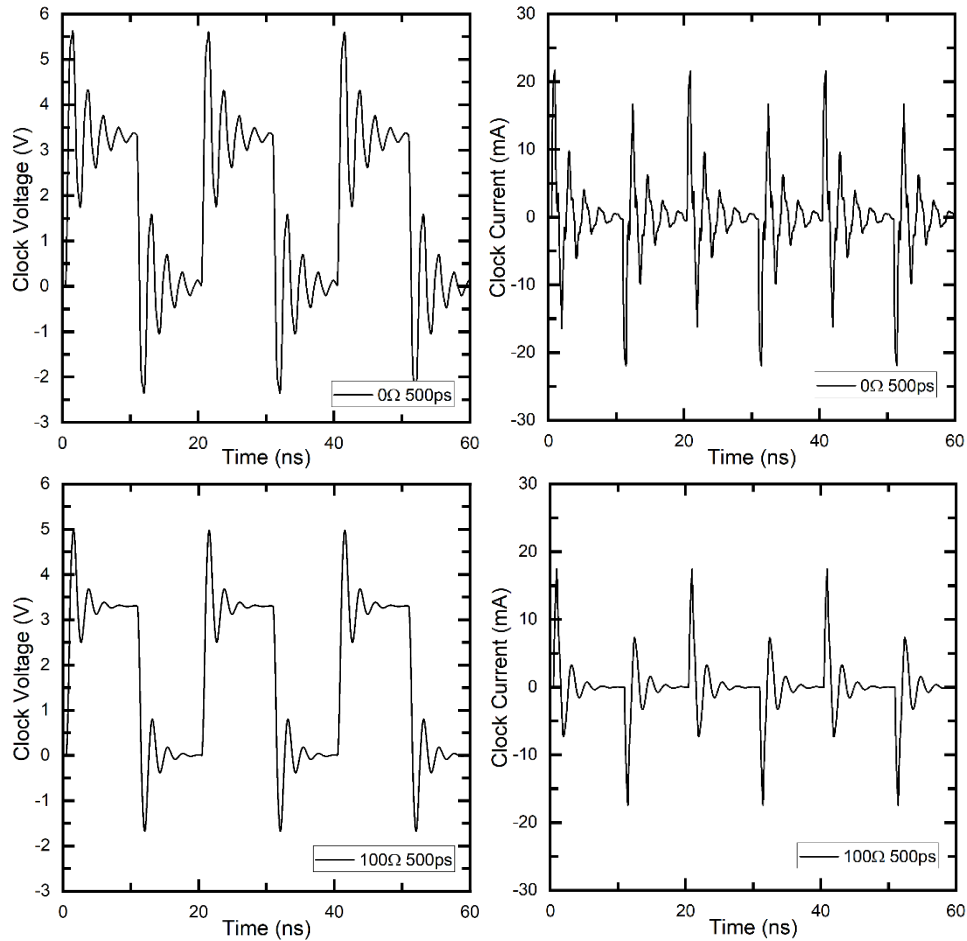
Figure. 74 Clock signals for a 10 Ω driver with 500 ps rise times and snub resistors

We can mitigate this issue by increasing the rise time to 2 ns as shown in figure 75. If this rise time is not acceptable for timing constraints, then we can maintain a 0.5 ns rise time and ensure the FPGA configures its driving resistance to 50 Ω, as also shown in figure 75. This was the method chosen for STAR since the FPGA has a 50 Ω output driver. If that ends up not solving the problem, then the slew rate is also configurable.
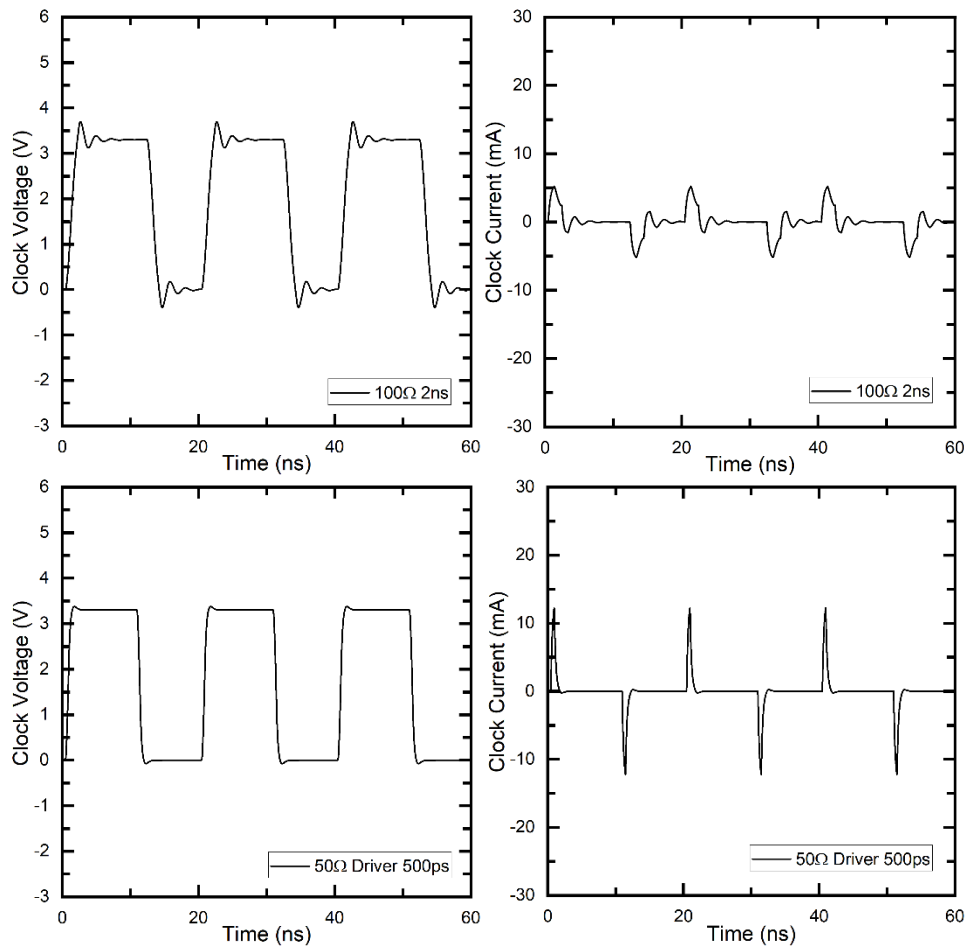
Figure. 75 Clock voltages and current driving requirements for a 10 Ω driver with 2 ns rise times in a 50 Ω system and a 100 Ω snub resistor or for a 50 Ω driver with 500 ps rise times and a 100 Ω snub resistor

CHAPTER 5

DISCUSSION AND CONCLUDING REMARKS

Full duplex continuous wave MRI is a new technology with a lot of distance to traverse before being integrated into a standard MRI ecosystem. Although images were decades away from being constructed, Bloch proved continuous wave NMR to be possible in 1946. Since then, efforts in pulse sequence design and MRI hardware have rapidly advanced and one sliver of this development is STAR. The precursor to STAR was continuous SWIFT, and since 2012 many efforts have been made globally to develop STAR hardware. Specifically for MRI, efforts have been made for general-purpose RF coil isolation, destructive interference-based leakage signal isolation, algorithmic leakage signal isolation, digital domain isolation through curve fitting the leakage signal and unique circuits such as a nonmagnetic STAR gyrator. I can only hope that standalone multichannel STAR has helped develop a future suite of MRI technology through its user interface, scalability, and general-purpose application. This suite is not necessarily limited to full duplex imaging, rather, aftermarket MRI electronics and systems that boost the possibilities of MRI clinically or in research.

There are a few avenues to explore when it comes to the future of STAR for MRI. The current system could be refined and developed into a standalone product to retrofit modern clinical MRI machines. This is the most organic path to take with minimal changes and overhead. It also caters primarily to adiabatic and low RF power pulse sequences since the current RF hardware is primarily low power. My long-term vision for STAR is a small, sleek, and sophisticated almost entirely IC-based design. Ideally it would be wideband, thus operating for proton and X-nuclei from 0.1T through > 20T for

clinical imaging, preclinical imaging, and NMR spectroscopy. The cancelation channel could be replaced with modern modulation/demodulation circuits, such as those found in the ADL5390 from Analog Devices. The VCO board could be replaced with frequency synthesizer circuits like those found in the ADF4356 from Analog Devices. Most of the other circuits are already off-the-shelf ICs such as FPGAs, microcontrollers, RF switches, etc. The most difficult circuits to handle would be couplers and power combiners, thus initial research would likely be done on a switch-based system for a few discrete frequencies or using software defined radio.

Self-interference cancellation is applicable beyond just low power sequences. ZTE and UTE pulse sequence are the most akin in purpose to continuous SWIFT and would be good first choices to demonstrate a general-purpose self-interference isolation system [68.69]. A general-purpose system would take the principles of STAR, upgrade it to handle high RF power levels, and apply it to ring down signals instead of continuous-wave self-interference leakage signals. Theoretically, this would push any pulse sequence to readily image tissues or materials with a short T_2 time constant, thus reserving STAR itself for applications where low power, cost, and portability are strictly necessary.

Another possibility is to integrate STAR into a unique MRI console and MRI machine framework, or in other words, to develop and entire MRI or NMR spectroscopy ecosystem with STAR at its core. This redefines the identity of MRI or NMR spectroscopy in a way that still caters to low power pulse sequences and consequently does not carry the extra requirements of a high power devices found in typical systems.

With the current applications of STAR, I see a STAR IC being the natural next step for a standalone product if clinical imaging systems were able to be readily

upgraded. If the intended application were custom portable or low power MRI systems, then a STAR console is the most advantageous and unique way to utilize and grow STAR MRI as a product. This custom console could be a project on its own, thus using a modular PCB-based STAR ecosystem as demonstrated in this thesis, or it could be the natural evolution of a STAR IC. Finally, a high power self-interference cancellation system for clinical imaging would have the most diverse application with the most headroom in terms of cost, safety, and power requirements. Before STAR can be fully applied to its applications or developed into new technologies, however, it must first improve isolation bandwidth and stability.

REFERENCES

[1] J. Larmor, "On the theory of the magnetic influence on spectra; and on the radiation from moving ions," *Phil. Mag*, series 5, vol 44, pp. 503-512, 1897.

[2] F. Bloch, "Nuclear Induction," *Phys. Rev*, vol. 70, no. 7, pp. 460-474, 1946.

[3] F. Bloch, W.W. Hansen, M. Packard, "The Nuclear Induction Experiment," *Phys. Rev*, 70(5), 474–485.

[4] E. M. Purcell, H. C. Torrey, and R. V. Pound, "Resonance Absorption by Nuclear Magnetic Moments in a Solid," *Phys. Rev*, vol. 69, iss. 1-2, 1946.

[5] E. L. Hahn, "Spin Echoes," *Phys. Rev*, vol. 80, iss. 4, 1950.

[6] B. A. Jung and M. Weigen, "Spin Echo Magnetic Resonance Imaging," Journal of Magnetic Resonance Imaging. 37;805-817. 2013.

[7] R. R. Ernst and W. A. Anderson, "Application of Fourier Transform Spectroscopy to Magnetic Resonance," *Rev. Sci. Instrum*., vol. 37, no. 1, pp. 93-102, 1966.

[8] D. Idiyatullin, S. Suddarth, C. Corum, G. Adriany, and M. Garwood, "Continuous SWIFT*," J. Magn. Reson*., pp. 26–31, 2012.

[9] A. Tannus and M. Garwood, "Adiabatic pulses," *NMR in Biomed*, vol. 10, pp. 423-434. 1997.

[10] R. A. DeGraaf and K. Nicolay, "Adiabatic RF pulses: Applications to *in vivo* NMR," *Concept. Magn. Res*. vol. 9, pp. 247-268, 1997.

[11] M. Garwood and L. De la Barre, "The return of the frequency sweep: Designing adiabatic pulses for contemporary NMR," *J. Magn. Reson.* vol. 153, pp. 155-177, 2001.

[12] J. Wang, W. Mao, M. Qiu, M. B. Smith, and R. T. Constable, "Factors Influencing Flip Angle Mapping in MRI: RF Pulse Shape, Slice-Select Gradients, Off-Resonance Excitation, and B_0 Inhomogeneities," *Magn. Reson, Med*., vol. 56, no. 2, pp. 463-468, 2006.

[13] R. Chamberlain, S. Moeller, C. Corum, D. Idiyatullin, and M. Garwood, "Quiet T1 and T2-weighted brain imaging using SWIFT," in Proc. 20th Int. *Soc.Magn.Res. Med*., 2011, p. 2723.

[14]   B. van Liempd, C. Lavin, S. Malotaux, C. Lavín, B. Debaillie, C. Palacios, J. R. Long, E.A.M Klumperink, and J. Craninckx "RF self-interference cancellation for full-duplex," 2014 9th International Conference on Cognitive Radio Oriented Wireless Networks and Communications (CROWNCOM), 2014, pp. 526-531, doi: 10.4108/icst.crowncom.2014.255756.

[15]   H. Zhao, J. Wang, and Y. Tang, "Performance Analysis of RF Self interference Cancellation in Broadband Full Duplex Systems," IEEE Int. Conf. Commun. Work., pp. 175–179, 2016.

[16]   E. A. Keehr , "A low-cost software-defined UHF RFID reader with active transmit leakage cancellation," 12th Annual IEEE International Conference on RFID., 2018, 1–8. https://doi.org/10.1109/RFID.2018.8376193.

[17]   S. A. Hassani, V. Lampu, K. Parashar, L. Anttila, A. Bourdoux, B. van Liempd, M. Valkama, F. Horlin, and S. Pollin, "In-Band Full-Duplex Radar-Communication System," IEEE Syst. J., vol. 15, no. 1, pp. 1086–1097, Mar. 2021.

[18]   C. B. Barneto, T. Riihonen, M. Turunen, L. Antilla, M. Fleischer, K. Stadius, J. Ryyännen, and M. Valkama, "Full-Duplex OFDM Radar with LTE and 5G NR Waveforms: Challenges, Solutions, and Measurements," IEEE Trans. Microw. Theory Tech., vol. 67, no. 10, pp. 4042–4054, 2019.

[19]   M. Mercuri, P. Barmuta, P. J. Soh, P. Leroux, and D. Schreurs, "Monostatic continuous-wave radar integrating a tunable wideband leakage canceler for indoor tagless localization," Int. J. Microw. Wirel. Technol., vol. 9, no. 8, pp. 1583–1590, 2017.

[20]   L. Luo and S. Li, "Influence of Full-Duplex Self-Interference Channel Measurement on Self-Interference Cancellation Capacity, " Proc. 2018 IEEE 8th Int. Conf. Electron. Inf. Emerg. Commun. ICEIEC 2018, pp. 63-66, 2018.

[21]   S. M. Sohn, J. T. Vaughan, R. L. Lagore, M. Garwood, and D. Idiyatullin, "In vivo MR imaging with simultaneous RF transmission and reception," Magn. Reson. Med., vol. 76, no. 6, pp. 1932–1938, 2016.

[22]   S. M. Sohn, M. Garwood and J. T. Vaughan, "Automatic RF leakage signal canceler in MRI applications," 2017 IEEE MTT-S International Microwave Symposium (IMS), Honolulu, HI, USA, 2017, pp. 1394-1395, doi: 10.1109/MWSYM.2017.8058876.

[23]   A. C. Özen, M. Bock, and E. Atalar, "Active decoupling of RF coils using a transmit array system," Magn. Reson. Mater. Phy., vol. 28, pp. 565-576, 2015.

[24] A. C. Özen, E. Atalar, J. G. Korvink, and M. Bock, "In vivo MRI with Concurrent Excitation and Acquisition using Automated Active Analog Cancellation," Sci. Rep., vol. 8, no. 1, pp. 1–12, 2018

[25] M. Salim, A. C. Ozen, M. Bock, and E. Atalar, "Active Isolation of Transmit and Receive Coils for Full-Duplex MRI," pp. 1–6, 2018.

[26] B. Tasdelen, A. Sadeghi-Tarakameh, U. Yilmaz, and E. Atalar, "Analysis and mitigation of noise in simultaneous transmission and reception in MRI," Magn. Reson. Med., vol. 86, no. 3, pp. 1746–1758, 2021.

[27] Z. A. Colwell, L. DelaBarre, D. Idiyatullin, G. Adriany, M. Garwood, J. T. Vaughan, and S-M. Sohn, "Standalone RF Self-Interference Cancellation System for In-vivo Simultaneous Transmit and Receive (STAR) MRI," IEEE Transactions on Biomedical Circuits and Systems. 2023.

[28] S. K. Kandala and S.-M. Sohn, "Design of standalone wireless impedance matching (SWIM) system for RF coils in MRI," Sci. Rep., vol. 12, no. 21604, 2022.

[29] P Zeeman, "Over de invloed eener magnetisatie op den aard van het door een stof uitgezonden licht," Verslagen van de Gewone Vergaderingen der Wis- en Natuurkundige Afdeeling (Koninklijk Akademie van Wetenschappen te Amsterdam). 5: 181–184 and 242–248. 1896

[30] A. G. Redfield, "Nuclear magnetic resonance saturation and rotary saturation in solids," Phys. Rev., vol. 98, no. 6, 1955.

[31] "Relaxation time, T1, T2," Questions and Answers in MRI. https://www.mriquestions.com/why-is-t1--t2.html (accessed Sep. 28, 2023)

[32] D. M. Pozar, Microwave engineering. Hoboken, Nj: Wiley, 2012.

[33] "PCB Manufacturing & Assembly Capabilities" jlcpcb.com https://jlcpcb.com/capabilities/pcb-capabilities (accessed Jun. 3, 2023)

[34] "Coplanar Waveguide With Ground Calculator," chemandy.com. https://chemandy.com/calculators/coplanar-waveguide-with-ground-calculator.htm (accessed Sep. 28, 2023).

[35] M. Wilcox, S. M. Wright, and M. P. McDougall, "Multi-Tuned Cable Traps for Multinuclear MRI and MRS," IEEE Transactions on Biomedical Engineering, vol. 67, no. 4, pp. 1221–1228, Apr. 2020, doi: https://doi.org/10.1109/tbme.2019.2933733.

[36]   Ekin Karasan, A. Hammerschmidt, Ana Claudia Arias, V. Taracila, F. Robb, and
        M. Lustig, "Caterpillar traps: A highly flexible, distributed system of toroidal
        cable traps," *Magnetic Resonance in Medicine*, vol. 89, no. 6, pp. 2471–2484, Jan.
        2023, doi: https://doi.org/10.1002/mrm.29584.

[37]   S. Ramo, J. R. Whinnery, and Theodore Van Duzer, *Fields and Waves in
        Communication Electronics*. Wiley, 1994.

[38]   "Introduction to NMR/MRI Amplifiers | CPC Amps," *www.cpcamps.com*.
        http://www.cpcamps.com/introduction-to-nmr-mri-amplifiers.html (accessed Sep.
        28, 2023).

[39]   C. E. Hayes and L. Axel, "Noise performance of surface coils for magnetic
        resonance imaging at 1.5 T," *Medical Physics*, vol. 12, no. 5, pp. 604–607, Sep.
        1985, doi: https://doi.org/10.1118/1.595682.

[40]   C. A. Balanis, "Antenna Theory, Analysis and Design," p. 1072, 2016.

[41]   C. E. Hayes, W. A. Edelstein, J. F. Schenck, O. M. Mueller, and M. Eash, "An
        efficient, highly homogeneous radiofrequency coil for whole-body NMR imaging
        at 1.5 T," *Journal of Magnetic Resonance (1969)*, vol. 63, no. 3, pp. 622–628, Jul.
        1985, doi: https://doi.org/10.1016/0022-2364(85)90257-4.

[42]   S. F. Ahmad, Y. C. Kim, I. C. Choi, and H. D. Kim, "Recent Progress in Birdcage
        RF Coil Technology for MRI System," *Diagnostics*, vol. 10, no. 12, p. 1017, Nov.
        2020, doi: https://doi.org/10.3390/diagnostics10121017.

[43]   Y. C. Kim, H. D. Kim, B.-J. Yun, and S. F. Ahmad, "A Simple Analytical
        Solution for the Designing of the Birdcage RF Coil Used in NMR Imaging
        Applications," *Applied Sciences*, vol. 10, no. 7, p. 2242, Jan. 2020, doi:
        https://doi.org/10.3390/app10072242.

[44]   C.-L. Chin, C. M. Collins, S. Li, B. J. Dardzinski, and M. S. Smith,
        "BirdcageBuilder: Design of specified-geometry birdcage coils with desired
        current pattern and resonant frequency," vol. 15, no. 2, pp. 156–163, Jun. 2002,
        doi: https://doi.org/10.1002/cmr.10030.

[45]   G. H. Glover, C. E. Hayes, N. J. Pelc, W. A. Edelstein, O. M. Mueller, H. R. Hart,
        C. J. Hardy, M. O'Donnel, and W. D. Barber, "Comparison of linear and circular
        polarization for magnetic resonance imaging," *J. Magn Reson*. vol. 64, pp. 255-
        270. 1985.

[46]   M. A. Bernstein, K. F. King, and X. J. Zhou (2004). Handbook of MRI pulse
        sequences. Amsterdam: Academic Press.

[47] D. Idiyatullin, C. Corum, J.-Y. Park, and M. Garwood, "Fast and quiet MRI using a swept radiofrequency," *Journal of Magnetic Resonance*, vol. 181, no. 2, pp. 342–349, Aug. 2006, doi: https://doi.org/10.1016/j.jmr.2006.05.014.

[48] J. B. Miller, B. H. Suits, A. N. Garroway, and M. A. Hepp, "Interplay among Recovery Time, Signal, and Noise: Series-and Parallel-Tuned Circuits Are Not Always the Same," Concepts in Magnetic Resonance (Vol. 12). John Wiley & Sons, Inc. 2000.

[49] D. Idiyatullin, C. Corum, S. Moeller, H. S. Prasad, M. Garwood, and D.R. Nixdorf, "Dental magnetic resonance imaging: making the invisible visibl,". *J Endod*. vol. 37, no. 6, pp. :745-752. 2011.

[50] M. T. Nelson, J. C. Benson, T. Prescott, C. A. Corum, A. Snyder, and M. Garwood, "Breast MRI using SWeep Imaging with Fourier Transform (SWIFT)," *European Journal of Radiology*, vol. 81, p. S109, Sep. 2012, doi: https://doi.org/10.1016/s0720-048x(12)70044-x.

[51] Z. A. Colwell, D. Idiyatullin, L. DelaBarre, T. Vaughan, M. Garwood, and S.-M. Sohn, "Passive Tunable RF Leakage Canceller for Simultaneous Transmit and Receive (STAR) RF Coils at 1.5T Imaging." In Proc. 30th Int. Soc. Magn. Resonance Med., 2021, p.1406

[52] W. -G. Lim, S. -Y. Park, S. -Y. Lee, M. -Q. Lee and J. -W. Yu, "Balanced Directional Coupler Structure with Insensitive Isolation for Load Impedance," 2008 38th European Microwave Conference, 2008, pp. 1280-1283, doi: 10.1109/EUMC.2008.4751696.

[53] A. Nagulu, A. Kord, G. Tong, M. Garwood, L. De la Barre, D. Idiyatullin, S. M. Sohn, J. T. Vaughan, and H. Krishnaswamy, "STAR MRI with non-magnetic, integrated circulator based on switched transmission lines." In Proc. 30th Int. Soc. Magn. Resonance. Med., 2021, p. 4277.

[54] Aravind Nagulu, T. Chen, G. Zussman, and H. Krishnaswamy, "A Single Antenna Full-Duplex Radio using a Non-Magnetic, CMOS Circulator with In-Built Isolation Tuning," May 2019, doi: https://doi.org/10.1109/iccw.2019.8756839.

[55] Aravind Nagulu *et al.*, "A Full-Duplex Receiver With True-Time-Delay Cancelers Based on Switched-Capacitor-Networks Operating Beyond the Delay–Bandwidth Limit," *IEEE Journal of Solid-state Circuits*, vol. 56, no. 5, pp. 1398–1411, May 2021, doi: https://doi.org/10.1109/jssc.2021.3063658.

[56] S. Salama, "Reactive-element based isolation network for a two-element MRI phased array," Journal of King Saud University - Engineering Sciences, vol. 32, no. 1. pp. 42–50, 2020.

[57]   S. Salama and A. Abuelhaija, "Parasitic Element Based Isolation Network for a Two-Element MRI Phased Array," 2019 IEEE Jordan Int. Jt. Conf. Electr. Eng. Inf. Technol. JEEIT 2019 - Proc., no. 1, pp. 790–793, 201

[58]   S. Hashemi, S. K. Kandala, and S.-M. Sohn, "Dielectric Loaded decoupling technique for multichannel RF coils," in *IEEE/MTT-S International Microwave Symposium*, IEEE, 2023.

[59]   Z. A. Colwell and S.-M. Sohn, "Miniaturized tunable extended eight-port hybrid coupler for 1.5 T MRI," *International Journal of Microwave and Wireless Technologies*, vol. 15, no. 5, pp. 805–809, 2023.

[60]   "Dielectric Properties of Body Tissues: HTML clients," *niremf.ifac.cnr.it*. http://niremf.ifac.cnr.it/tissprop/htmlclie/htmlclie.php (accessed Oct. 5, 2023)

[61]   "Dielectric phantom recipe generator," National Institute of Neurological Disorders and   Stroke, https://www.amri.ninds.nih.gov/cgi-bin/phantomrecipe (accessed Oct. 5, 2023).

[62]   J. S. Hyde, A. Jesmanowicz, W. Froncisz, J. B. Kneeland, and T. M. Grist, "Parallel Image Acquisition from Noninteracting Local Coils," *J. Magn. Reson.*, vol. 70, pp. 512-517. 1986.

[63]   P. B. Roemer, W. A. Edelstein, C. E. Hayes, S. P. Souza, and O. M. Mueller, "The NMR Phase array," Magn Reson Med., vol. 16, no. 2. pp. 192–225, 1990.

[64]   A. Deshmane, V. Gulani, M. A. Griswold, and N. Seiberlich, "Parallel MR Imaging, " *J. Magn. Reson.,* vol. 36, no. 1, pp. 55-72. 2012.

[65]   B. Gruber, M. Froeling, T. Leiner, and D. W. J. Klomp, "RF Coils: A Practical Guide for Nonphysicists," *J. Magn. Reson. Imaging*. vol. 48, pp. 590-604. 2018.

[66]   S. Khan and T. Calabria, "How to Replace Optocouplers with Digital Isolators in Standard Interface Circuits," *Application Brief No. SLLA522A*. https://www.ti.com/lit/an/slla522a/slla522a.pdf (accessed Jun. 3, 2023)

[67]   "Digital Isolator Design Guide," *Application Note No. SLLA284F*. https://www.ti.com/lit/an/slla284f/slla284f.pdf (accessed Jun. 3, 2023)

[68]   M. Weiger, and K. P. Pruessmann, "MRI with Zero Echo Time," eMagRes, 1, 311–322. 2012.

[69]   J. Du, G. Ma, S. Li, M. Carl, N. Szeverenyi, S. Vandenberg, J. Corey-Bloom, and G. M. Bydder, "Ultrashort echo time (UTE) magnetic resonance imaging of the short T2 components in white matter of the brain using a clinical 3T scanner," NeuroImage, 15;87:32-41. 2014.

APPENDIX A

ACRONYMS AND INITIALISMS

Simultaneous Transmit and Receive (STAR)

Magnetic Resonance Imaging (MRI)

Nuclear Magnetic Resonance (NMR)

Continuous Wave (CW)

Radio Frequency (RF)

Specific Absorption Rate (SAR)

Frequency Modulated Continuous Wave (FMCW)

Radio Frequency Identification (RFID)

Sweep Imaging with Fourier Transform (SWIFT)

Printed Circuit Board (PCB)

Device Under Test (DUT)

Transverse Electromagnetic (TEM)

High Frequency Structure Simulator (HFSS)

Electromagnetic Interference (EMI)

Direct Current (DC)

Printed Circuit Board Assembly (PCBA)

Sub-Miniature Version A (SMA)

Inductor-Capacitor (LC)

Coplanar Waveguide (CPWG)

Grounded Coplanar Waveguide (GCPWG)

Signal to Noise Ratio (SNR)

Advanced Design System (ADS)

Concurrent Excitation and Acquisition (CEA)

Analog to Digital Converter (ADC)

Field Programmable Gate Array (FPGA)

Voltage Controlled Oscillator (VCO)

Digital to Analog Converter (DAC)

Serial Peripheral Interface (SPI)

Metal Oxide Semiconductor Field Effect Transistor (MOSFET)

Micro Coaxial (MCX)

Bipolar Junction Transistor (BJT)

Light Emitting Diode (LED)

General Purpose Input Output (GPIO)